Master's Thesis

Sensitivity of snowmelt energy fluxes during rain-on-snow events to topography, climate conditions and land use.

Daniel Günther

M.Sc. Hydrology — University of Freiburg.

Supervisors:

Prof. Dr. M. Weiler	University of Freiburg, Germany
Prof. Dr. J. W. Pomeroy	University of Saskatchewan, Canada

Abstract

When liquid precipitation falls onto a snowpack the resulting melt water production can contribute to flood events. This research shows, that rain induced melt events could be modeled with satisfactorily accuracy at several stations in the alpine and treeline zones of the Canadian Rocky Mountains. The main source of energy available for rain-on-snow (ROS) melt was found to be radiation for most scenarios examined. Turbulent fluxes and advective heat transfer from the rain itself can also contribute significant amounts of energy. The model results show that air temperature is the main factor controlling the available energy for melt, particularly due to its impact on the incoming longwave radiation, advective heat and the turbulent fluxes. Depending on the air temperature, wind speed and precipitation have different impacts on snow melt rates. It was found that snow melt energetics during ROS conditions are not as sensitive to land use and topography as during clear sky pre-event periods. This is especially true for events that come with low to moderate wind speeds.

Extended Abstract

Regen-auf-Schnee (ROS) Ereignisse können auf Grund der daraus resultierenden Schneeschmelze Hochwasserereignisse auslösen. In dieser Arbeit wurde gezeigt, dass durch Regen induzierte Schmelzereignisse vom verwendenden Modell mit hinreichender Genauigkeit dargestellt werden konnten. Für die meisten Szenarien wurde die Kombination aus kurzwelliger und langwelliger Strahlung als Hauptquelle der Schmelzenergie identifiziert. Die Modelergebnisse zeigen, dass durch die Verstärkung der langwelligen Einstrahlung, des advektiven Energieaustausches mit dem Regen und der turbulenten Flüsse, die Lufttemperatur den stärksten Einfluss auf die Schneeschmelze hat. Darüber hinaus kontrolliert die Lufttemperatur die Wirkung der Windgeschwindigkeit und vor allem der Niederschlagsmenge auf die Energiebilanz. Es wurde gezeigt, dass im Vergleich zu wolkenlosen Bedingungen, die Schneeschmelze während ROS Ereignissen weniger stark von Topografie und Landnutzung abhängt. Dies gilt vor allem für Ereignisse, die mit niedrigen oder moderaten Windgeschwindigkeiten einhergehen.

keywords: Alberta flood 2013, rain-on-snow, sensitivity analysis, snowmelt, snowpack energy balance

Acknowledgements

First, I would like to thank my supervisors Prof. Dr. John Pomeroy and Prof. Dr. Markus Weiler, who made this present work possible and acknowledge their support and guidance through my graduate studies. I wish to thank Dr. Stefan Pohl for valuable commentary and feedback throughout the development of my thesis and Xing Fang for his insights and expertise in modeling issues.

I thank the Centre for Hydrology field technicians May Guan and Angus Duncan for spending countless hours collecting data, Alberta Environment and Sustainable Resource Department for providing meteorological observations and funding of this study. Furthermore I would like express my gratitude to my fellow students Nicolas Leroux, Sebastián Krögh and Ramona Skozilas for discussions, their encouragement and help to organize paperwork. I am also grateful to the community of developers of R, an open source statistical software, which was used for the analysis in this thesis.

Finally, I want to thank my family who supported me throughout my studies and without whom I could not have completed my degree.

Contents

List of Symbols

symbol	unit	description
a	[-]	wind speed attenuation coefficient
a_e	[-]	ratio of eddy diffusivity and viscosity for water vapor
a_h	[-]	ratio of eddy diffusivity and viscosity for heat
B_{net}	[kg/m^2]	net input and output of blowing snowt
c_i	2102 [J/(kg∗K)]	heat capacity of ice
C_p	1006 [J/(kg∗K)]	specific heat of dry air
C_{p-p}	[kJ/(kg∗K)]	specific heat of precipitation
d_0	[-]	zero-plane displacement height
E_{evap}	[kg/(m^2∗s)]	evaporation rate
E_{subl}	[kg/(m^2∗s)]	sublimation rate
g	9.807 [m/s^2]	gravitational acceleration
H	[m]	canopy height
I	[kg/m^2]	interception
i	[-]	time step
k	≈ 0.4[-]	Karman constant
$K_{es,0}$	[J/(m∗K∗s)]	effective thermal conductivity for the surface
$K_{es,l}$	[J/(m∗K∗s)]	effective thermal conductivity for the lower snow layer
K_{eg}	[J/(m∗K∗s)]	effective thermal conductivity for the soil
L	[m]	Obukhov stability length
L_f	3.37E05 [J/kg]	latent heat of fusion
L_{vi}	2.828E06 [J/kg]	latent heat of sublimation
L_{vl}	2.505E06 [J/kg]	latent heat of evaporation
M	[kg]	mass
n	[-]	number of pairs
P	[kg/(m^2∗s)]	precipitation rate
q	[kg/kg]	specific humidity of air
$q_{s,0}$	[kg/kg]	specific humidity of the snow surface
Q_a	[W/m^2]	advectiv heat
Q_{cc}	[W/m^2]	cold content
Q_e	[W/m^2]	latent heat

Q_g	[W/m^2]	ground heat
Q_h	[W/m^2]	sensible heat
$Q_{lw\uparrow}$	[W/m^2]	outgoing longwave radiation
$Q_{lw\downarrow}$	[W/m^2]	incoming longwave radiation
Q_{lnet}	[W/m^2]	net longwave radiation
Q_m	[W/m^2]	energy flux density available for melt
Q_n	[W/m^2]	net all-wave radiation
$Q_{sw\uparrow}$	[W/m^2]	outgoing shortwave radiation
$Q_{sw\downarrow}$	[W/m^2]	incoming shortwave radiation
Q_{snet}	[W/m^2]	net shortwave radiation
$R_{release}$	[kg/(m^2∗s)]	melt water release
RH	[%]	relative humidity
t	[s]	time
t_{step}	[s]	time step length
T_a	[°C; K]	air temperature
T_g	[°C; K]	soil temperature
T	[0°C ;273.15K]	melting precipitation temperature
T_{pp}	[°C; K]	precipitation temperature
T_s	[°C; K]	mean snow pack temperature
$T_{s,0}$	[°C; K]	snow surface temperature
$T_{s,l}$	[°C; K]	lower snow layer temperature
U	[J/m^2]	cold content
u	[m/s]	wind speed
u_H	[m/s]	wind speed at top of the canopy
u^*	[m/s]	friction velocity
V_{water}	[m^3]	volume of liquid water
V_{snow}	[m^3]	volume of the snowpack
V_{ice}	[m^3]	volume of solid water
w_c	[-]	liquid water content
$w_{c,max}$	[-]	maximal water retention capacity
z	[m]	height
z_0	[m]	roughness length
z_{pp}	[m]	precipitation depth
z_q	[m]	measurement height for humidity
z_T	[m]	measurement height for air temperature
z_u	[m]	measurement height for wind speed

z_s	[m]	snow pack thickness
$z_{s,0}$	[m]	active snow layer thickness
$z_{s,l}$	[m]	lower snow layer thickness
$z_{s,m}$	[m]	modeled snow pack thickness
$z_{s,o}$	[m]	observed snow pack thickness

Greek symbols

symbol	unit	description
α	[-]	snow albedo
β	[-]	fraction of ice in a unit mass of snow
Δ	[-]	change; difference
ρ	[kg/m^3]	density of air
ρ_{pp}	[kg/m^3]	density of precipitation
ρ_w	[kg/m^3]	density of liquid water
ψ_{sh}	[-]	stability function for heat
ψ_{sm}	[-]	stability function for mass
ψ_{sv}	[-]	stability function for water vapor

Abbreviations

CRHM	Cold Regions Hydrological Model
EB	energy balance
FR	Fisera Ridge main station
FR_N	Fisera Ridge north face
FR_S	Fisera Ridge south face
FR_SF	Fisera Ridge south face forest
HRU	hydrological response unit
ISC	initial snowpack condition
LAI	leaf area index
LES	Little Elbow Summit
MCRB	Marmot Creek Reasearch Basin
NSE	Nash-Suttclif efficiency
ROS	rain on snow

RMSE	root mean square error
SWE	snow water equivalent
SS	snow survey
UC	Upper Clearing
UCT	Upper Clearing tower
UF	Upper Forest

List of Figures

List of Tables

1 Introduction

Rain-on-snow events (ROS) are a common feature in many regions, such as the North American West (e.g. Marks et al., 1998; Harr, 1981; McCabe et al., 2007; Mazurkiewicz et al., 2008) as well as the American East (Pradhanang et al., 2013), Central Europe (Garvelmann et al., 2014; Singh et al., 1997; Sui and Koehler, 2001) and northern Eurasia (Ye et al., 2008). However, those events all occur in temperate climates, where water is seasonally stored in a snowpack. If rainfall reaches a melting snow surface, the melt rates can be accelerated and a flood or landslide can be induced (Sui and Koehler, 2001; Harr, 1981). However, the higher potential for generating floods of those events, compared to snowmelt driven predominantly by radiative exchange, is not only due to the extra energy provided by rainfall, but also due to the surplus of water from the precipitation and condensation (Mazurkiewicz et al., 2008). In fact, ROS events which occur late in melt season can also lead to reduced melt rates (Pomeroy et al., 2014). This is especially true for antecedent high radiation-induced melt rates. Other studies such as the one from Solberg et al. (2001) emphasize the biological importance of rain-on-snow events, due to the formation of ice lenses, that keep animals from feeding.

This study aims to analyze the contribution of the energy balance components to the total energy available for melt and to demonstrate the sensitivity of these energy fluxes to topography, climate conditions and landuse. To improve insights into mechanisms which control ROS events is crucial for a deeper understanding of melt processes, risk assessment and eventually for flood forecasting.

2 Literature Review

2.1 Engery Budget Terms of a Snowpack

The energy budget (EB) for a snowpack is the sum of all energy fluxes of radiance, convection, conduction and advection. It uses a control volume, which is limited by the atmosphere-snow interface and by the soil surface. If the horizontal energy flux is neglected, the energy balance for a snowpack can be written as:

$$\frac{dU}{dt} = Q_{snet} + Q_{lnet} + Q_h + Q_e + Q_g + Q_a + Q_m \tag{1}$$

Where $\frac{dU}{dt}$ is the change in snowpack internal sensible and latent heat storage, which is also referred as the change of the internal cold content per unit area of snowcover. Q_{snet} is the net shortwave radiation energy flux, Q_{lnet} is the net longwave radiation energy exchange. Q_h represents the convective exchange of sensible heat with the atmosphere and Q_e is the convective exchange of latent heat of vaporization and sublimation with the atmosphere. Q_g is the ground heat flux, Q_a is the advected energy from precipitation and Q_m is the energy flux associated with melt. The terms of the energy balance are energy flux densities (W/m^2). Fluxes towards the snowpack are positive, fluxes away from the snowpack have a negative sign. All terms except for Q_{snet}, Q_a and Q_m can represent either energy gains or losses (DeWalle and Rango, 2008). In the case of a subfreezing snowpack Q_m is equal to zero, whereas for an isothermal snowpack U is equal to zero.

The net shortwave radiation Q_{snet} is defined as:

$$Q_{snet} = Q_{sw\downarrow} * (1 - \alpha) \tag{2}$$

Where $Q_{sw\downarrow}$ is the incoming shortwave solar radiation and α is the surface albedo or fractional reflectivity of the snow surface. The net longwave radiation flux Q_{lnet} can be written as the sum of incoming ($Q_{lw\downarrow}$) and outgoing ($Q_{lw\uparrow}$) longwave radiation:

$$Q_{lnet} = Q_{lw\downarrow} - Q_{lw\uparrow} \tag{3}$$

The mass balance describes the accumulation and the ablation of a snow volume:

$$\Delta SWE = P_{net} + E - R_{release} \tag{4}$$

Where SWE is the snow water equivalent, P the net precipitation inputs from snowfall, rainfall and blowing snow. E is either the condensation rate or sublimation rate, depending on the sign of the latent heat flux, which is positive towards the snowpack. $R_{release}$ represents the outflow of liquid water from the snowpack, which becomes available for runoff or infiltration, and contributes only to ablation. The terms in equation 4 represent cumulative mass fluxes per unit area (e.g. kg/(m^2)). P_{net} is the precipitation P minus the fraction of the intercepted precipitation I that is lost due the sublimation of intercepted snow respectively evaporation of intercepted rain and cannot contribute to snowpack SWE by dripping or unloading. It summarizes as well the net mass gain and mass loss of the snowpack due to transport of blowing snow B_{net} (see fig. 1). The mass balance of a snowpack is coupled to the EB via:

a) $R_{release}$ accounts for water from rainfall, melt and internal changes in the water retention capacity (DeWalle and Rango, 2008). When no rainfall occurs $R_{release}$ is highly dependent on the melt rate M and therefore coupled to Q_m:

$$M = Q_m/(\rho_w L_f \beta)) \tag{5}$$

Where, ρ_w is the density of water, L_f is the latent heat of fusion and β is the fraction of ice in a unit mass of snow (Gray and Male, 2004)

b) E is related to the latent heat flux by:

$$Q_e = L_{vi} E_{subl} \approx L_{vi} E \tag{6}$$

Where L_{vi} is the latent heat of sublimation for ice (King et al., 2008).

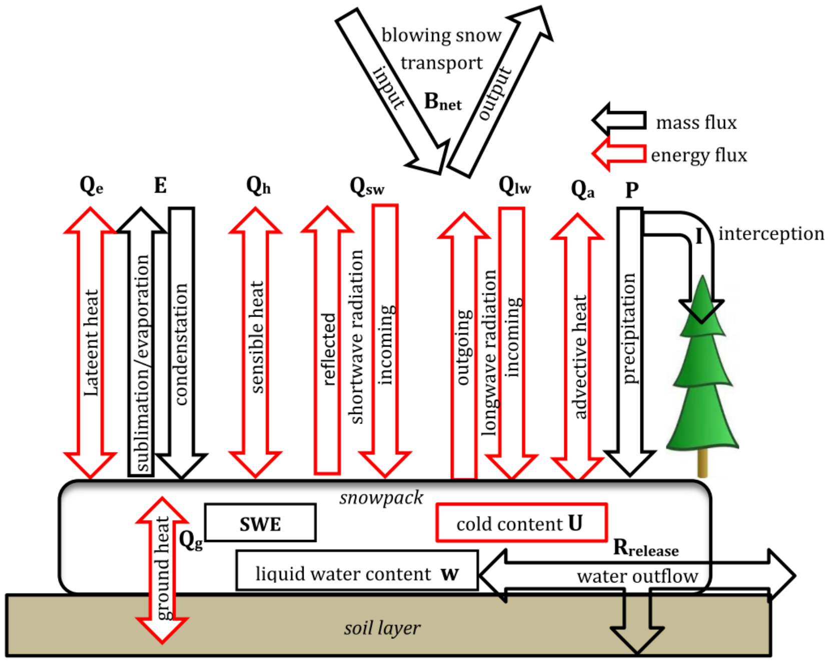

Figure 1: Schematic diagram of snowpack energy and mass fluxes.

2.2 Snowcover Accumulation

One necessary condition for rain-on-snow is the accumulation of snow on the ground prior to these events (McCabe et al., 2007). The spatial distribution of the snowcover is influenced primarily by elevation (Jost et al., 2007; Pomeroy et al., 1998b) and various other factors, such as vegetation cover, wind field and topographic features; therefore, a high variability through different spatial scales is generally observed (Anderton et al., 2002). The factors that influence snow accumulation and redistribution under various land use types are well documented and can be found in Pomeroy et al. (1998b), Jost et al. (2007), Strasser et al. (2011), Varhola et al. (2010), Musselman et al. (2008) and Winkler et al. (2005) as examples.

2.3 Energy Balance During a Rain-on-Snow Event

During a ROS event, energy is added to the snowpack mainly in the form of longwave radiation from clouds, latent heat due to condensation, sensible heat from warm air and advective energy from the rain itself (Marks et al., 1998). Since rain-events come with increasing cloud cover, the incoming shortwave radiation $Q_{sw\downarrow}$ decreases. Albedo increases as well, due to non-uniform radiation extinction in the cloud cover (Male and Granger, 1981). However, liquid precipitation also alters the albedo. Increasing water content in the snowpack replaces the air between the snow crystals and reduces the reflectivity (Wiscombe and Warren, 1980).

Incoming longwave radiation $Q_{lw\downarrow}$ shows a positive trend with cloud cover (Male and Granger, 1981). However, outgoing longwave radiation $Q_{lw\uparrow}$ is dependent on the surface temperature of the snowcover and is, therefore, restricted to emission of a 0 °C surface during snowmelt (see equation 9). The increase in net longwave radiation Q_{lnet} is usually more important than the decrease in net shortwave Q_{snet} during ROS events (Berris and Harr, 1987).

During spring snowmelt periods, the latent heat is often negative, due to the sublimation of water vapour from the snowpack. It mirrors the sensible heat flux and reduces the net turbulent transfer of energy to the snowpack (Pohl et al., 2006). However, at the onset of a ROS event both turbulent fluxes become positive and might even become the dominant fluxes (Garvelmann et al., 2014). The increase in air temperature, which is associated with ROS events, contributes to the sensible heat energy transfer (Male and Granger, 1981). Condensation of water vapour on the snow surface occurs due to the increase in atmospheric water vapour, which reverses the water vapour pressure gradient between snow surface and atmosphere. This effect leads to the release of latent heat, as well as to the addition of mass into the snowpack. Turbulent fluxes are functions of wind speed, air temperature and humidity gradients, stability of the air layers and surface roughness (van Heeswijk et al., 1996).

The ground heat flux Q_g is temperature and moisture-gradient dependent. Due to infiltration of melt and rainwater into frozen soil, the refreezing of the water and the consequential release of latent heat keeps this gradient small. Therefore, Q_g plays a minor role int the snowmelt EB (Pomeroy et al., 1998a).

Advective energy Q_a from the precipitation adds to the snowmelt EB. Q_a can contribute a significant magnitude to the EB, especially in the case of a cold snowpack. Percolating rainwater refreezes and can contribute to the snowmelt EB via the release of latent heat (Marks et al., 1998). During a ROS event, rain -and meltwater move several times faster through the snowpack then natural snowmeltwater under dry conditions (Singh and Kumar, 1997).

Positive net energy fluxes contributes to warm the snowpack (up to 0 °C), and hence to decrease the cold content. In isothermal state, additional energy input results in the production of meltwater and its release, once the holding capacity of liquid water (in mid-snowmelt period from 1 % to 2.5 % (Lu et al., 2012); up to 6.8 % in ROS situation, respectively, 14.2 % if ice layers are present (Singh and Kumar, 1997)) is reached.

Vegetation Effects: The influence of vegetation cover is not just limited to the accumulation phase, but also plays an important role during the snowpack depletion. The different EB components have different magnitudes for a melting snowpack under a forest canopy as oppose to one in an open environment (van Heeswijk et al., 1996).

One of the main difference in melt energetics between forested and non-forested sites under clear sky conditions is the absorption of incoming shortwave radiation and the emission of longwave radiation due to canopy shading (Berris and Harr, 1987). In a counteracting way, forest cover reduces the albedo of the sub-canopy snowpack due to litter and preferential absorption of radiation in visible wavelengths (Melloh et al., 2002). However, the increasing cloud cover during a ROS event attenuates $Q_{sw\downarrow}$ and, therefore, alters the shading effect of the vegetation and the emission of longwave radiation from the warming canopy (Pomeroy et al., 2009). The canopy might even cool down during a ROS event as the vegetation surface tends to reach the wet-bulb temperature due to evaporative cooling (J.W. Pomeroy, personal communication, 13.01.2015).

Wind speed is significantly altered in the forest, which has a strong influence on the turbulent fluxes of latent and sensible heat (Berris and Harr, 1987; Male and Granger, 1981). On the other hand, and due to the higher turbulence introduced by the forest canopy, roughness lengths were found to be higher under the vegetation than in the open (Reba et al., 2012). Moderated air temperatures, as well as increased relative humidity influence the turbulent fluxes under the vegetation during non-ROS days (Hardy et al., 1997). However, during ROS events temperature and humidity differences might be less relevant, due to overall high air humidity and altered incoming shortwave radiation.

The input of advective heat from the rain and the release of latent heat due to refreezing in cold the snowpacks is also affected by vegetation cover. The canopy influences the incoming liquid precipitation amount in various ways. First, as a result of melting intercepted snow during rainfall, leading to higher sub-canopy precipitation amount. Second, due to the melting and dripping of intercepted snow during dry conditions, leading to rain-like conditions in the forest (Berris and Harr, 1987; Storck et al., 2002). Third, light snowfall at high dew point temperatures around 0 °C changes phase under the canopy but not in the open. Fourth, interception of rainfall alters the precipitation amount under the canopy, which is most important during events with smaller rainfall intensities (Rutter et al., 1972).

In contrast to the studies conducted by Marks et al. (1998) and Berris and Harr (1987), who found a large difference in melt rates, Garvelmann et al. (2014) noted very similar cumulative snowmelt energetics during rain-on-snow events for forested and open sites. Berg et al. (1991) found no significant difference in outflow amount between open and forested sites during ROS. However, these studies agree that in a rain-on-snow situation Q_{snet} becomes less important for melt energy balance, whereas Q_{lnet} and the turbulent fluxes gain significance compared to clear sky periods, especially for an open environment. The disagreement in the literature about the effect of forest cover on snowmelt in a ROS situation shows that there is a lack of knowledge about the controls during such events.

2.4 2013 Alberta Flood

In June 2013, Alberta experienced widespread flooding. Heavy rainfall of up to over 100 mm/d started on June 19^{th} and continued for three days. The storm with its large spatial extent caused flood levels in many rivers and lakes throughout much of the southern half of Alberta. Many municipalities declared local states of emergency and more than 100,000 people evacuated their homes. Five people lost their live. High water levels and debris flow damaged property and infrastructure considerably. Recovery costs are projected to exceed $6 billion (Pomeroy et al., submitted). In high altitudes of the Canadian Rocky Mountains, especially in wind sheltered locations, there was still a snowcover present at the onset of the event.

It is crucial for flood risk assessment and flood forecasting to know the potential contributions of rainfall to snowmelt generation, which impacts the water levels and flood plains. Extreme events, such as the June 2013 flood, emphasize the need for a detailed, process based understanding of the controls during rain-on-snow events. This study aims to improve the understanding of these controls.

2.5 Modeling ROS Melt Energetics

Physically based hydrological models can be used to better understand and predict the behaviour of the hydrological cycle, in particular, the dynamics during ROS events. The Cold Regions Hydrological Model (CRHM) platform (Pomeroy et al., 2007) is able to reproduce most processes presented in section 2.3. CRHM handles direct and diffuse shortwave radiation to a slope under different canopy coverages and longwave emission by the atmosphere, surrounding terrain and the vegetation. Furthermore, processes, such as blowing snow, interception and sublimation are represented. The EB of a snowpack and the resulting meltwater production are calculated. The model was successfully applied in various studies in Western Canada (e.g. Ellis et al., 2010; DeBeer, 2012; Fang et al., 2013; Rasouli et al., 2014) and other cold regions of the world (e.g. López-Moreno et al., 2013; Zhou et al., 2014; Krogh et al., 2015). The model platform and its components are further described in section 4.4.

3 Objectives

- Simulate the energy and mass balance during ROS events and validate the model performance.
- Identifying the meteorological controls on the snowpack energy balance and the relative importance of its components under varying antecedent conditions during the June 2013 rain event and a adjacent clear sky period.
- Identifying the control of environmental parameters such as topography, climate variation and forest cover on the snowpack energy balance during a ROS event.

4 Methods

4.1 Study Sites

4.1.1 Marmot Creek

The Marmot Creek Research Basin (MCRB, fig. 2) covers an area of 9.4 km^2 in the Kananaskis Valley, Alberta, Canada, approx. 75 km west of Calgary. It was established in 1961 to assess the effect of different forestry systems on basin hydrology (Golding, 1974). The catchment consists of four subbasins: Cabin Creek (2.35 km^2), Middle Creek (2.94 km^2), Twind Creek (2.79 km^2) and the Moarmot Creek confluence (1.32 km^2). The topography of the watershed can be described as rather steep, with an elevation range of 1225 m. The highest point of the basin is Mount Allan with an elevation of 2825 m a.s.l. (Pomeroy et al., 2012).

Under the timberline, which is at about 2300 m, the vegetation primarily consists of Engelmann spruce (Picea engelmanni Parry), alpine fir (Abies lmiocarpa) and lodgepole pine (Pinus contorta var. Latifolia) (Golding, 1974). Large clear-cuts as well as various smaller circular clearings can be found in different part of the watershed, due to forest management experiments in the 1970s and 1980s (Pomeroy et al., 2012). Storr (1967) found an average annual precipitation of 896 mm of which only 25-30 % occurs as rain. Therefore Marmot Creek is a snow dominated basin with mean monthly air temperatures ranging from 14 °C in July to -10 °C in January (Pomeroy et al., 2012).

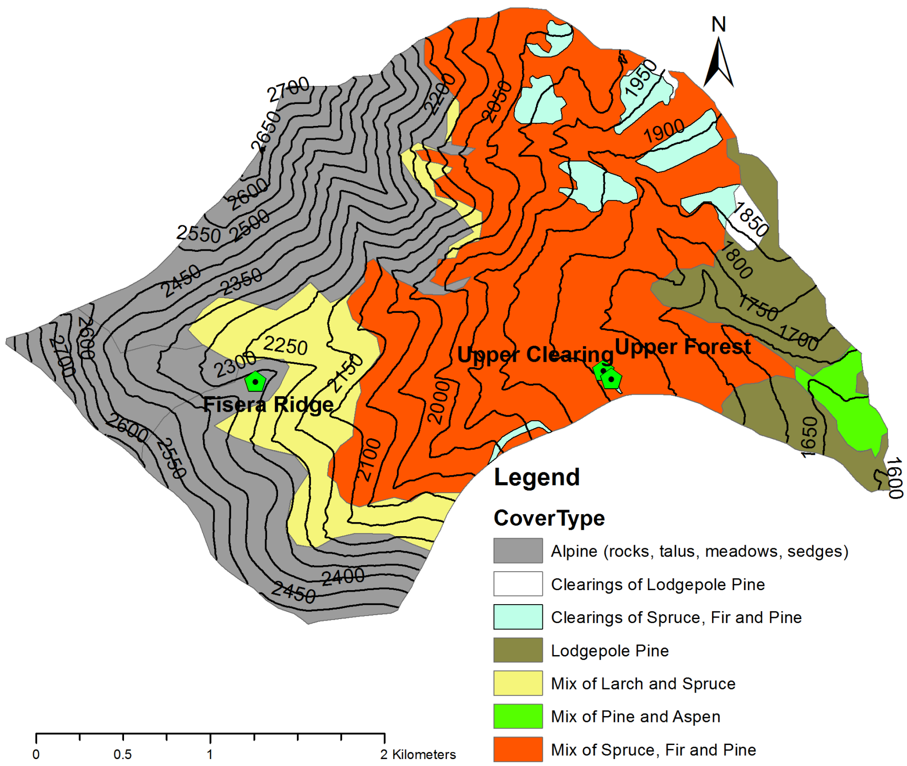

Figure 2: Marmot Creek Research Basin: land cover and meteorological stations.

The MCRB is equipped with several meteorological stations. Because the few ROS events that met the criteria specified in section 4.3 occurred late in the melt season, the analysis of the events was limited to data from one meteorological station (details in tab. 1) and adjacent four snow survey sites (fig. 3). In addition, either site of the ridge is equipped with an automated sonic snowdepth measurement system.

- Fisera Ridge Main Station (FR): The main station is located on the fairly level ridge top, right above the tree line at 2325 m a.s.l.. It is representative location of the alpine-forest transition zone in the Front Ranges of the Rockies (DeBeer, 2012).
- Fisera Ridge North Facing (FR_N): The north facing site of the ridge (345°) is sparsely vegetated. Due to local wind fields, this windward

site shows shallow snowpacks.

- Fisera Ridge South Facing (FR_S): In contrast to FR_N big snowdrifts can form on the leeward south facing site (101°). These persistent drifts were crucial for the analyzes of the identified events. Scattered shrub vegetation and small trees can be found here.

- Fisera Ridge South Facing Forest (FR_SF): The south facing forest is located just below FR_S. It is a rather sparse *Larix lyallii* (Alpine larch) forest with a winter LAI of about 0.92 and spring LAI of 1.2.

At all of the above described sites regular snow surveys (SS) have been conducted as shown in figure 3.

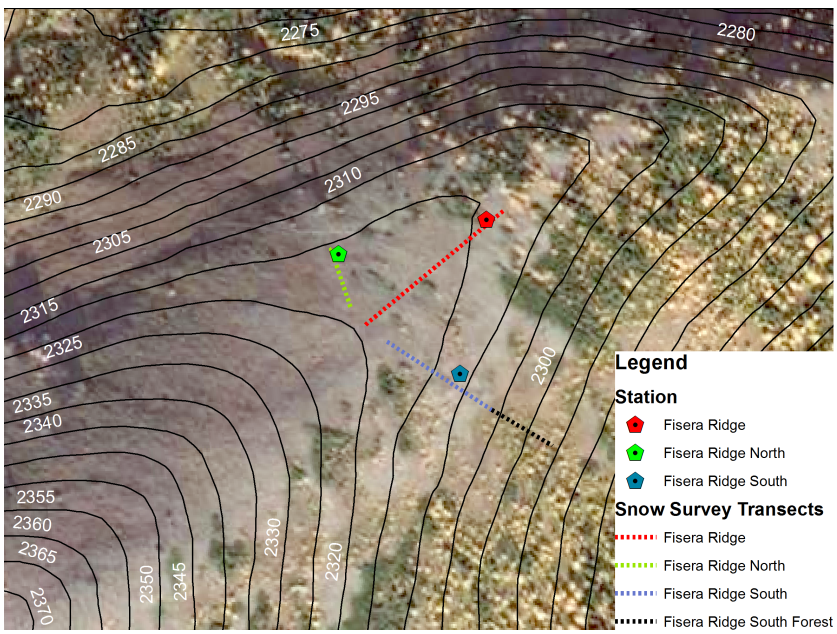

Figure 3: Location of meteorological station and snow survey transects at Fisera Ridge.

To provide meteorological input data for the sensitivity analysis, three mid elevation (1845 m a.s.l.) stations were used in this study:

- Upper Forest (UF): predominantly vegetation at this site is *Picea engelmanni* (Engelmann spruce) and *Pseudotsuga menziesii var. glauca*

(Douglas fir) with average tree heights of about 20 m (MacDonald, 2010).

- Upper Clearing Main Station (UC): this approximately 60 m wide clear cut shows slight regeneration of forest vegetation with stand heights of ≤ 1.5 m (MacDonald, 2010).
- Upper Clearing tower (UCT): a 20 m tall Del-Hi triangular free standing tower is located in the center of the very same clear cut (MacDonald, 2010).

4.1.2 Little Elbow Summit

The station at the Little Elbow Summit is operated by Alberta Environment ans Sustainable Resource Development (AESRD). It is located north of Tombstone Pass and about 44 km south east of Marmot Creek at an elevation of 2160 m. The meteorological station and the snow pillow are located in a small gap within a dense mature spruce forest. The Alter-shielded precipitation gauge is located approximately 40 m west of it.

4.2 Observation Data

Table 1 lists measured meteorological parameters and snowpack characteristics obtained at the Fisera Ridge and Little Elbow Summit site, which are used for model input and validation purposes. Specifications of the measurement devices used in this study are indicated.

Table 1: Forcing and validation data Fisera Ridge and Little Elbow Summit

Observation	FR	FR_S/FR_N	FR_SF	LES
air T [°C]	Campbell Sci. HMP45C212	X	X	Campbell Sci. HMP45C
soil T [°C]	K-type soil thermocouple	X	X	X
RH [%]	Campbell Sci. HMP45C212	X	X	Campbell Sci. HMP45C
U [m/s]	RM Young anemometer 05103AP	X	X	X
P [mm]	Geonor T-200B alter shielded strain gauge	X	X	Ott Pluvio 1000 alter shielded
$Q_{sw\downarrow}$ [W/m^2]	Kipp & Zonen CNR1 pyranometer	X	X	X
snowdepth [m]	Campbell Sci. SR50 sonic ranger	Campbell Sci. SR50 sonic ranger	X	X
SWE [mm]	SS	SS	SS	Snow pillow with water log encoder

The sensitivity analysis was forced with data measured at the Upper Clearing, Upper Forest and Upper Clearing Tower site. The details about employed devices are shown in table 2.

Table 2: Forcing and validation data at Upper Clearing, Upper Clearing Tower and Upper Forest, used for the sensitivity analysis.

Observation	UC	UCT	UF
air T [°C]	Campbell Sci. HMP35C	x	Campbell Sci. HMP212
RH [%]	Campbell Sci. HMP35C	x	Campbell Sci. HMP212
U [m/s]	RM Young anemometer	RM Young anemometer	RM Young anemometer
P [mm]	Geonor T-200B alter shielded strain gauge	x	x
$Q_{sw\downarrow}$ and $Q_{lw\downarrow}$ [W/m^2]	Kipp & Zonen CNR4 radiometer	Kipp & Zonen CNR4 radiometer	Kipp & Zonen CNR4 radiometer

Air temperature and humidity measurements are obtained at the UCT site, but not used in the analysis. Here, the humidity readings are heavily influenced by the transpiration of the surrounding vegetation and can therefore not be used to represent an open environment. Also, the air temperature measured at 20 m is not applicable for the calculation of near ground processes.

To derive the wind speed in a forested environment where no sub-canopy measurements are available, a simple approach proposed by Cionco (1965) was applied:

$$u = u_H \exp^{a(\frac{z}{H}-1)} \tag{7}$$

Where u is the wind speed under the canopy in height z, H is the canopy height and a is an attenuation coefficient, set to 1 for larch forest and to 2.74 for spruce (Cionco, 1978). Thereby the wind speed for the FR_SF site could be computed, assuming that the above canopy wind speed equals the measured wind speed on the ridge. For the computation of the sub-canopy wind speed at the LES site, an above canopy wind speed interpolated from 7 stations within a 57.1 km radius, as provides by Alberta Environment, was used. This approach was tested for the June 2013 event (June 19th to 21st) and for three days prior to this event (June 16th to 19th) using the 20 m above canopy wind speed data at the UCT and sub-canopy measurements at UF. This validation resulted in an r^2 for the event of 0.73 and a RMSE of 0.087 m/s and r^2 =0.46 and RMSE=0.091 m/s for the pre-event period respectively (see fig. 39 in Appendix A).

There are no shortwave radiation measurements at the LES site. Due to the nature of big ROS events, which come with full cloud cover and therefore a very high fraction of diffuse radiation, the incoming shortwave radiation readings were approximated by measurements at FR.

4.3 Defining ROS-Events

Past ROS events were extracted from the observation time series using precipitation amount, phase and the snowdepth data. The precipitation phase was derived using a psychometric energy balance method proposed by Harder and Pomeroy (2013). To specify a ROS event, a similar approach to Mazurkiewicz et al. (2008) was applied. To pass the criteria of a ROS event all of the following conditions had to be met:

- at least 6 hours of consecutive precipitation.
- snowfall fraction ≤ 0.1
- mean precipitation intensity $\geq$ 1mm/h
- minimum precipitation intensity $\geq$ 0.5mm/h
- measured snowdepth $\geq$ 10cm

By applying these filter criteria to the obervation time series, three events could be identified. They are characterized in section 5.1.

- 17^{th} - 19^{th} of June 2011
- 12^{th} - 13^{th} of May 2013
- 19^{th} - 21^{th} of June 2013

4.4 Cold Regions Hydrological Model Platform

The Cold Regions Hydrological Model (CRHM) platform is a physically based modular model. Appropriate modules can be selected from a library in order to simulate the hydrological processes in different hydrological response units (HRU). These units can be defined as areas, where the same set of parameters for mass and energy balance calculation can be applied. Thereby one HRU is defined by three groups of attributes: biophysical structure, hydrological state and hydrological flux. Module parameters are characterized by the user. CRHM automatically links these modules in the sequential order. (Pomeroy et al., 2007).

In this study the model will perform simulations of the energy fluxes of a snowpack at point scale. Therefore no hydrological routing between the point HRUs is provided. Due to the missing linkage between the HRUs, meaningful redistribution of blowing snow is not possible in this model setup. Since this study addresses rather short periods of wet melt events the redistribution of blowing snow is neglected.

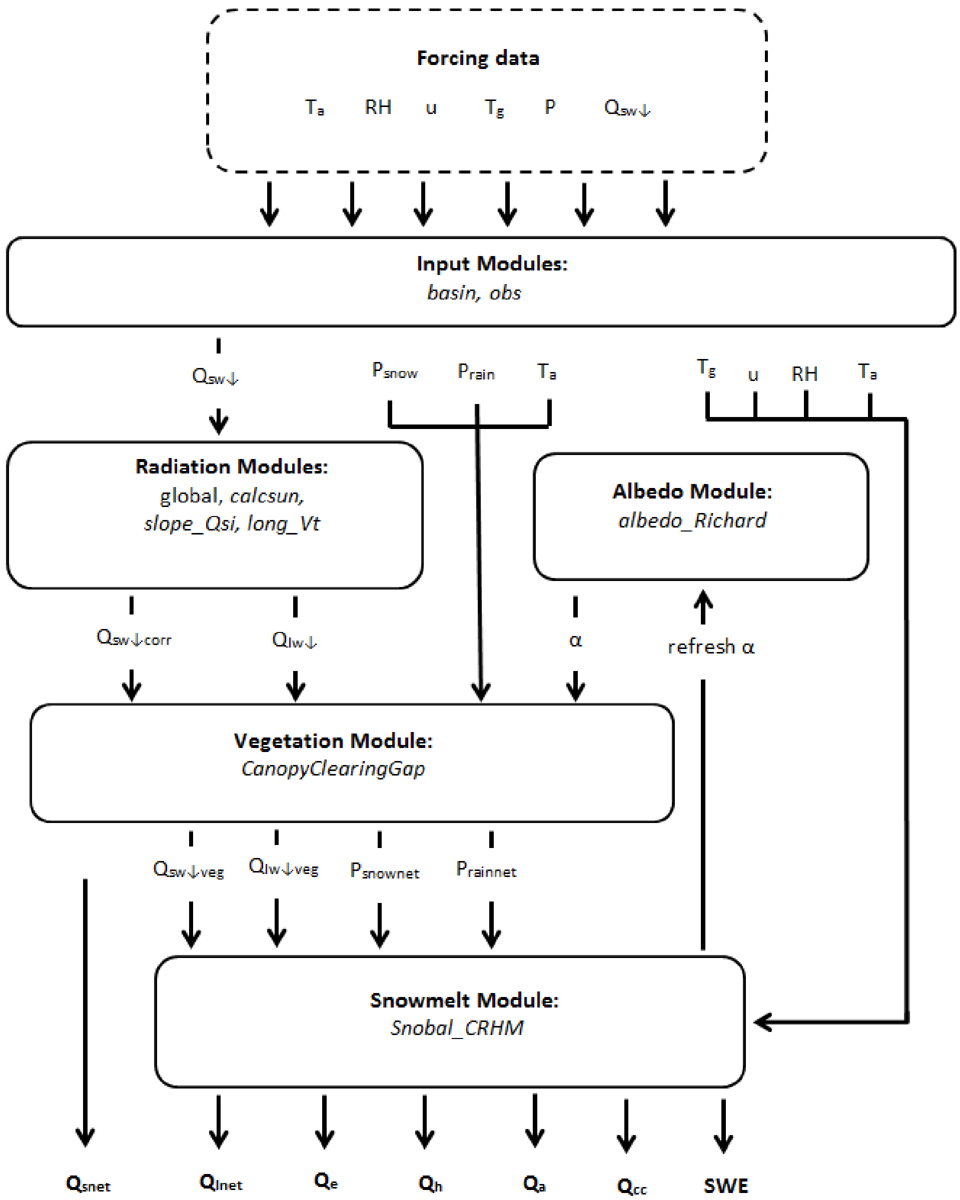

Figure 4: Simplified CRHM structure.

4.4.1 Input Modules

- The *basin* module specifies basic control parameters like catchment and HRU area (obsolete in this study, due to point scale), elevation, latitude slope and aspect.

- Within the *obs* module, the forcing data is assigned to - and if necessary interpolated between - the different HRUs/points. The routine handles the determination of the precipitation phase using a method proposed by Harder and Pomeroy (2013). The module offers the possibility to manipulate air temperature and precipitation amount for climate change simulations.

4.4.2 Radiation Modules

- The *global* module calculates the theoretical clear sky incoming shortwave radiation, where the direct component is computed by a method developed by Garnier and Ohmura (1970) and the diffuse component using a simple approach by List (1968).

- The *slope_Qsi* module then adjusts the measured shortwave radiation from a plane surface to a given slope orientation, using the the ratio of measured to calculated diffuse and direct shortwave radiation (DeBeer, 2012).

- *albedo_Richard* calculates the snowcover albedo as an exponential decay function developed by Verseghy (1991) and modified by Essery and Etchevers (2004). The authors also developed an albedo refreshing function dependent on the ratio of a minimal threshold snowfall amount required to refresh the albedo and the actual snowfall amount.

- The incoming longwave radiation from the atmosphere is estimated in the *long_Vt* module using measurements of shortwave radiation (Sicart et al., 2006). It also accounts for the longwave emission of the surrounding terrain. The terrain view factor could be calculated from a digital elevation model and a terrain emissivity was set to 0.98.

4.4.3 Vegetation Module

The impacts of forest canopy on sub-canopy precipitation and radiation are determined by the *CanopyClearingGap* module. It calculates the shortwave transmittance through the canopy dependent on the solar angle and the leaf area index. It is assumed that the downwelling thermal radiation under the canopy derives from two further energy sources in addition to the atmospheric longwave irradiance: longwave radiation emitted by canopy elements at air temperature and longwave radiation emitted by canopy elements heated above air temperature, due to the extinction of shortwave radiation. Whereby the vegetation temperature is approximated by the air temperature. A dimensionless factor (0.038) is then used to transfer the amount of shortwave energy extinguished in the canopy to thermal radiance from heated canopy parts Pomeroy et al. (2009).

The module includes coupled forest snow interception and sublimation routine after Hedstrom and Pomeroy (1998) and Parviainen and Pomeroy (2000). The interception losses for liquid precipitation are handled using a Rutter model (Rutter et al., 1972) modified by Valente et al. (1997).

4.4.4 Snowmelt Module

The snowmelt model Snobal, developed and described in greater detail by Marks et al. (1998) is used in its modular form within the CRHM platform *Snobal_CRHM* to solve the energy and mass balance of the snowpack (see fig. 1). This module is considered as the core part of this ROS process study. It is using several sub-routines predicting melt, adjusting the mass, thickness and thermal properties at each time-step for a two layer system. The upper active layer has a maximum thickness and interacts with the atmosphere, while the lower layer interacts with both, the soil and the active layer. Snobal calculates the EB for each layer and each time-step. Once a layer reaches 0 °C additional energy results in meltwater production. This meltwater becomes available for runoff once the liquid water content exceeds a threshold $w_{c,max}$. This threshold is defined as the liquid water holding capacity of the void fraction of the snowpack. The liquid water content w_c is calculated as:

$$w_c = \frac{V_{water}}{V_{snow} - V_{ice}} \tag{8}$$

The ratio of liquid water content to the maximal water retention capacity gives the relative saturation of the snowpack. As suggested by Marks et al. (1998) $w_{c,max}$ is set to a low value. In this study a very low value of 0.0001 was use (discussed in section 5.3.1). For ROS events with warm snowpacks well within the melt period, the initial relative saturation was set to 1, for cold snowpacks it was set to 0.

The version of Snobal, which is implemented into CRHM doesn't calculate shortwave radiation fluxes, nor incoming longwave fluxes. This is done by the other modules described above.
The outgoing longwave component is computed using the snow surface Temperature $T_{s,0}$ and is calculated for each time step:

$$Q_{lw\uparrow} = \epsilon_s \sigma T_{s,0}^4 \tag{9}$$

Where ϵ_s represents the emissivity of snow and σ is the Stefan-Bolzman constant (5.67E-08 W/m^2K^4).

The turbulent fluxes of sensible and latent heat Q_h and Q_e, as well as the sublimation rate (includes condensation) E are derived by a bulk transfer approach. Therefore the friction velocity u^* and the Obukhov stability length L are calculated as part of a non-linear equation system as:

$$u^* = \frac{uk}{\ln\left[\frac{z_u - d_0}{z_0}\right] - \psi_{sm}\left[\frac{z_u}{L}\right]} \tag{10}$$

$$L = \frac{u^{*3}\rho}{kg\left[\frac{Q_h}{T_a C_p} + 0.61E\right]} \tag{11}$$

and solved with Q_h and E simultaneously.

$$Q_h = \frac{(T_a - T_{s,0}) a_h k u * \rho C_p}{\ln\left[\dfrac{z_u - d_0}{z_0}\right] - \psi_{sh}\left[\dfrac{z_T}{L}\right]} \tag{12}$$

$$E = \frac{(q - q_{s,0}) a_e k u * \rho}{\ln\left[\dfrac{z_q - d_0}{z_0}\right] - \psi_{sv}\left[\dfrac{z_q}{L}\right]} \tag{13}$$

Where u is wind speed (m/s), k is the von Karman constant ($\approx$0.4), d_0 is the zero-plane displacement height (m; $2 * 7.35 * z_0/3$), z_T, z_q and z_u are measurement heights for temperature, humidity and wind speed (m). As in Reba et al. (2012) the roughness height z_0 was set to 0.0001 for open sites and 0.003 for sheltered forested sites. The stability functions for mass ψ_{sm}, heat ψ_{sh} and water vapor ψ_{sv} are described in detail by Marks and Dozier (1992) and are positive for stable and negative for unstable conditions. The ratio of eddy diffusivity and viscosity for heat is represented by a_h, respectively for water vapor by a_e and as suggested by Brutsaert (1982) set to $a_h = a_e = 1$. T_a and $T_{s,0}$ are the air and snow surface temperatures, ρ is the density of air and C_p the specific heat of dry air. q and $q_{s,0}$ are the specific humidity of air and the snow surface. Since the Obukhov stability length is both, a variable in the turbulent flux calculations and function of them itself, the equations need to be solved iteratively (King et al., 2008). With equation 6, Q_e can be derived from E.

In order to calculate the ground heat flux Q_g, the model uses the assumption of a single soil layer with a thickness equal to soil temperature measurement depth z_g (m). Temperature and vapor pressure gradients are calculated and used to compute heat conduction and vapor diffusion between the soil-snow interface.

$$Q_g = \frac{2K_{es,l} K_{eg} (T_g - T_{s,l})}{K_{eg} z_{s,l} + K_{es,l} z_g} \tag{14}$$

$K_{es,0}$, $K_{es,1}$ and K_{eg} (J/(m K s)) are effective thermal conductivities for the surface, the lower snow layer and the soil. It accounts for heat conduction and vapor diffusion. Beke (1969) classified the alpine soil in MCRB as *Alpine Dystrie Brunisol*. The author found 10.7 % of organic material in the uppermost 20 cm of this silty clay loam soil. Al Nakshabandi and Kohnke (1965) measured thermal conductivity for fully saturated silty loams and found a value of 1.68 J/(m s K), which is used for the calculation of the effective thermal conductivity (see Marks et al. (1998) for details).

Using the same gradient approach, the energy transfer by conduction and diffusion between the upper and lower snow layer can be derived. Marks et al. (1998) found increasing contribution of Q_g (up to 25%) to total melt energy, right after the observed ROS event. The authors concluded that this might be the result of a thinning snowcover and the heating of the soil from solar radiation. However, as it can be seen in equation 14, Q_g is dependent on the snowdepth, leading to high values for very thin snowcover. Where ground temperature measurements where not available, an assumed temperature of 0 °C in 10 cm depth was used to calculate the ground heat flux.

Advected energy from precipitation to the snowpack is calculated as:

$$Q_a = \frac{C_{p-p}\rho_{pp}z_{pp}\left[T_{pp} - T_{s,0}\right]}{t_{step}} \tag{15}$$

Where, ρ_{pp} is the precipitation density (kg/m^3), z_{pp} precipitation depth (m) and T_{pp} (K) is the precipitation temperature. C_{p-p} is the specific heat of precipitation, according to its temperature and phase.

4.5 Applying CRHM

4.5.1 Initial Conditions

Due to the focus of this study on single events, initial snowpack conditions (ISC) prior to the ROS-events have to be specified to permit the computation of snow accumulation, redistribution and melt throughout the whole season. This procedure has several advantages: it dismisses the model uncertainties of the accumulation period, it is less computationally expensive and the model structure can be kept simpler. ISC include depth, density and therefore snow water equivalent, snow temperature, cold content, relative saturation and albedo. A two-layered snowpack with an active layer thickness of 10 cm and no density difference between the layers was set as ISC at all sites. The initial depth, density and SWE was found from the last snow survey prior to the event. Due to the fact, that all ROS events occurred late in the melt season, a saturated, isothermal snowpack with no cold content was assumed. Where albedo measurements were not available, the albedo was set to 0.6 for old wet snow (King et al., 2008). Intercepted precipitation prior to the event was assumed to be 0. Table 3 shows the ROS events and the initial snowpack conditions.

Table 3: Initial snowpack conditions

start event	Location	ISC date	density [kg/m^3]	SWE [mm]	α [-]
June 18th 2011	FR	June 14th	278	114.2	0.58
	FR_S	June 14th	400	416.5	0.58
	FR_SF	June 14th	386	314.3	0.58
May 13th 2013	FR	May 2nd	326	378.2	0.85
	FR_S	May 2nd	266	592.5	0.85
	FR_SF	May 2nd	197	378.1	0.85
	FR_N	May 2nd	300	156.1	0.85
	LES	May 12th	400	400.0	0.85
June 19th 2013	FR_S	June 13th	451	442.0	0.6
	FR_SF	June 13th	513	256.5	0.6
	LES	June 18th	400	215.0	0.6

4.6 Model Validation

To test the ability of the model to represent physical processes in a correct way and to justify a sensitivity analysis during ROS conditions, the model results are validated using field observations. Those observations include:

- time series of sonic ranger snowdepth.

- measurements of SWE from snow pillow at the LES site.
- results of the snow survey after the event.

The root mean square error (RMSE) of the model to the observation time series is computed as:

$$RMSE = \sqrt{\frac{\sum_{i=1}^{n}(X_o - X_m)^2}{n}} \tag{16}$$

Where X_o is the observed value (of snowdepth $z_{s,o}$ or SWE SWE_o), X_m is the modeled value ($z_{s,m}$ or SWE_m), n is the number of pairs and i is the time step.

To compare the change in snowdepth (z_s) and SWE of the observation data and changes predicted by the model, simple absolute ($\Delta X_m - \Delta X_o$) and relative differences ($\frac{\Delta X_m}{\Delta X_o} * 100 - 100$) are calculated. Negative values indicating therefore an underestimation of the decline in snowdepth or SWE and positive values vice versa. These z_s and SWE changes were computed between the snow surveys and between the onset and the end of the ROS event respectively.

4.7 Sensitivity Analysis

The sensitivity analysis is based on the observed meteorological data of the June 2013 event at the Upper Clearing, Upper Clearing Tower and Upper Forest site (see fig: 2 and table 2). Even though there was no snowcover present during the event, these sites were chosen since they provide input data for different land use units. Four different land use classes (a) dense coniferous forest (, b) sparse coniferous Forest, c) 50 m wide gap in a dense coniferous forest and d) open land form) are analyzed. Table 5 shows the origin of the forcing data for these land use scenarios. Parameters specifying these land use classes are shown in table 4. In order to point out differences in ROS event and non-event sensitivities, the main event days (June 19^{th} to June 21^{st} 2013) and pre-event condition (June 13^{th} to June 16^{th} 2013) are compared.

Table 4: land use scenarios

parameter	a) Dense Forest	b) Sparse Forest	c) Gap
canopy albedo α_c [-]	0.17	0.17	0.17
diameter [m]	-	-	50
LAI [-]	2.5	1.25	2.5
max. interception load [kg/m^2]	6.6	2	-
canopy height [m]	20	3	20

Compared to the data from the Fisera Ridge station (fig. 8), the UC and UF station show warmer air temperatures (fig. 5). On average the event period shows an air temperature of 5.8 °C with little difference between the UC (gap & open) and UF site (dense & sparse forest) and almost no diurnal oscillation. During the pre-event period, however, air temperatures show a distinct diurnal pattern with a slightly attenuated regime for the UF site. During the ROS event constantly high humidity values, almost saturated conditions are measured at both stations. RH values during the pre-event fluctuate with the influence of the air temperature between 38 % at day and 86 % in the night.

In order to obtain wind speed values above the snowpack for an open site the above canopy anemometer readings from UCT are used. The wind speed increases slightly during the event (3.5 m/s peak) compared to the pre-event period (2.6 m/s peak) above the canopy at 20 m. With the assumption of a logarithmic wind profile the near ground wind speed could be calculated for the open land use class d) as well as to derive the wind speed at the sparse forest class c) by applying equation 7 (attenuation coefficient of 1). The so derived values at the sparse forest site are comparable in magnitude to the values measured at UC. The lowest value are measured at the UF site. Here, wind speed peaks are as small as 0.5 m/s.

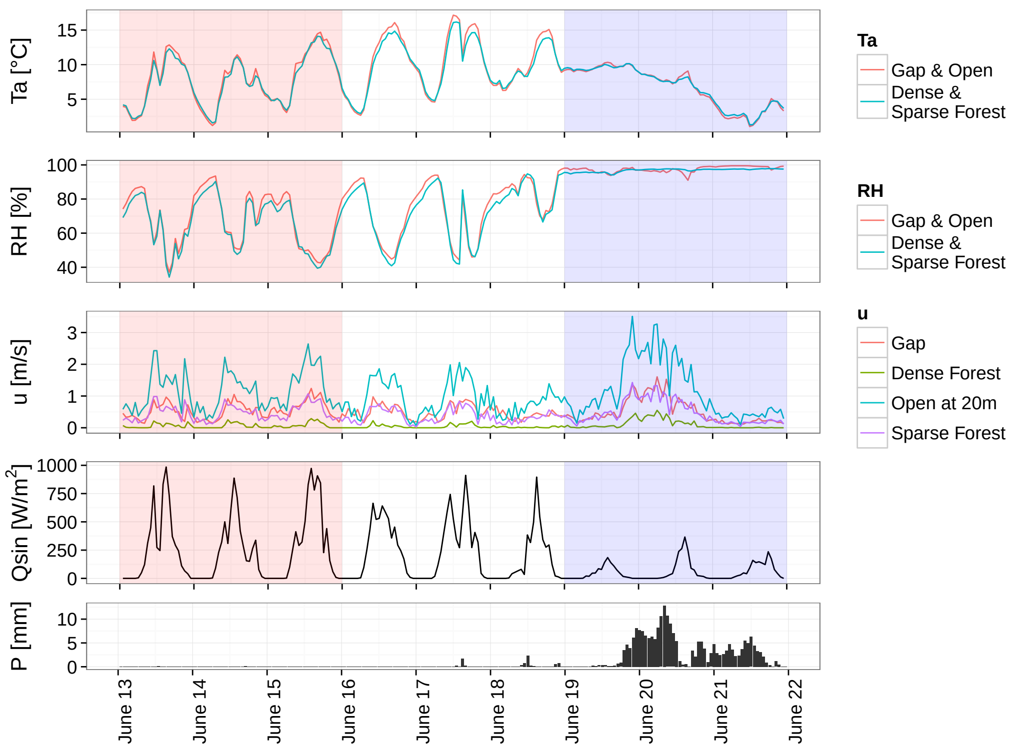

Figure 5: Forcing data for model sensitivity analysis. The red shade indicates the pre-event period, the blue shade shows the event period.

Table 5: Measurement location of forcing data and the assigned land use classes

parameter	a) Dense Forest	b) Sparse Forest	c) Gap	d) Open
T_a	UF	UF	UC	UC
RH	UF	UF	UC	UC
P	UC	UC	UC	UC
Q_{si}	UCT	UCT	UCT	UCT
u	UF	UCT (equ: 7, a=1)	UC	UCT

Throughout all land use classes the initial conditions were set to a saturated, isothermal two-layered snowpack of 500 mm SWE with a mean density of 400 kg/m^3. The active layer thickness was set to its maximum of 10 cm. To determine the influence of topographic characteristics and changing meteorological conditions on the snowpack energy balance, model parameters, forcing data and ISC are modified for all of the four land use classes. These modified parameters include:

- leaf area index: in addition to the four simulated land use classes, the effect of a varying LAI as a proxi of stand characteristics was investigated. For this analyisis all other vegetation describing parameters were set to the dense forest values, while the LAI was increased from 0 to 3 by steps of 0.5.

- initial snowpack conditions: snow temperatures were varied in 1°C steps from -10 °C to 0 °C of the active snow layer and 30 % higher temperature values at the lower snowlayer (the use of a multiplier is applicable here, since the temperature difference to the melting temperature is of interest). The cold content for each layer was then computed using:

$$Q_{cc} = -c_i * \rho_w * z_s * (T_s - T_m) \tag{17}$$

  Where c_i is the heat capacity of ice (2102 J/kg K), ρ_w is the density of water, z_s is the snowdepth, T_s is the mean snowpack temperature and T_m is the melting temperature (0 °C) (Dingman, 2002).

- slope and aspect: in order to asses the influence of aspect and slope on the ROS energy budget, these parameters are changed within the *basin* module. The aspect is changed in eight steps from 0 ° to 325 ° and the slope in 8 steps from 0 ° to 42 °. Due to the semi-distributed character of the model, there is no directional dependency of the wind profile. Therefore a change in slope and aspect solely influences processes dependent on the solar angle.

- air temperature: Nogués-Bravo et al. (2007) evaluated five Atmosphere Ocean General Circulation Models (AOGCM) and provide an overview over the surface air temperature changes in mountainous environments.

For Intergovernmental Panel for Climate Change (IPCC) relatively pessimistic emission scenario A1FI, which accounts for a fossil fuel intensive world of rapid economical growth, the authors found air temperature increases of 4.1°C for the high-latitude North American regions by the year 2055. In this study air temperature values are stepwise increased to Δ 5°C, in order to assess the effects of global warming and decreased Δ -10°C to simulate colder ROS events. The results of climate change models suggest, that the relative humidity will stay constant with increasing air temperature. This is certainly true for ROS conditions. This is taken into account, since an increasing air temperature and a constant vapour pressure *ea* would lead to a decreasing relative humidity. Therefore RH will be kept constant instead. Air temperatures can be varied inside the *obs* module.

- precipitation: the precipitation amount will be varied using a build in multiplier function in the *obs* module. The amount will be changed to 0%, 25%, 50%, 100% 125%, 150%, 175% and 200%.
- wind speed: Changes to wind speed data are done outside CRHM. Measured values are modified in 8 steps from 25% to 200% of the observed value. Since the change in wind speed is a relative one, absolute velocity differences between the scenarios are greatest in the open and smallest in the dense forest. This relative approach is believed to be a more realistic representation, since the impact of an actual storm will always be smaller in the forest than in the open.

All parameter changes were performed for both, an isothermal saturated snowpack and a cold dry snowpack (-5°C in active layer, -3.5°C in the lower layer). In addition to these single parameter changes aspect and slope, air temperature and precipitation, as well as air temperature and wind speed are varied simultaneously. With the above described parameter combination, two initial snowpack conditions and the four land use classes for both, the event and the pre-event period, 5383 model runs were computed in this sensitivity analysis. In order to run all these parameter sets, a fortran code had to be applied to execute CRHM in a batch run. The files storing the parameter sets were modified and rewritten using the statistical software *R*.

The sensitivity of the EB to the described parameters is analyzed by taking a closer look to:

- the changes of total cumulative energy and the resulting meltwater release.
- changes of energy fluxes of the individual EB components.
- the changes of relative contribution of these components to the cumulative energy input.
- differences between the land use classes.

To analyze the 1^{st} order sensitivity of the variable B (e.g. cumulative melt) to the variable A (e.g. air temperature) the impact of a change in variable A (ΔA) for the resulting change in variable B ($\Delta B = B_{sens} - B_{ctl}$) is investigated. Where the sensitivity run B_{sens} is the result to a change in A and the control run B_{ctl} is the result for a defined case (e.g. ΔA=0 and potentially a second parameter ΔC=50% (e.g. precipitation))(Seneviratne et al., 2010).

$$\frac{dB}{dA} \approx \frac{\Delta B}{\Delta A} \tag{18}$$

To asses the impact of this sensitivity on the response variable B, $\frac{\Delta B}{\Delta A}$ is multiplied by the range of the parameter (A_{max}-A_{min}).

The 2^{nd} order sensitivity - here defined as the impact of a parameter C to the sensitivity $\frac{\Delta B}{\Delta A}$ - is calculated similarly as:

$$\frac{\frac{\Delta B}{\Delta A}}{\Delta C} * (C_{max} - C_{min}) \tag{19}$$

Accordingly, the overall impact is then calculated by multiplying with the range of A.

5 Diagnosis of ROS Events

5.1 Event Characterization

June 2011 Two consecutive rainfall events were identified in the month of June 2011. The first event occurred during the daytime of June 17^{th} (11:00 - 17:00). A total of 15.5 mm precipitation fell during this period at the Fisera Ridge site. A comparison with other precipitation gauges in the basin shows a significant increase in precipitation with increasing elevation (1.2 mm/100 m, r^2: 0.86)). The second part of the event occurred during the night from June 18^{th} to June 19^{th} (18:00 - 4:00). With a cumulative rainfall amount of 17.7 mm, the event showed no precipitation-elevation gradient (r^2: 0.12). Both events are accompanied by high humidity (RH: 85 %) and about the same average air temperature readings of 4.7 °C to 4.6 °C. Wind speed maxima during the events are 5.4 m/s and 4.7 m/s. The events follow a period of slightly colder temperatures with a mix of wet snow and rain, that was not defined as a ROS period due to its high fraction of solid precipitation.

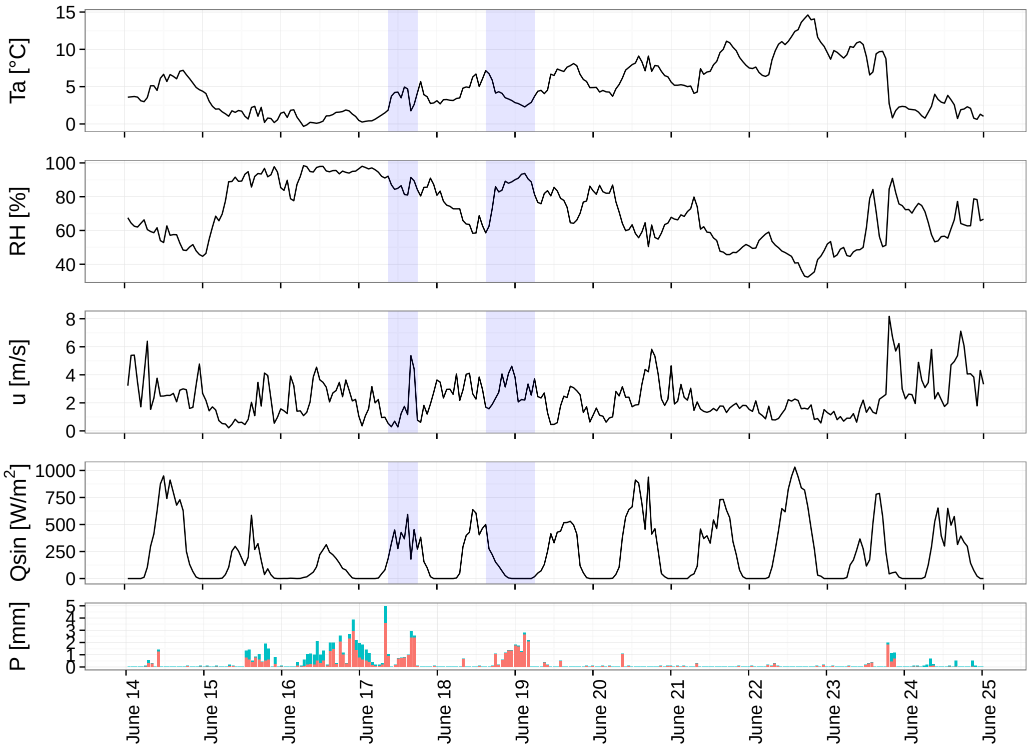

Figure 6: Fisera Ridge: Meteorological conditions for the ROS event in June 2011. The blue shading indicates the event periods.

May 2013 During the period from May 12^{th} to May 13^{th}, a total of 17.7 mm of rain fell on the snowpack at the Fisera Ridge site. A strong relation between precipitation and elevation could be found for this event (1.4 mm/100 m, r^2: 0.99). The warm initial air temperatures of about 12 °C dropped to about 4.5 °C during the event period. The rainfall was accompanied by comparatively low relative humidity values of about 75 to 80 %. Between the two rain pulses the relative humidity dropped to 68 %. The mean wind speed of 2.7 m/s (peak of 5.1 m/s) can be described as moderate compared to pre- and post-event conditions. The sudden increase of the cloudiness can be seen in the abrupt decline of the shortwave radiation readings at May 12^{th}. During the day of the 13^{th} the pyranometer measured only half (around 330 W/m^2 peak) of incoming shortwave radiation compared to pre-event days.

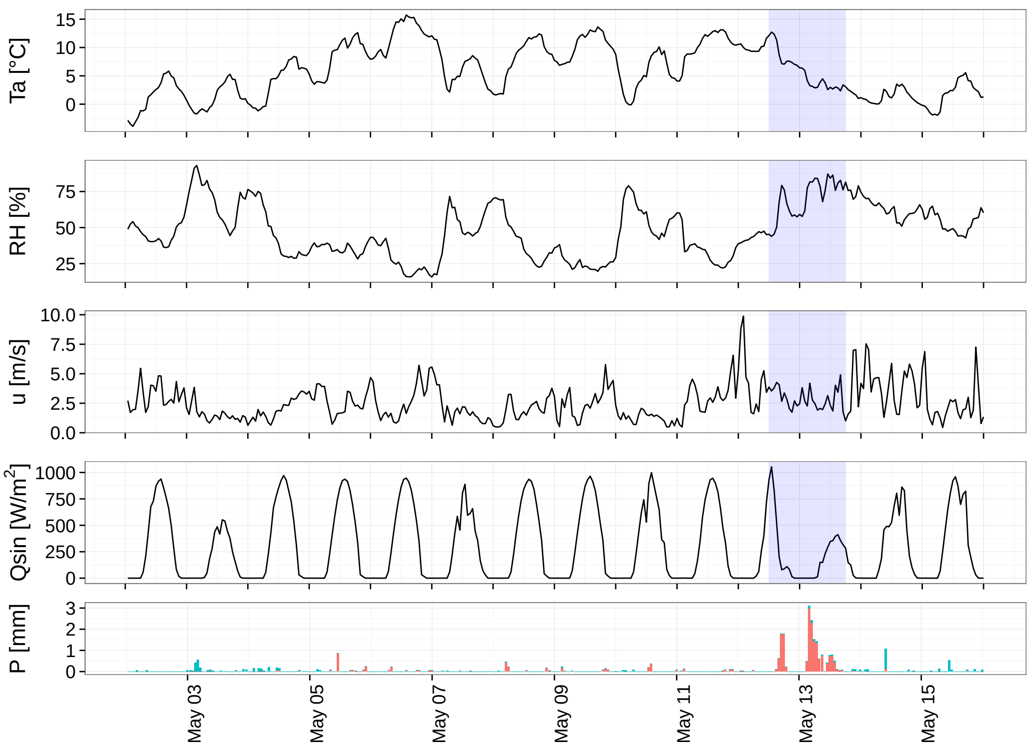

Figure 7: Fisera Ridge: Meteorological conditions for the ROS event in May 2013. The blue shading indicates the ROS period.

June 2013 Heavy rainfall started on June 19^{th} and continued for three days till June 21^{st}. Together with meltwater origin from alpine snowmelt this rain event triggered a flood in southern Alberta. A total of 236 mm of precipitation fell during this period at the Fisera Ridge site. The precipitation amount was even higher at the Little Elbow Summit site, where 307 mm of cumulative precipitation were measured. However, no correlation of rainfall amount to elevation could be observed during this remarkable event (r^2: 0.085). The evolution of the incoming shortwave radiation illustrates how intense the cloud cover must have been during these three days. On June 19^{th} as little as 80 W/m^2 reached the surface. Air temperature readings dropped from 7.4 °C to about 1.2 °C during the event, leading to an increasing fraction of solid precipitation with time. The air humidity readings show fully saturated conditions for the longest part of the event. In the afternoon of June 21^{st} the relative humidity started to decreased to about 80 % in the morning of June 22^{nd}. With a reading of 5.6 m/s, the wind speed peaked at the 21^{st} of June.

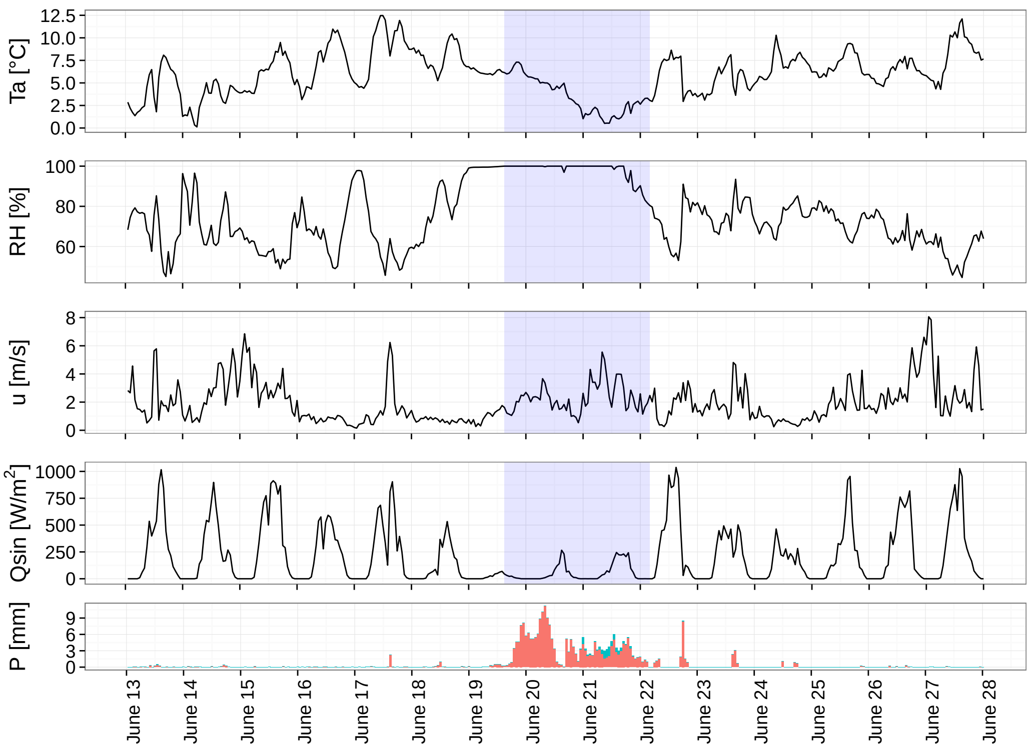

Figure 8: Fisera Ridge: Meteorological conditions for the ROS-event in June 2013. The blue shading indicates the ROS period.

5.2 Model Results

The model performance is evaluated for the three events described in section 5.1 using snowdepth sonic ranger (SR50) or snow pillow measurements whenever available, as well as the results of the manual snow survey following the event. Due to the spatial variability within the same response class, the illustrated of snowdepth and SWE, as found from the snow surveys, is displayed by the median and the lower and upper quartile.

5.2.1 June 18^{th} 2011

For the event in June 2011, the ROS criteria (section 4.3) were met at three alpine sites (FR, FR_S and FR_SF). Figure 9 shows the model results and snowpack observations at Fisera Ridge main station. It can be seen that the automated snowdepth measurements at the station lie outside the interquartil range of the value distribution obtained from the snow survey. To evaluate the model results to both measurements is therefore difficult.

The model seems to perform well and is able to reproduce the post-event snow survey measurements at June 22^{nd}. It underestimates the snowdepth loss only by 1 cm (-3.3 %) and overestimates the ΔSWE difference by 7 mm (6.5 %) at the FR site. During the first event part the model shows a slight decline in SWE and a steeper decline in snowdepth, accounting for the densification of the snowpack. The SR50 readings, however, show no significant response, resulting in a huge relative error of 2688 % (5 cm). The second part of the event reveals greater differences in model and observation. According to the measurements, the snowdepth increased in the early morning of the 19^{th}, while the model predicts about 5 mm of melt. The snowdepth measurements at the south face of Fisera, however, show no increase in snowdepth for this period (fig. 10), leading to the conclusion that the measurements are influenced by the local wind field and snow redistribution around the main station. The model was not able to replicate the dynamic shown by the snowdepth measurements prior the the first event part at the FR_S site. While the SR50 readings show an increase in snowdepth, modeled z_s values decline. This indicating that either the fraction of solid and liquid precipitation in this period could not be estimated correctly, or relocation of blowing snow occurred. The model overestimates Δz_s and underestimates ΔSWE by 14 cm (51.6 %) respectively -11 mm (-9.3 %). During both event parts the snowdepth decline is overestimated by 2 cm (95 and 110 %). At the FR_SF site the model is not able to predict the post event snowpack. Here, the depth loss and melt are overestimated over the whole modeled period by 33 cm (260 %) and 59 mm (109 %) respectively.

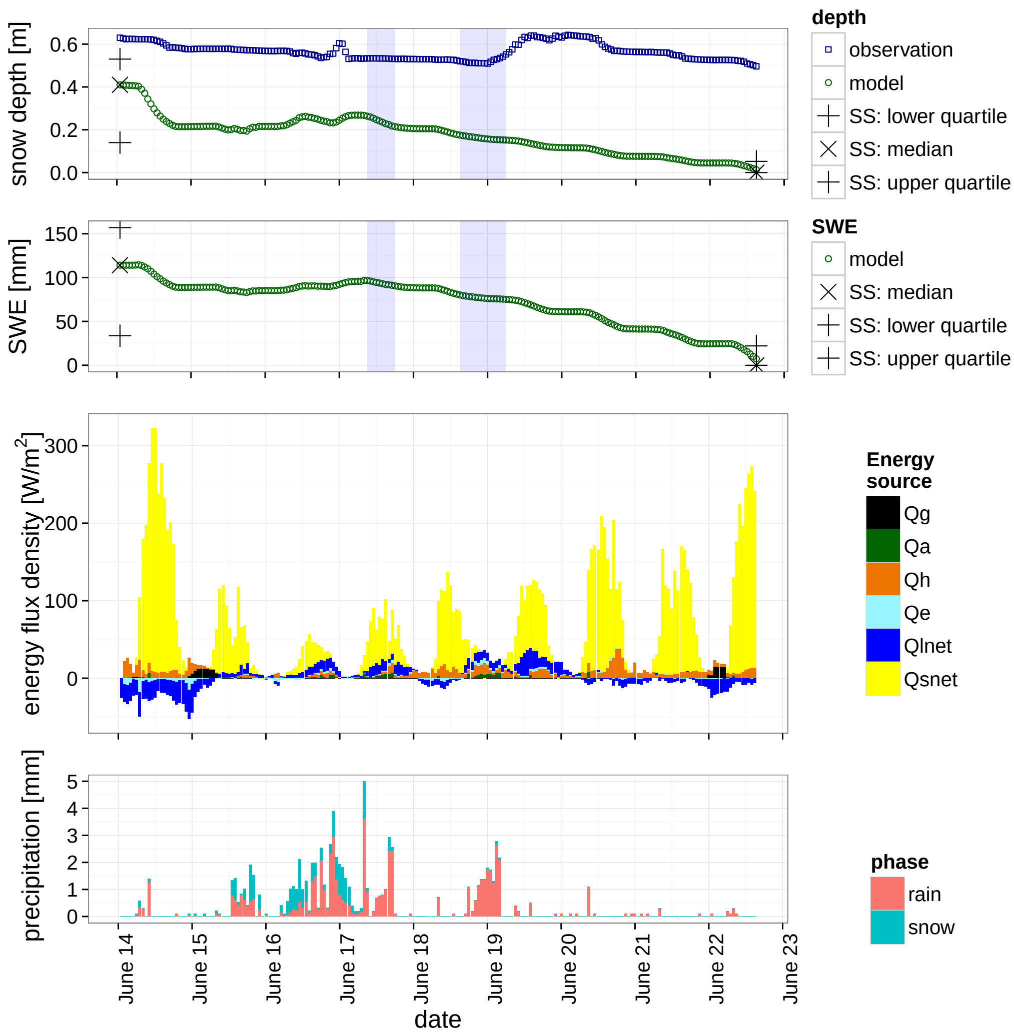

Figure 9: Fisera Ridge: ROS-event in June 2011. Modeled and observed snowdepth (sonic ranger (observation) and snow survey (SS)), SWE and precipitation, as well as the time series of the modeled energy fluxes.

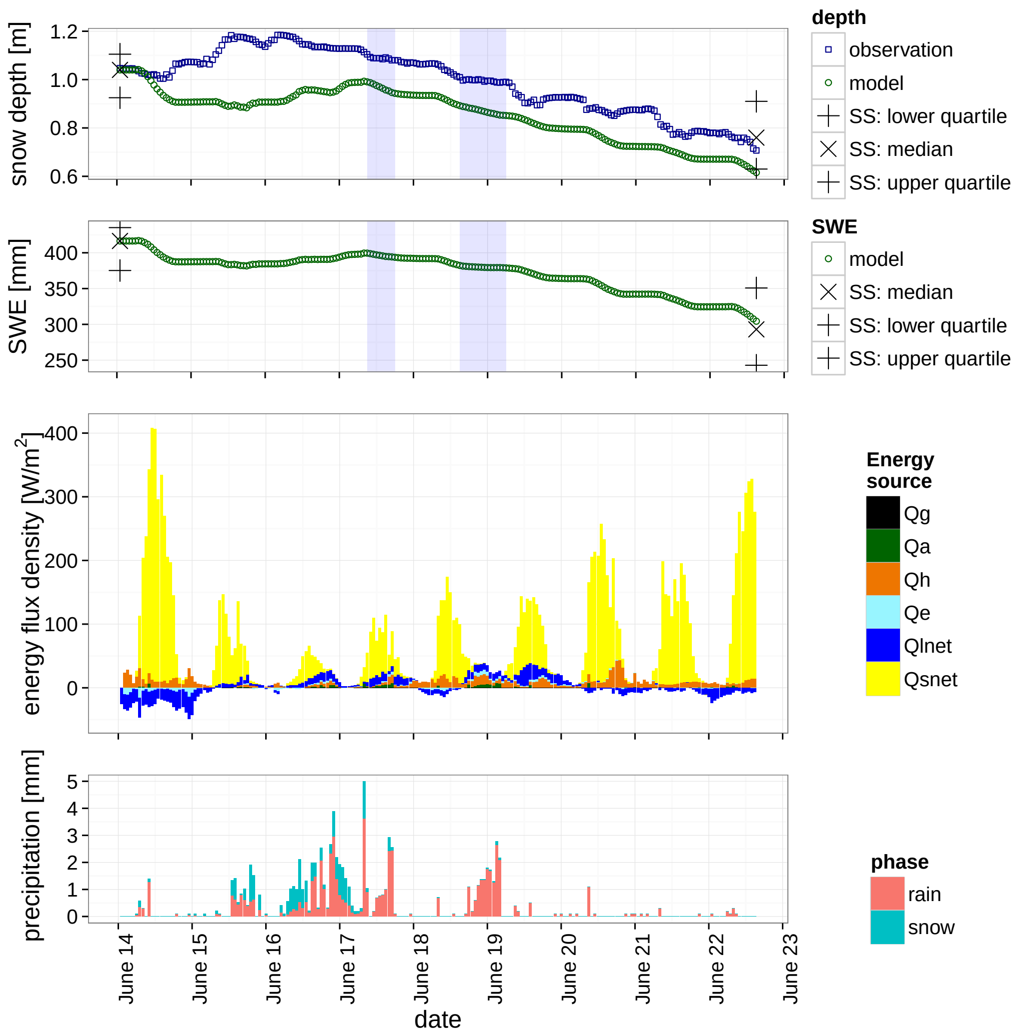

Figure 10: Fisera Ridge South: ROS-event in June 2011. Modeled and observed snowdepth (sonic ranger (observation) and snow survey (SS)), SWE and precipitation, as well as the time series of the modeled energy fluxes.

According to the model results, the EB during ROS periods differs considerable compared to clear sky periods (fig. 11). Even though the net shortwave radiation decreases drastically to 25 % of the net shortwave radiation at the clear sky day (14^{th} of June), Q_{snet} is still the main energy source during the first event part. Since the second precipitation event started late in the day and occurred mainly during the night, the total energy available for melt was found to be lower during this event part, compared to the the available melt energy during the previous daytime-event. Compared to non-event nights, however, the energy available to melt was found to be much higher. At the onset of both ROS events Q_{lnet}, as well as Q_e become positive, providing an additional energy input. The turbulent fluxes, especially the latent heat flux, are small during the first event part and contribute together only 5 to 8 % to the total energy. During the second event part they are slightly higher and accounting for 35 to 55 % of the total energy.

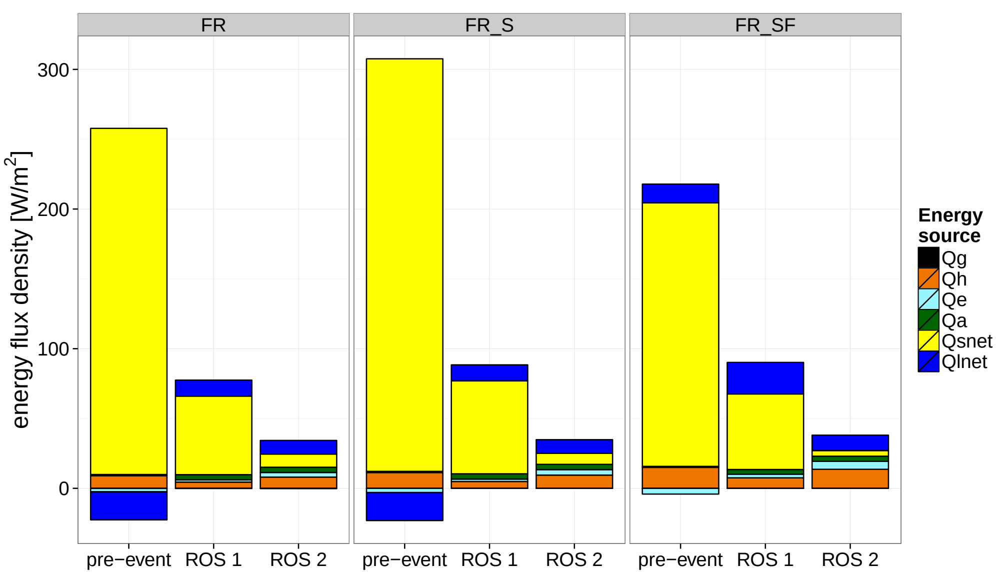

Figure 11: Modeled mean energy fluxes for the June 2011 event and pre-event period at Fisera Ridge (FR), South (FR_S) and South Forest (FR_SF) site.

5.2.2 May 13^{th} 2013

Figure 12 and 13 show the results of the model runs for the May 2013 event at the FR and LES site. During the event from the 13^{th} to the 14^{th} of May 2013 the model was able to predict the decline in z_s measured by the SR50 with a difference of -0.01 cm (-5.8 %) at FR. For the whole modeled period, the model performs well and reproduces the Δz_s and ΔSWE with errors of -4 cm and -5,5 % respectively and 40.8 mm and 19.9 % compared to the values obtained by the snow surveys at the FR site. At the FR_N, FR_S and FR_SF site, where no SR50 measurements were available, the model shows differences to the post-event snow survey SWE of 3.5 mm (4.8 %), 232.1 mm (1589 %) and 327 mm (-282 %).

The post-event snow surveys at FR_S and FR_SF site show a higher variability as well as a higher mean in SWE compared to the pre-event survey. Pomeroy and Gray (1995) pointed out that density and depth are correlated, therefore the a regression function between those two parameters was used (if $r^2 \geq 0.6$) to calculate the areal SWE from the snow surveys. Here, the increase of the variability of SWE, which was found between the two surveys, origins partly from this regression, which showed a negative correlation of depth and density found at the pre-event survey and a positive correlation at the post-event survey. However, this does not explain the overall increase of SWE. The accumulation of snow due to redistribution at the south side seem unlikely, given the results of a CRHM set up using the semi distributed HRU approach and accounting therefore for blowing snow processes. The model suggests that during the observed period only very little snow was transported. According to the model only about 0.4 mm were relocated from the north face and the ridge top to the south facing site of the ridge. Therefore the increase in SWE can not be explained other than by the fact, that different operators conducted the post-event survey. It is likely that they followed a different transect path down the south slope into the forest, where the snowdrift was deeper.

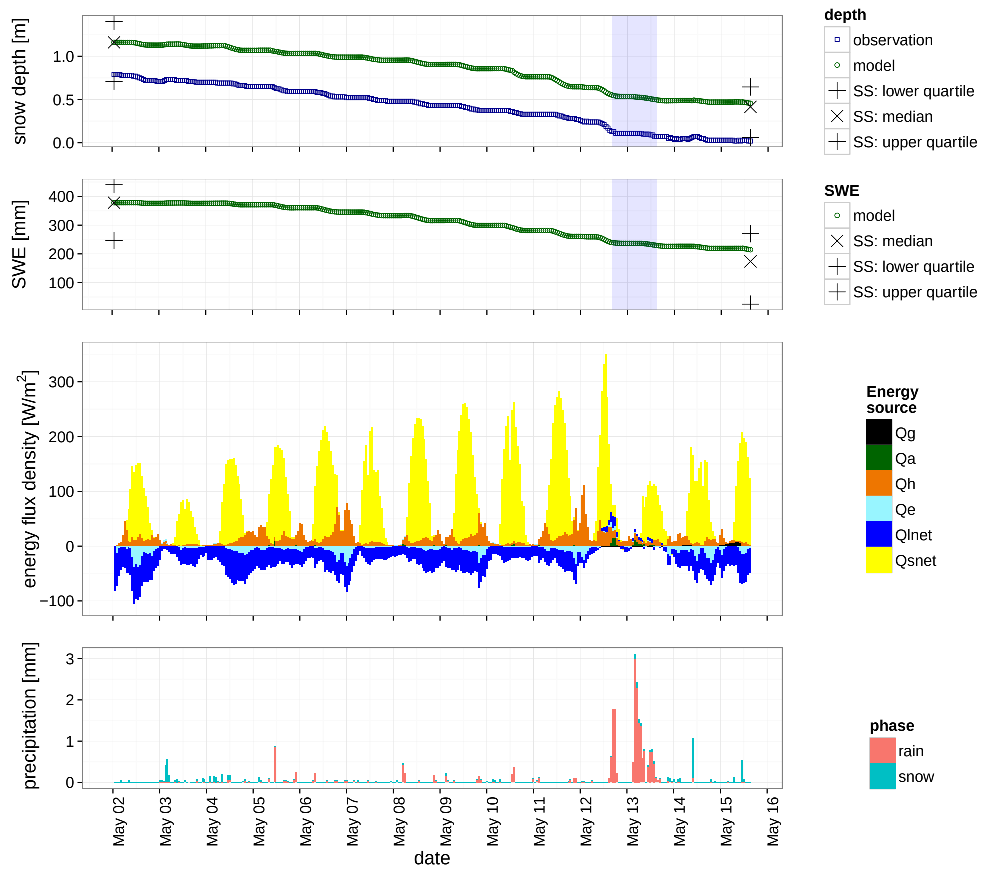

Figure 12: Fisera Ridge: ROS-event in May 2013. Modeled and observed SWE (snow pillow), precipitation and the time series of the modeled energy fluxes.

Due to the employment of a snow pillow at the LES station, model runs could be started at the onset day of the event. During the event the model shows reasonable agreement with the snow pillow data, resulting in a RMSE during the event of 1.5 mm. From the beginning till the end of the rainfall event the model underestimates the change of SWE by 3.4 mm (-38 %). In the subsequent course of the snowpack evolution, model results and measurements differ progressively. Interestingly the trajectory of measured SWE values doesn't show any correlation with the precipitation measurements after the 15th of May, but rather a diurnal pattern. The model suggest a negative EB during the night time in this period due to the loss of longwave radiation. The resulting cooling of the snowpack, which influences the snow pillow readings through bridging effects, could be a possible explanation. An error in the gauge is another possibility.

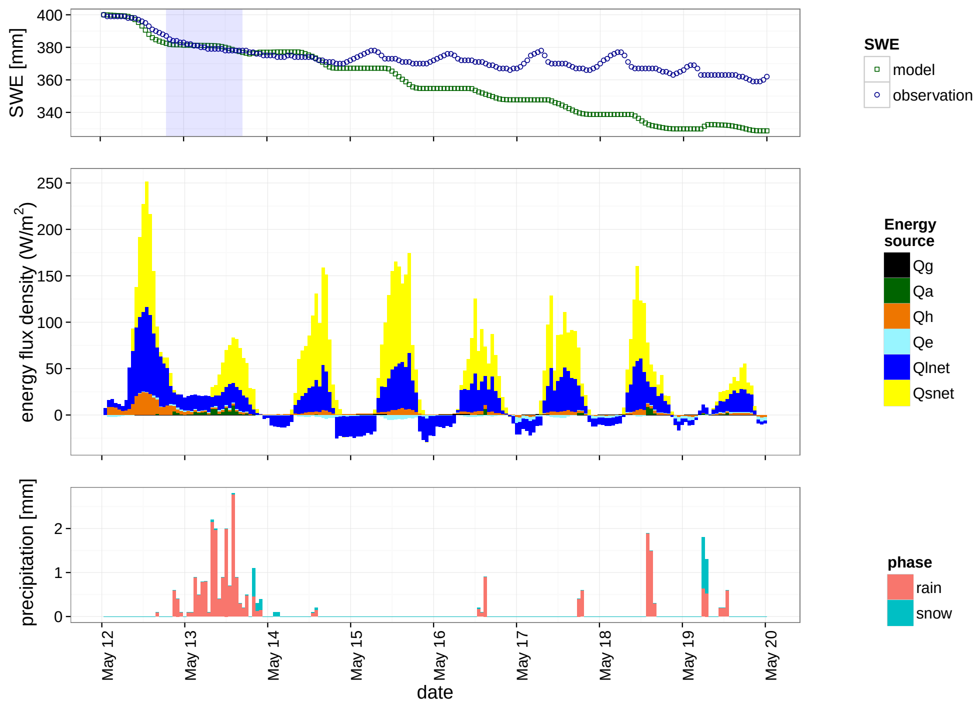

Figure 13: Little Elbow Summit: ROS-event in May 2013. Modeled and observed snowdepth (sonic ranger (observation) and snow survey (SS)), SWE and precipitation, as well as the time series of the modeled energy fluxes.

The average energy fluxes of the EB components for the ROS event and the previous day are shown in figure 14. The major energy input origins from the net shortwave radiation in both, the pre-event and the ROS period for all sites. Thereby the influence of the aspect on Q_{snet} can be seen when comparing the FR, FR_N and FR_S site. The EB in the dense forest at the LES site, however, is equally strongly influenced by net longwave radiation. At LES a high incoming longwave radiation flux, due to the extinction of shortwave radiation at the canopy, leads to comparably high Q_{lnet} values. The three open sites FR, FR_N and FR_S show a similar energetic composition. Pre-event conditions lead to a negative net longwave and a negative latent heat flux at those sites. Throughout all sites the sensible heat flux contributes significantly to the pre-event EB (14 to 42 %). The model predicts a positive but very small latent heat flux during the event as a result of the, compared to other ROS events, rather low RH values. The advected energy flux from the precipitation accounts for only up to 10 % of the EB.

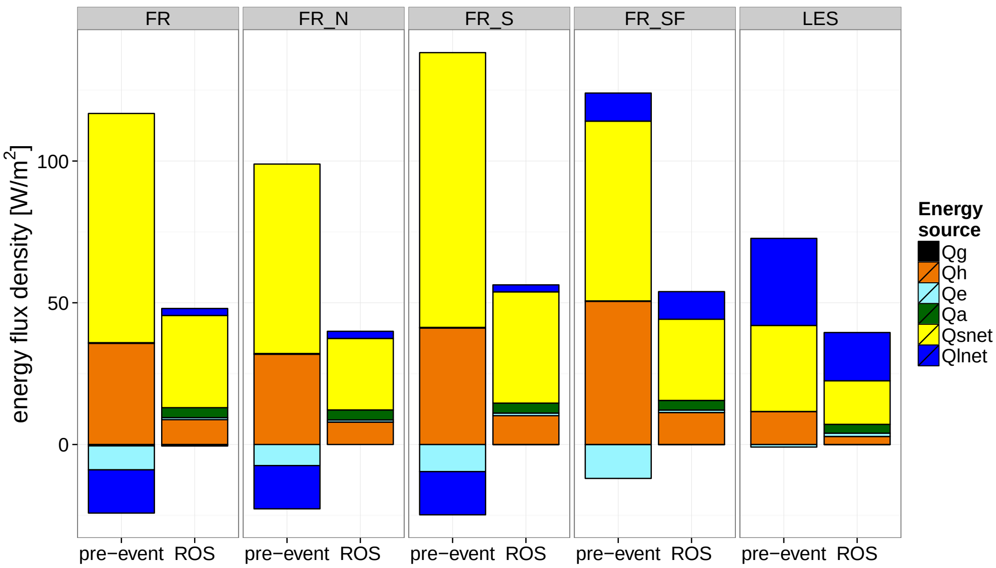

Figure 14: Modeled energy fluxes for the May 2013 event and pre-event period at Fisera Ridge (FR), North (FR_N), South (FR_S), South Forest (FR_SF) and Little Elbow Summit (LES) site.

5.2.3 June 19th 2013

Model results for the June 2013 event at the FR_S site are summarized in figure 15. The model is able to predict the development of the snowpack well at the 26th of June with a marginal depth difference of 0.4 cm (0.6 %) and a ΔSWE difference of -25 mm (-7.9 %) compared to the median of the manual snow surveys. The model results show as well a good agreement with the observation of the snowdepth time series prior to the event. However, according to the results, the model underestimates the snow depletion during the event. A Δz_s difference of 9 cm (51 %) between model and observation was found from the onset of the ROS till snow accumulation sets in. At the FR_SF site the model shows a good performance over the 14 day period. Snowdepth and SWE decline could be predicted within errors of -4 cm (7.8 %) and -16 mm (-6.3 %) respectively.

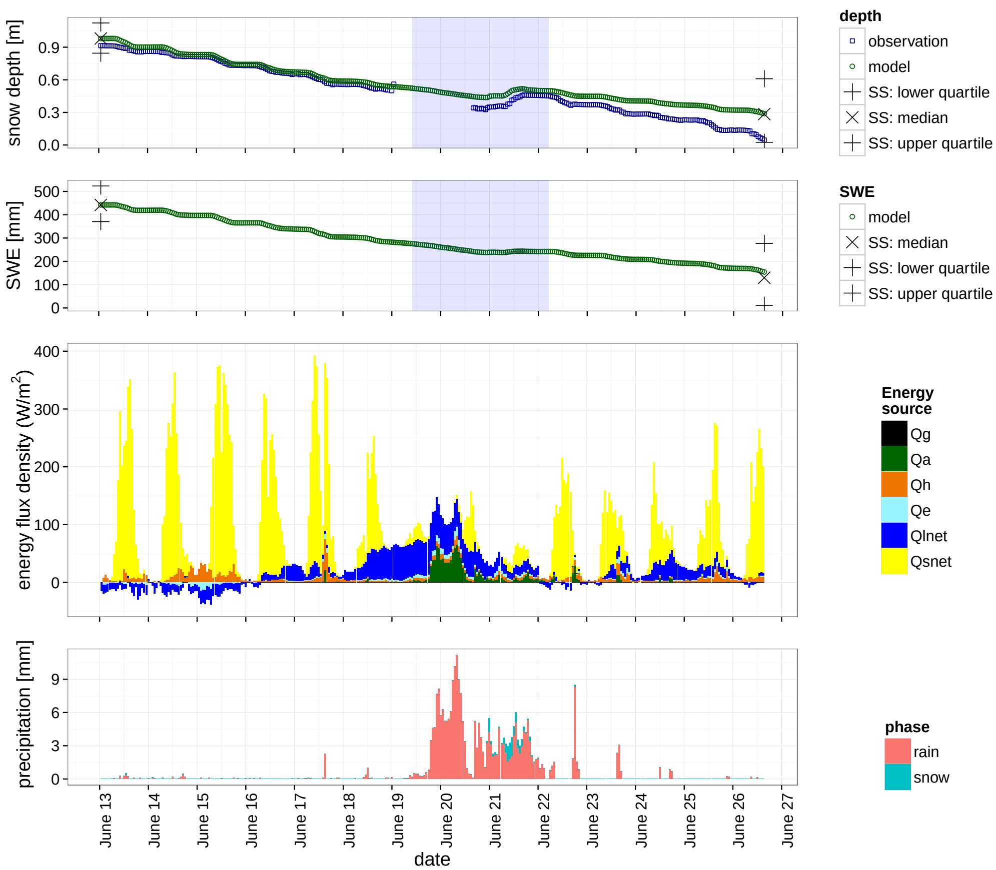

Figure 15: Fisera Ridge South: ROS-event in June 2013. Modeled and observed snowdepth (sonic ranger (observation) and snow survey (SS)), SWE and precipitation, as well as the time series of the modeled energy fluxes.

At the Little Elbow Summit site (fig. 16) the model start to differ from the observed SWE measurements at the onset of the event. The model underestimates the snowmelt and therefore the minimum SWE at June 20^{th} by 19 mm (-37 %). The subsequent accumulation during the later part of the event could be reproduced well in both, timing and magnitude. RMSE over the whole modeled period was found to be 11 mm and 7.9 mm during the event itself.

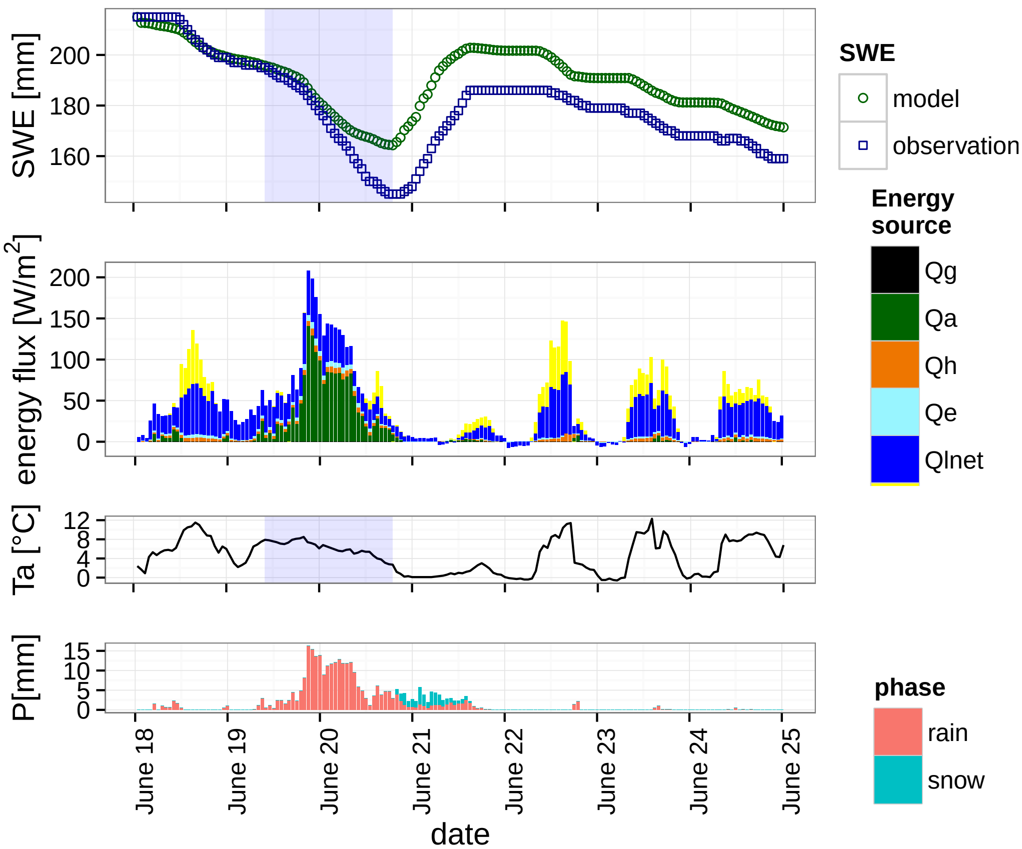

Figure 16: Little Elbow Summit: ROS-event in June 2013. Modeled and observed SWE (snow pillow), precipitation and the time series of the modeled energy fluxes.

The model results show, that during the pre-event condition the EB is mainly influenced by shortwave radiation (fig. 17). Whereas the main energy input during the event was provided by the longwave radiation, except at the LES site. Here, the very heavy rainfall combined with mild temperatures dominated the total energy available for melt through advected heat transfer. At all sites Q_a provided significant amounts of energy and accounted for

25-44 % of the EB. The course of the modeled energy fluxes shows a strong decrease in the shortwave radiation during the event. At the open sites, net longwave radiation and latent heat flux are directed away from the snowpack during pre-event conditions, resulting in just a slightly higher total energy available for melt than during ROS conditions. The sensible heat flux decreases during the event period compared to pre-event conditions. Because of condensation during the event and the resulting release of latent heat, the total contribution of the turbulent fluxes increases during the event.

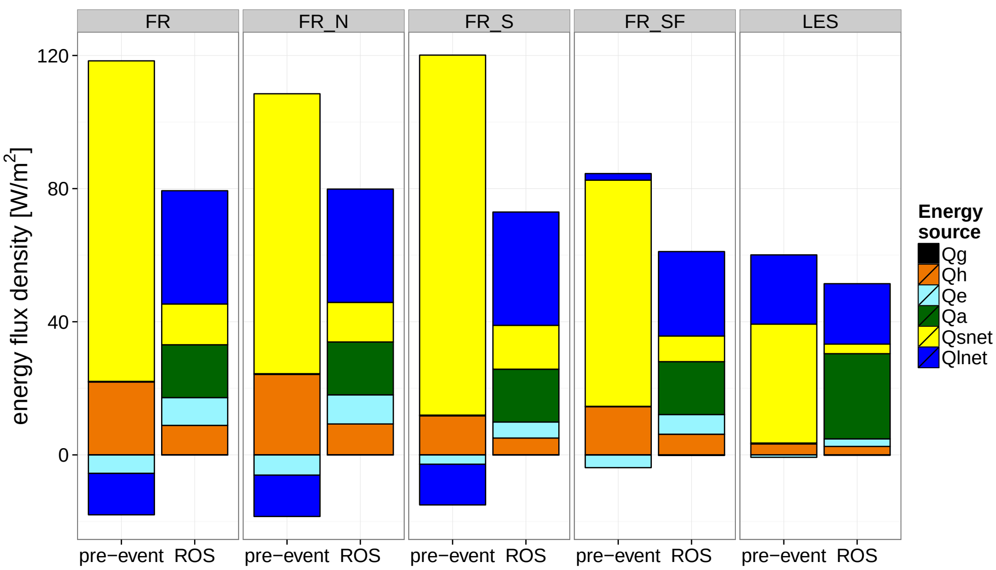

Figure 17: Modeled energy fluxes for the June 2013 event at Fisera Ridge (FR), North (FR_N), South (FR_S), South Forest (FR_SF) and Little Elbow Summit (LES) site.

5.3 Discussion

5.3.1 Uncertainties

To assess the suitability of the model for further sensitivity analysis, the model performance described in section 5.2 has to be put into the context of possible uncertainties. The model results and its validation are subject to three different sources of uncertainty. These sources include: uncertainty of forcing data, uncertainty of validation data and uncertainty from the model and its parametrization.

Uncertainty of forcing data All measurement techniques are subject to uncertainty. This is especially true, when recording variables in the environment, such as meteorological data in alpine conditions. Radiometers can be snowcovered, precipitation gauges undercatch rain and especially snowfall and the anemometers show problems at low wind speeds. The forcing data with the highest uncertainty are those, where no direct measurement was available: soil temperature readings could not be used due to the lack of snowcover. At the LES site neither shortwave radiation measurements, nor wind speed observation are available. The major source of uncertainty at this site results therefore from the estimation of those variables. As Mishra (2009) pointed out, the contribution of a model input uncertainty to the model output uncertainty is a function of both, the uncertainty in deriving this input parameter and the sensitivity of the output to this very input parameter.

Uncertainty of validation data Nine to 14 days lie between the pre-event snow surveys, which were used to set the initial conditions of the snowpack and the post-event surveys, which were used for model validation purposes. The time periods of interest, the ROS events, are just a couple of hours to a couple of days in duration. This difference of observation and model time scale is the main flaw of using the surveys for validation. Therefore not just processes during the ROS event itself, but during the whole period are integrated. Processes like snow accumulation, snow redistribution and radiation driven melt take place. All those processes influence the result and add to the uncertainty. To conclude a model performance during the ROS events from the difference of snowdepth and SWE to the post-event snow survey is therefore problematic. Furthermore, the measurement technique of manual snow surveys itself might be subject to uncertainty, resulting from the use of different measurement devices for deep and shallow snowpacks (Mount Rose and ESC30 snow tube), changing survey operators and the use of different sampling points.

When available, the sonic ranger snowdepth is the only validation possibility during the events. As it lies in the nature of a point measurement which is used to represent a spatial variable parameter, these measurements imply an element of uncertainty. This uncertainty increases with increasing spatial variability. Snow ablation processes were found to be less spatial variable than accumulation and redistribution processes (Egli et al., 2012). The sonic ranger measurements during the events are therefore assumed to be more suitable for validation during the ROS periods, rather than during pre- and post-event periods. The meltwater production and therefore the SWE development is of major interest in this study. However, the SR50 sonic ranger measures snowdepth, which adds the uncertainty of the snowpack density estimation procedure. For validation purposes at a point scale, the snow pillow at the LES has many advantages compared to the above described a snowdepth measurement. However, this measurement technique has shown unexpected and unexplainable behavior after the May 2013 event. This is raising questions about the reliability of this device as well. Bridging effects of hard snow layers and the drainage of wet snow can influence snow pillow readings (Pomeroy and Gray, 1995).

Model uncertainty In addition to the uncertainties origin from the forcing and validation data, the model structure and parametrization add to the model uncertainty as well. Hereafter, the uncertainties and issues of estimating the different energy fluxes are discussed.

As tested at the UC, UF and UTow site, the longwave approximation following Sicart et al. (2006) shows an overestimation of $Q_{lw\downarrow}$ (see fig. 35 and 36) during cloudy conditions and during the nighttime for clear sky conditions. Especially during nights with potentially negative net longwave radiation values, this overestimation of $Q_{lw\downarrow}$ influences the EB, by potentially preventing the snowpack to cool off. The incoming longwave approximation was improved by bypassing the corresponding routine with the build in macro interface. Thereby the sky emissivity was set to a constant value of 0.98 (fig. 37 and 38) during the events itself where full cloud cover can be assumed. The model performance improved in the gap from a RMSE of 23.6 to 4.4 W/m^2 and in the open from 23 to 6.5 W/m^2. In the forest the use of the macro decreases the performance slightly from a RMSE of 4.4 to 8.2 W/m^2 respectively. The model by Sicart et al. (2006), however, is the best one available for the non-event days and was therefore further employed.

The employed albedo routine uses a function, where the albedo decay due to aging and due to melting is differentiated (Verseghy, 1991). There is no direct way to parametrize this routine to account for possible dust and debris precipitated on leeward slopes or falling litter under canopy. The albedo variability in partly forested basins is considerable but difficult to monitor (Mazurkiewicz et al., 2008). ROS events with heavy rainfall and high wind speeds might enhance the litter fall and alter the albedo additionally.

As the calculation of the turbulent fluxes are based on the Obukhov and Monin similarity theory, the limitations of the theory have to be addressed. The theory is limited to the constant-flux layer above the roughness sublayer over homogenous surfaces. Helgason and Pomeroy (2005) state, that the underlying assumption of this flux-profile approach of a steady state and constant vertical flux layer might be not valid in non-homogeneous terrain. Here, large horizontal turbulence adjust more slowly to changes in surface roughness than do smaller vertical eddies, and therefore show some of the upstream roughness characteristics. For vegetation $\geq 0.1\,\mathrm{m}$ the roughness sublayer becomes increasingly important. The constant-flux layer, where the similarity theory is valid, becomes very shallow for tall vegetation (Foken, 2006). Helgason and Pomeroy (2005) found high values for the roughness length z_0 using a Eddy-Covariance system, even at the comparatively homogeneous valley bottom at MCRB. This indicates that the flow was not in equilibrium with the snow surface. Therefore the turbulent fluxes are higher than they are when estimated from approaches based on Monin-Obukhov similarity theory and textbook values such as provided by Reba et al. (2012). Topographic features and wind flow patterns have therefore to be taken into account when selecting appropriate effective transfer coefficients (Helgason and Pomeroy, 2012). Even under ideal homogeneous conditions, the accuracy of the Obukhov theory was found to be about 10-20 % (Foken, 2006). However, Marks et al. (2008) found a very close match of modeled turbulent fluxes over a snowpack using the Obukhov-Monin theory and measured values from an Eddy-Covariance system in a mature pine stand.

Due to the lack of snowcover over the soil thermocouples during the events, the assumption of a soil temperature of 0 °C was made. Since the ground heat flux is calculated using a gradient approach, this cancels the ability of the ground heat flux to provide energy to an isothermal snowpack. Shallow snowpacks, where shortwave radiation penetrates the snowcover and warms the underlying soil can't therefore be represented. Marks et al. (1998) found Q_g contributions of 25 % to total melt energy for those conditions. For the ROS periods however, this assumption might be valid. Singh et al. (1997) found constant soil temperatures of 0 °C throughout their ROS experiments.

As the ROS events analysed in this study occurred late in the melt season, where the snowcover becomes increasingly patchy and the snowcovered area decreases, the neglect of lateral advection energy fluxes is questionable. To include this energy flux into melt calculations is an important consideration. Higher surface temperatures of snow free patches due to a lower surface albedo causes enhanced longwave emmission, sensible and latent heat transfer towards the snow patches (Granger et al., 2002). The model does not account for lateral energy transport from adjacent bare ground. However, during a ROS situation where the cloud cover prevents substantial solar heating of the bare ground, horizontal advection will be minimal.

The precipitation phase estimation procedure following Harder and Pomeroy (2013) was developed at the MCRB. The authors found good agreement of measured and predicted phase at an hourly time scale at the UC site and validated the model at the FR site. Thereby a good performance of the psychometric EB method (≈2 % rain error at hourly time scale) could be shown.

Due to model stability issues the maximum liquid water content $w_{c,max}$ had to be set to an unrealistic low value. Snobal was developed for the warm snowpacks in California, which seems to result in problems concerning the the removal of the cold content and the thereby refreezing water amount.

One main difficulty to model the snowpack development over multiple weeks, seems to be the redistribution of snow at the alpine sites. To neglect blowing snow processes during the ROS events might be a valid approach, due to wet high density snowpack conditions. The model results however suggest, that this approach fails for longer periods, even during the late melt season at the observed sites.

5.3.2 Suitability of the Model for Sensitivity Analysis

Due to the above mentioned uncertainties a validation of the model during the rain events is very difficult. The model showed an underestimation of the snowdepth decrease, found for the May and June 2013 event at the FR site (see fig. 12 and 15) and the underestimation of the SWE decline at the LES site (see fig. 13 and 16) compared to the point measurements of the sonic ranger and the snow pillow. These point measurements show the snowpack evolution during the ROS event but suffer from inadequate spatial representation.

The snow survey, however, are able to represent the snowcover on a HRU scale and are therefore more appropriate to represent the snowpack evolution. Furthermore, the model validation to SWE values reduces the model uncertainty. It eliminates the uncertainty of the density estimation procedure. The model predicts the post-event SWE found from the snow surveys well for the June 2011 and June 2013 event at the FR, FR_S and FR_SF site with errors $\leq 10\,\%$. As described in section 5.3.1 the results of the May 2013 post-event snow survey down the south side of the ridge are questionable. As a result the model is not able to predict those increasing values. With the forcing and validation data available and given the uncertainty that comes with it, the model performs reasonably well during ROS events. Due to its physically based nature, the model is assumed to be suitable for a sensitivity analysis during ROS conditions.

6 Sensitivity Analyisis

6.1 Results

6.1.1 Land use

Figure 18 shows the EB and its components for the pre-event and the event period for four land use classes. For the pre-event period (June 13^{th} to 16^{th}) the contribution of the energy fluxes to the total energy available for melt are found to be in the order of $Q_{snet}>Q_{lnet}>Q_h>Q_e>Q_g>Q_a$ for the land use classes b) to d). In the dense forest (a)) however, net longwave radiation provides the major source of energy. The canopy absorbs incoming shortwave radiation and wars, which results in the emission of thermal radiation.

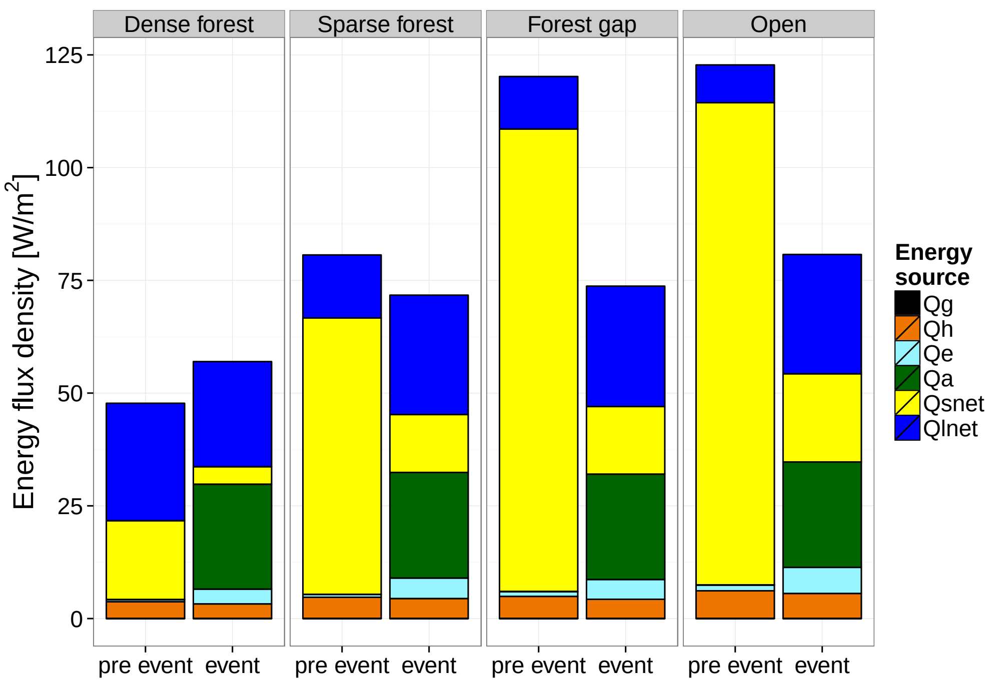

Figure 18: Modeled EB components of the June 2013 event and pre-event period, for four different land use classes.

Compared to this clear sky period, the model predicts a drastically different EB composition during the ROS-event (June 19^{th} to 21^{st}). The melt energetics are mainly influenced by longwave radiation advected heat flux. The influence of the shortwave radiation decreases remarkably. The latent heat flux increases, while the sensible heat flux shows no significant difference between pre-event and event period. The turbulent fluxes accounting together for about 10 % of the EB. During the event the fluxes contribute to the EB in the order of $Q_a > Q_{lnet} > Q_{snet} > Q_h \approx Q_e > Q_g$. There is more energy available for melt in the open, the gap and the sparse forest during the pre-event period than during the ROS event. Here, the additional energy input of advected heat from the rain, the increase of Q_{lnet} and the rise of Q_e could not compensate for the massive reduction of Q_{snet}. In the dense forest, however, where the absolute reduction of incoming shortwave radiation between pre-event and event is smaller, the total energy available for melt is higher during the event. It can be seen, that the degree of forest cover has a greater influence on the total energy flux during the pre-event condition than it has during the rain event.

Figure 19 shows the total energy available for melt under a 20 m tall forest stand with varying leaf area index. The graph illustrates the differences for pre-event and event conditions. To drive this comparison the forcing data from UF was used. It can be seen, that for both, the pre-event and the ROS period, an increase in LAI results in a reduced melt energy.

According to the model results this reduction is much steeper during the clear sky pre-event period than during the event. For sparse forest up to a LAI of 1.5 the meteorological conditions of the pre-event period result in a higher melt energy than the event conditions and for denser vegetation vice versa. The LAI can just be seen as a proxy of landuse, since other vegetation parameters like stand height, maximum interception load and canopy enhancement factor stayed constant for the analysis. This simple analysis also does not account for the dependency of wind speed and roughness length to vegetation density. The resulting change in the turbulent fluxes are therefore neglected. Nonetheless, the general pattern of melt energy for sparse and dense vegetation cover, found from the defined land use classes (fig. 18) could be shown here, too.

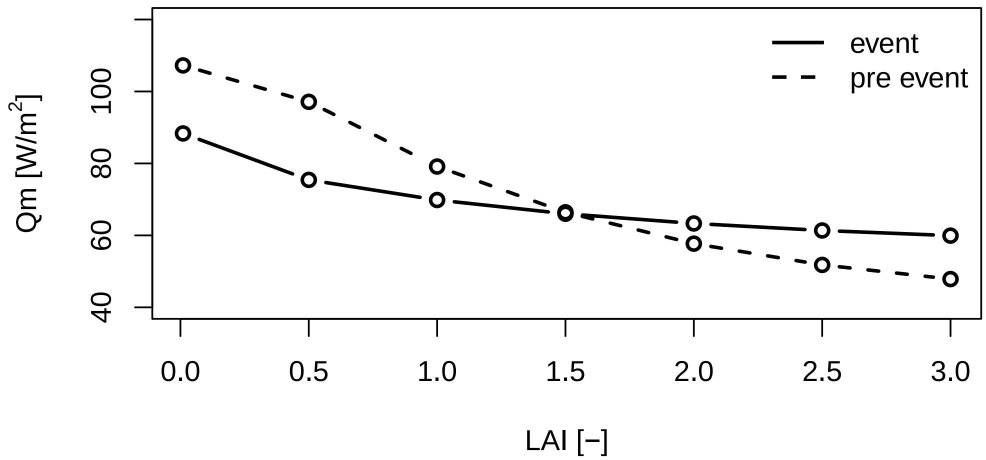

Figure 19: Total energy available for melt during ROS event and pre-event for varying LAI.

6.1.2 Initial Snowpack Condition

Figure 20 shows the change in the EB components (bars) and the resulting energy available for melt (line) due to a change of the initial snowpack temperatures in the open land form. The energy flux that is necessary to raise the internal snowpack temperature to isothermal 0°C is indicated as Q_{cc}. As expected, it can be seen, that the melt energy decreases with colder initial snowpack conditions. The ground heat flux increases slightly during the ROS period, due to higher temperature gradients between the lower snow layer and the underlying soil at the beginning of the simulation. A reduction of initial mean snowpack temperature to -7.2 °C reduces the energy available for melt by 42 %.

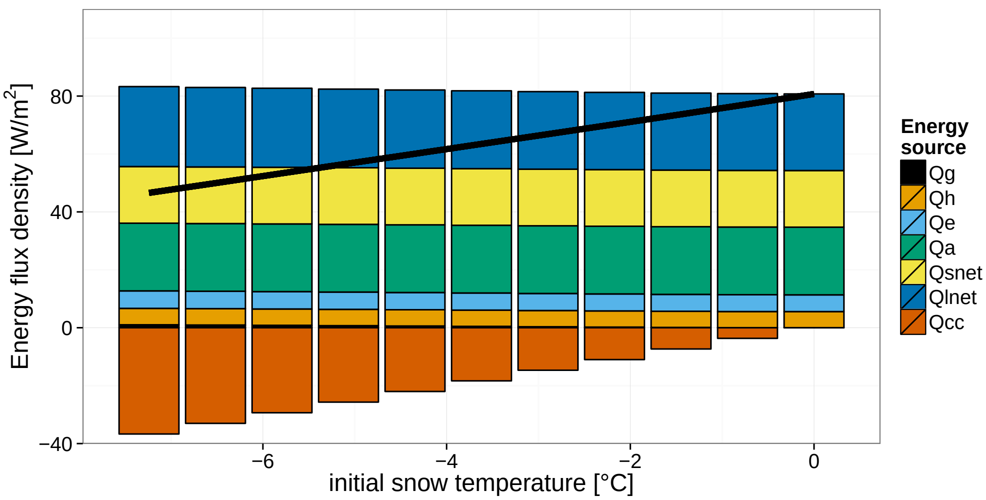

Figure 20: Change of EB components for different initial snowpack temperatures (bars) and the resulting energy available for melt (black line) in the open landform.

6.1.3 Slope and Aspect

Figure 21 and 22 show the influence of aspect and slope on the meltwater production during both, the ROS period and the pre-event period. The results show that the aspect plays a much greater role for the snowmelt in the clear sky period rather than during the ROS event. The difference between the land use scenarios is much greater during non-ROS event conditions. The maximum of the cumulative melt is neither in the pre-event period, nor in the ROS period at a south facing slope at 180 °. During the ROS event the maximum is shifted towards the west, which can be explained with an average minimum of cloud cover in the afternoon during the event days. The shift towards the east during the clear sky pre-event period is due to the topography of the valley and the shading of the surrounding mountains. The results show that the influence of aspect and slope on snowmelt is rather small. First, this can be explained by the decreased contribution of net shortwave radiation to the EB and second, by the increase in the diffuse fraction of the incoming shortwave radiation.

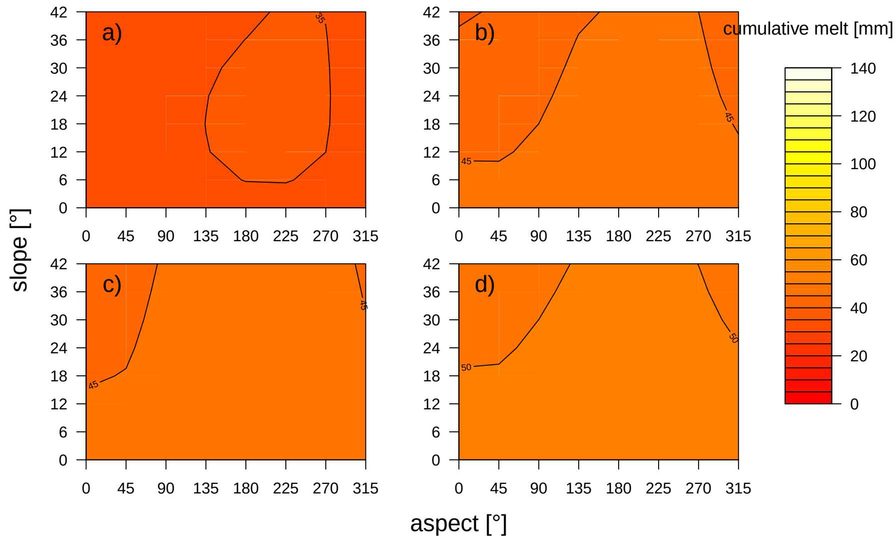

Figure 21: Response surface of cumulative melt to aspect and slope for a three day ROS-period for four land use classes (a) dense forest, b) sparse forest, c) forest gap and d) open).

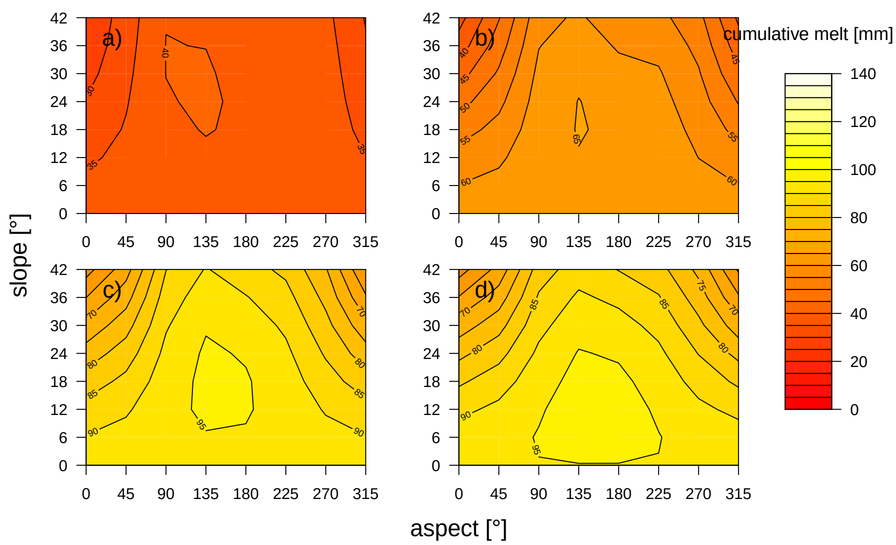

Figure 22: Response surface of cumulative melt to aspect and slope for a three day clear sky period prior to ROS-event for four land use classes (a) dense forest, b) sparse forest, c) forest gap and d) open).

6.1.4 Temperature and Precipitation

The response of the modeled snowpack EB to a change in air temperature is shown in figure 23. All fluxes show a positive correlation to a change in air temperature. According to the model, the net longwave radiation is the most sensitive energy flux to a change in air temperature. The energy advected from rain shows also a pronounced response. The turbulent fluxes respond approximately equally to an air temperature change. However, the sensitivity of the latent heat flux is slightly higher than the sensible heat flux. Due to the albedo feedback of the increasing fraction of solid precipitation, even the Q_{snet} flux declines with colder conditions. This is more apparent in the open than in the forest, because of the interception of the falling snow fraction and a higher required snowfall amount to refresh the albedo in the forest. For warmer temperatures, however, where no snowfall is predicted, Q_{snet} is insensitive to a change in air temperature. This is expected since the albedo routine differentiates between albedo decay due to melt and due to metamorphism, but is independent of the melt rate.

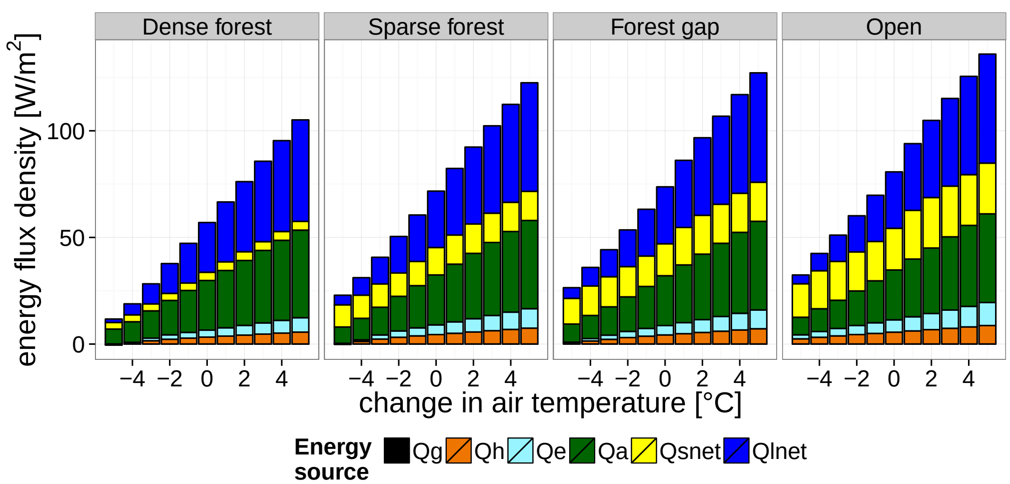

Figure 23: Response of the energy fluxes to a change in air temperature for four land use classes.

The influence of the precipitation amount that falls on a snowpack on the EB is illustrated in figure 24.

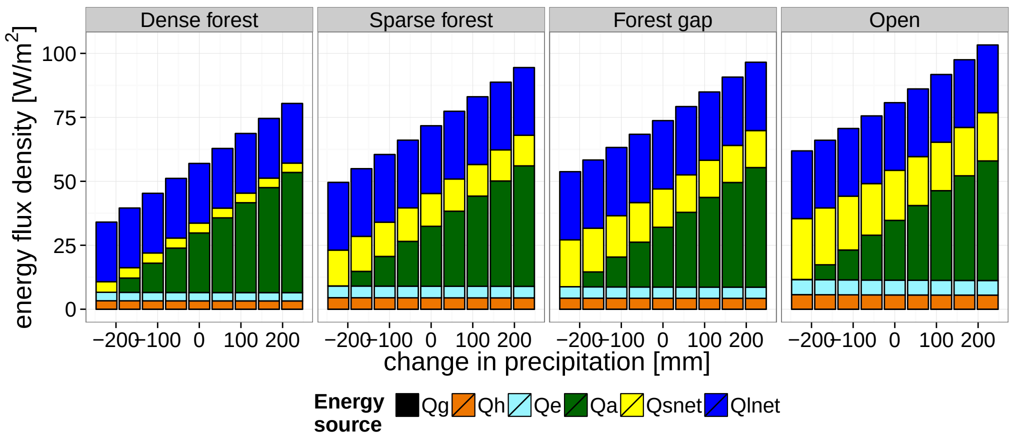

Figure 24: Response of the energy fluxes to a change in precipitation amount for four land use classes.

It can be seen that the advected energy flux is by far the most responsive EB component. An increase of 100 mm precipitation results in an additional 11 W/m^2 of advected energy. At the observed temperature the albedo feedback on the sensitivity of Q$_{snet}$ is here also apparent. With a decrease in precipitation, the snowfall decreases, the albedo stays lower and the net shortwave radiation flux increases. As previously mentioned, this is not the case for runs with higher air temperatures.

Air temperature has a substantial impact on the ROS EB. Figure 25 shows the dependency of the advected energy flux on air temperature and precipitation amount. Throughout the land use classes, a strong positive correlation of the advected heat flux to both parameter is apparent. Minimal differences of Q$_a$ response were found between the land use classes.

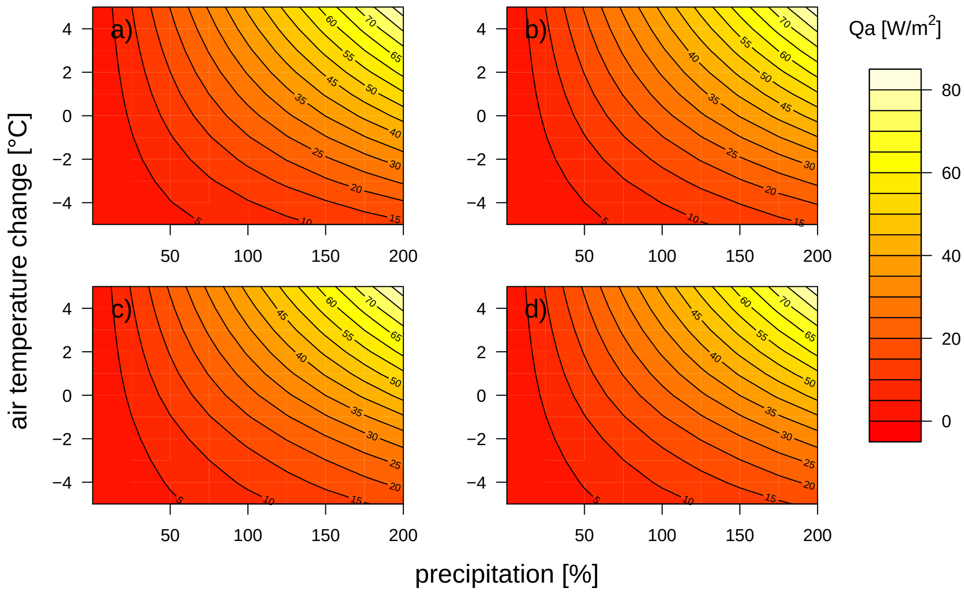

Figure 25: Response surface of the advective heat flux Q_a to air temperature and precipitation for a three day ROS-period for four land use classes (a) dense forest, b) sparse forest, c) forest gap and d) open).

As shown in figure 26, the influence of T$_a$ on the snowmelt is greater than the influence by the precipitation. This is expected, since the precipitation amount controls mainly the advective flux and the air temperature has a strong influence on most EB components. However, for low air temperatures, where the fraction of solid precipitation increases, it can bee seen that the melt increases when no precipitation is added to the snowpack. This bend in the contour lines between 0 % and 25 % of the measured precipitation is reduced in the gap and not present under the canopy. At the end of the event a small fraction of the falling precipitation becomes snow for lower air temperatures. Interception decreases the snowfall in land use class a) and b) and alters therefore the refreshing of the snow albedo and the above described albedo feedback (fig. 23).

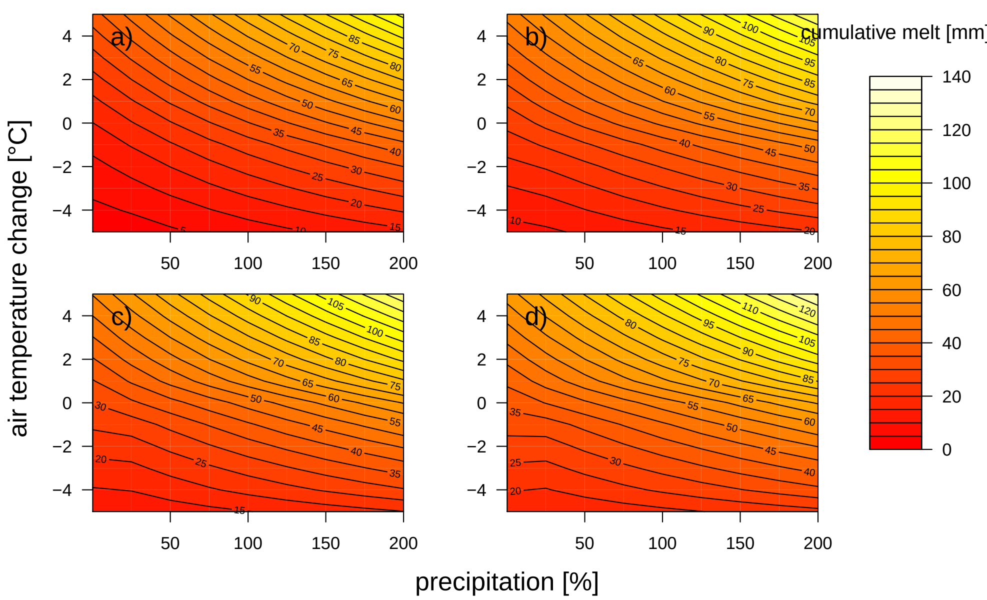

Figure 26: Response surface of cumulative melt to air temperature and precipitation for a three day ROS-period for four land use classes (a) dense forest, b) sparse forest, c) forest gap and d) open) for an isothermal snowpack.

Figure 27 illustrates the snowmelt response to a change in air temperature and precipitation amount for an initially cold snowpack (-7.2°C). The initial cold content could be sustained well into the event period, resulting in a different melt response to parameter changes compared to isothermal conditions. Overall reduced cumulative melt values are apparent. Furthermore, it can be seen that there is a greater difference in cumulative melt between 0 and 25 % of precipitation compared to higher precipitation amounts, especially for low air temperatures. Lower air temperatures result in a greater cold content at the onset of the rain. If liquid water is added to the snowpack, this percolating rainwater releases latent heat due to refreezing. This removes the cold content efficiently and allows the snowpack to melt with further energy input.

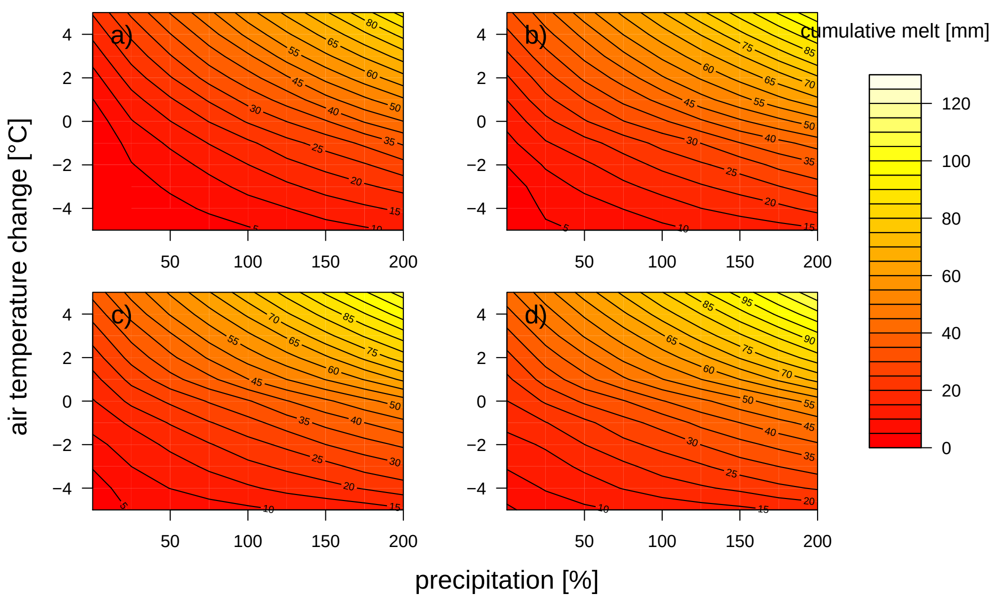

Figure 27: Response surface of cumulative melt to air temperature and precipitation for a three day ROS-period for four land use classes (a) dense forest, b) sparse forest, c) forest gap and d) open) for an initially cold snowpack.

6.1.5 Temperature and Wind Speed

Figure 28 illustrates the EB response to a change in wind speed. The same relative change in wind speed results in different absolute changes for the land use classes. However, bigger storms will not result in the same absolute wind speed change under the canopy and the open. The turbulent fluxes of latent and sensible heat are the only energy fluxes that are sensitive to both parameters. Because of the difference of absolute wind speed changes the response of the turbulent fluxes is altered in the dense forest compared to their response in the open. Hence, bigger storms, which come with increasing wind speeds, result in a greater differences in available melt energy between the land use classes. A doubling in wind speed increases the contribution of the turbulent fluxes to the total EB to 6.2 % in the forest and to 32 % in the open.

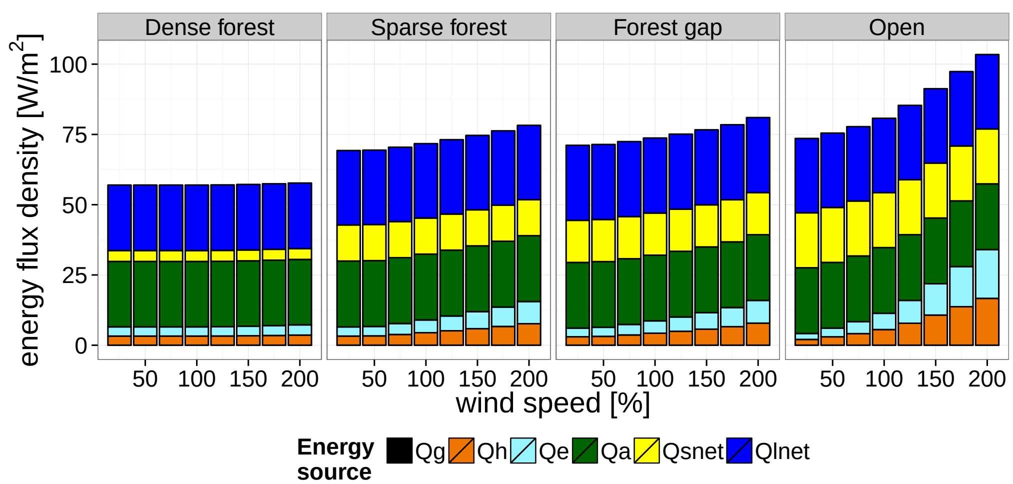

Figure 28: Response of cumulative melt to wind speed for a three day ROS-period for four land use classes.

The combined influence of wind speed and air temperature on meltwater production can be seen in figure 29. The graph shows cumulative melt relative to unchanged conditions (ΔT_a=0 u=100 %). While the cumulative melt shows almost no response to changing wind speeds in the dense forest, meltwater production differs at the other land use classes when the model is forced with 50 % and 150 % of the measured wind speed. The influence of the wind speed increases with increasing air temperature. However, the influence of the wind speed on cumulative melt seems rather small compared to the influence of the air temperature.

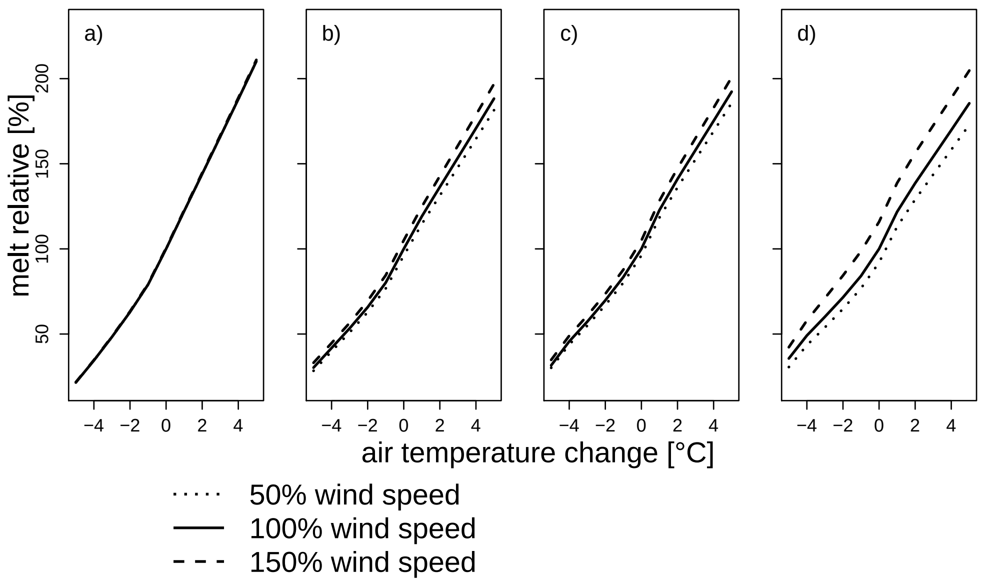

Figure 29: Response of cumulative melt to air temperature and wind speed for a three day ROS period for four land use classes (a) dense forest, b) sparse forest, c) forest gap and d) open). Values are relative to the cumulativ melt for unchanged conditions ($T_a = \Delta 0°\mathrm{C}$ and u=100%)

The turbulent fluxes of sensible and latent heat (fig. 30 and 31) show the most distinct response to a changing wind speed and air temperature. The sensible heat fluxes increases with a doubling of the observed wind speed 3-fold from 5.5 W/m^2 to 16 W/m^2 in the open, in the dense forest, however, just from 3.2,W/m^2 to 3.6 W/m^2 (12.5 %). The latent heat flux increases from 5.6 W/m^2 to 16 W/m^2 in the open and from 3.3 W/m^2 to 3.7 W/m^2 in the dense forest and shows therefore about the same response than the sensible heat to a doubling of the wind speed. A one degree rise of the air temperature leads to an 0.47 W/m^2 increase in sensible heat in the forest and about 0.7 W/m^2 in the open. The latent heat flux responds with an increase of 0.67 W/m^2 in the forest and 0.97 W/m^2 in the open respectively. It can be seen that the wind speed itself affects the response of the turbulent fluxes to the air temperature and vice versa. The sensitivity of the turbulent fluxes to air temperature is altered in the forest, where wind speeds are reduced compared to the open. At the other hand the sensitivity of melt to wind speed increases with increasing air temperature.

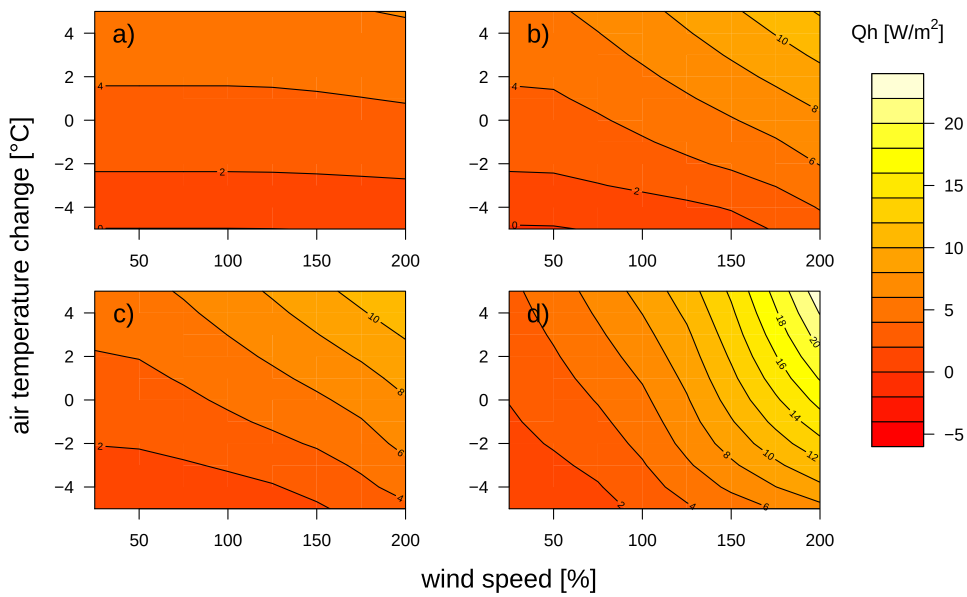

Figure 30: Response surface of the sensible heat flux Q_h to air temperature and wind speed for a three day ROS-period for four land use classes (a) dense forest, b) sparse forest, c) forest gap and d) open).

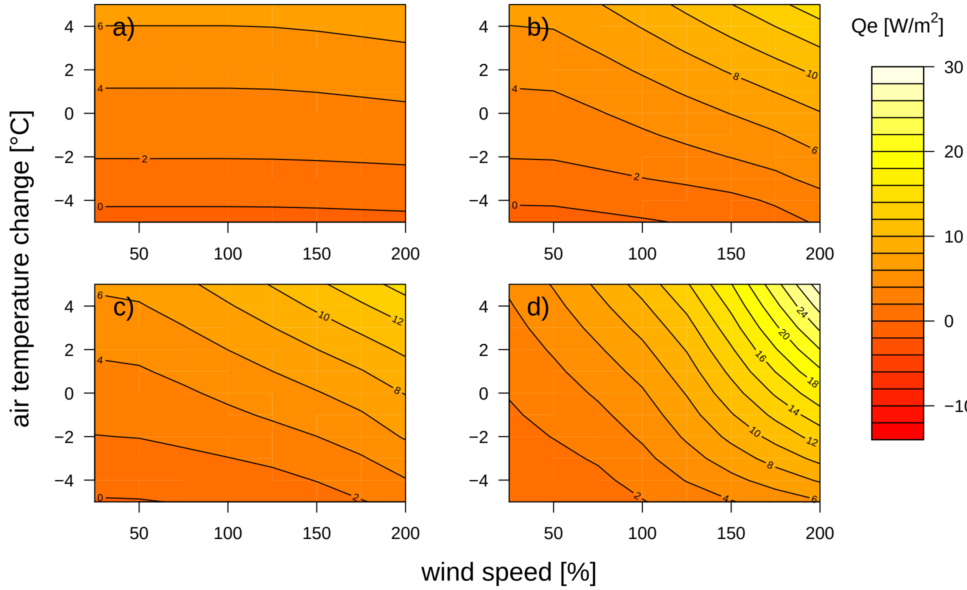

Figure 31: Response surface of the latent heat flux Q_h to air temperature and wind speed for a three day ROS-period for four land use classes (a) dense forest, b) sparse forest, c) forest gap and d) open).

6.1.6 Summary

The sensitivity of an energy flux or of the cumulative melt to a change of one ore more parameters is calculated according to section 4.7. As earlier defined, the sensitivity is provided as the slope of a linear regression between the varying parameter (e.g. air temperature) and the result variable (e.g cumulative melt). It is therefore a change of the response variable over a change of the parameter. To asses the impact of these correlations and in order to be able to compare the influence of each parameter, the sensitivity is multiplied by possible parameter ranges.

As Mishra (2009) noted, the usage of sensitivity coefficients outside a local parameter range just valid if the the functional relationship between parameter and response variable is linear over the entire range of parameters values. The model response to single parameter changes was found to be linear for T_a changes $\geq$-5°C.

1^{st} order sensitivity The sensitivity of the cumulative melt to single parameter changes is listed in table 6.

Table 6: 1^{st} order sensitivity of cumulative snowmelt and impact for realistic parameter ranges (bold). Parameter ranges include a 10 °C range in air temperature, 300 % range of wind speed, 350 mm range of precipitation, 180 ° range of northing and easting and a LAI range of 3.5 $\frac{m^2}{m^2}$.

parameter	unit	Dense forest	Sparse forest	Gap	Open
Ta	mm/°C	6.6	7.3	7.5	7.7
	mm	**66**	**73**	**75**	**77**
u	mm/%	0.003	0.042	0.045	0.137
	mm	**0.9**	**12.6**	**13.5**	**41.1**
P	mm/mm	0.088	0.085	0.079	0.076
	mm	**30.8**	**29.8**	**27.7**	**26.6**
northing	mm/° to N	-0.007	-0.013	-0.014	-0.016
	mm	**-1.3**	**-2.3**	**-2.5**	**-2.9**
easting	mm/° to E	-0.003	-0.003	-0.005	-0.004
	mm	**-0.5**	**-0.5**	**-0.9**	**-0.7**
LAI	mm/$\frac{m^2}{m^2}$	-6.8			
	mm	**-23.8**			

A change in air temperature has a strong influence on the meltwater production. For the observed meteorological conditions, a change in 10 °C, respectively the difference between a cold and a warm ROS event, influences the total cumulative melt by 66-77 mm. It can be seen that the positive correlation between air temperature and melt is the strongest in the open. The turbulent fluxes, however, show a peak sensitivity to T_a in the sparse forest (Q_h: 0.69 W/m^2 °C and Q_e: 0.90 W/m^2 °C). Here, the higher turbulence, specified through the roughness length, can compensate the reduction in wind speed compared to the open. This leads to a higher dependency of the turbulent fluxes on air temperature in the sparse forest.

The wind speed contributes in average about 0.003 mm per % increase of wind speed to the snowmelt in the dense forest and 0.14 mm in the open. This results in a marginal melt difference of 0.9 mm in the forest and a pronounced difference of 41 mm in the open for reasonable wind speed ranges

(0-300 % of observed values). Wind speed is the parameter with the second biggest impact on melt rates in the open.

The effect of changing precipitation amount on melt rates increases with increasing canopy coverage. Difference between the vegetation classes are result of three processes. i) different measured air temperatures for land use class dense forest/sparse forest and gap/open, which reduces the calculated temperature of the falling hydrometer; ii) rainfall interception reduces the rainfall amount slightly; iii) interception of the small fraction of solid precipitation in the later part of the event, as well as the higher accumulation threshold in the forest permits the albedo to refresh. The latter effect seems to be the strongest. A comparison of the sensitivity using warmer air temperatures, where the maximum fraction of solid precipitation is smaller than 1 %, reveals just minimal differences between the land use classes. For initially cold snowpack conditions (mean temperature -7.2°C) the model predicts a higher sensitivity of melt to precipitation. For lower precipitation amounts (0 to 25 to 50 %) the sensitivity of melt increases in the forest by 58 % and in the open by 35 % compared to the sensitivity found at isothermal conditions. This indicates that the presence of liquid water is crucial to bring a sub-freezing snowpack to melting conditions.

The aspect of a 30 ° slope, here expressed as northing and easting, has just a small influence on the cumulative melt. The sensitivity rises with decreasing canopy cover, however, the maximal impact on cumulative melt is only 1.8-3.6 mm. The sensitivity of the cumulative melt to the LAI seems rather high, but compared with pre-event conditions (-15.9 mm/$\frac{m^2}{m^2}$) it is obvious, that the influence of the vegetation cover is altered during the event.

2^{nd} order sensitivity The interaction between two parameters is analyzed as the ability of one parameter to change another parameters influence on the response variable. It can be expressed as the maximal potential change of the sensitivity. This is done by calculating the change of the sensitivity over the change of the parameter (see section 4.7). Table 7 provides these changes in the slope of the correlations to cumulative melt and the resulting impact on cumulative melt.

Table 7: 2^{nd} order sensitivity of cumulative snowmelt and impact for realistic parameter ranges (bolt).

impact of	on	unit	D. forest	S. forest	Gap	Open
u	Ta	mm/°C	0.23	1.26	1.22	5.84
		mm	**2.3**	**12.6**	**12.2**	**58.4**
P	Ta	mm/°C	4.47	4.44	4.56	4.58
		mm	**44.7**	**44.4**	**45.6**	**45.8**
Ta	u	mm/%	0.002	0.027	0.027	0.049
		mm	**0.58**	**8.1**	**8.0**	**14.7**
Ta	P	mm/mm	0.13	0.13	0.13	0.13
		mm	**44.3**	**43.8**	**46.2**	**46.8**

The sensitivity of melt to air temperature is also influenced itself by changes in precipitation and windspeed, through the mechanisms described in section 6.1.4 and 6.1.5.

The influence of the wind speed on the melt-air temperature correlation, respectively the maximal sensitivity of melt to air temperature resulting from this interaction, ranges from 0.23 mm/°C in the forest to 5.84 mm/°C in the open respectively. Given the range of air temperature values this results in a difference of 2-58 mm of melt between the coldest and the warmest events. The influence of the wind speed on the melt-T_a sensitivity is not linear. Therefore a second order polynomial regression was chosen to calculate the impact of wind speed on this sensitivity. The precipitation amount also influences the sensitivity of melt to air temperature, however, in a linear way. The sensitivity of melt to air temperature resulting from a maximal variation of precipitation is between 4.47 and 4.58 and therefore very similar throughout the land use classes. The total impact on cumulative melt was found to be up to 45.8 mm. Vice versa, the air temperature influences the sensitivity of melt to wind speed and precipitation. This interaction with the wind speed is rather small. It results a 15 mm melt difference in the open and a difference of 0.6 mm in the forest between cold events with low wind speeds and warm stormy events. For the precipitation, however, up to 46.8 mm of melt can origin from this interaction with air temperature.

Figure 32 illustrates the interaction of meteorological effects on the snowpack EB for eight discrete ROS scenarios. It is apparent that the change in snowcover energy is much higher for warm events than for cold events. Even for reduced precipitation and wind speed values there is more energy available in the forest for warm events, than in the open for cold events with high precipitation and wind speed values. The dependency of the turbulent flux on the wind speed and temperature is apparent, as well as the dependency of the advective heat flux on air temperature and precipitation amount. A doubling in wind speed and reduction of the rainfall amount to 25 % results in a relative contribution of the turbulent fluxes of 42 % in the open and 29 % in the forest for warm events. For cold events the relative contribution was found to be 38 % in the open and 15 % in the forest. This response of the turbulent fluxes has the biggest impact on the differences between the vegetation cover classes. The net longwave radiation is sensitive to the air temperature, but comprises a high fraction of the EB throughout the scenarios and is dominant whenever the precipitation and wind speed are low. If both, u and P are low, net longwave radiation contributes 56 % of melt energy in the open and 66 % in forest for warm conditions and 43 % to 59 % for cold conditions respectively. It is worth to note, that the energy provided by the net shortwave radiation might be small compared to that under clear sky conditions, but especially for colder events with lower wind speeds and moderate precipitation amounts it can still contribute up to 40 % to the energy available for melt in the open.

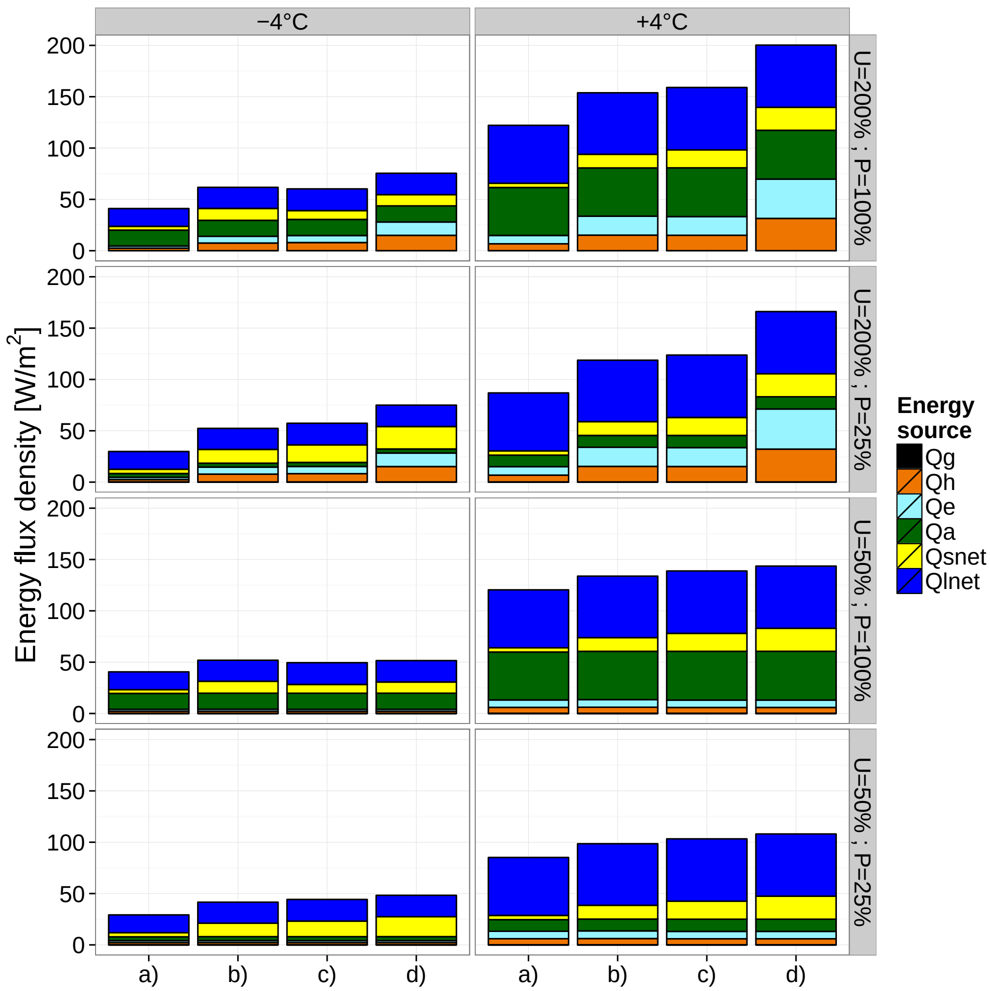

Figure 32: EB during ROS event for different combination of meteorological conditions in four land use classes (a) dense forest, b) sparse forest, c) forest gap and d) open). Variations of the wind speed u, the precipitation amount P and the air temperature ($\pm 4°C$) are indicated.

6.2 Discussion

6.2.1 Context to other Studies

As expected and as other studies have shown in the past, the influence of the shortwave radiation on the snowpack energy balance decreases during ROS events, whereas the contribution of longwave radiation and the turbulent fluxes of latent and sensible heat increase. However, in this study the energy provided from the turbulent sources account for only 9 % of the EB in the dense forest and 15 % in the open under the observed meteorological conditions. Garvelmann et al. (2014), found for two ROS events in a mid elevation mountain range in Germany contribution of the turbulent fluxes of 32-47 % under forest canopy and 67-72 % in the open. Marks et al. (1998) reported similar high contributions of 35 % in the forest and 75-80 % in the open for a big ROS event in the Central Oregon Cascades. For the same event Mazurkiewicz et al. (2008) found contributions of Q_h and Q_e of 25 % and 54 % at the H.J. Andrews Experimental Forest watershed in Western Oregon. Furthermore, the study by Mazurkiewicz et al. (2008) showed a relative contribution of the ground heat flux to the EB of between 8 to 23 %. However, the authors noted that there might be some bias from the soil temperature measurements, which led to an overestimation of Q_g. In the present study the ground heat flux was assumed to be restricted by a constant soil temperature of 0 °C. This study also shows that due to the intense cloud cover and the resulting high fraction of diffuse radiation, the effect of the aspect and slope on the shortwave radiation is minimized compared to that under clear sky conditions. This is in agreement with the findings of Garvelmann et al. (2014)who found no significant correlation of the aspect and the incoming shortwave radiation. The results from Garvelmann et al. (2014) showed a high contribution of Q_{lnet} to the change in snowcover energy in the forest (39 to 55 %), however a much lower, even negative contribution of -2 % in the open. Given the previously shown higher sensitivity of the longwave radiation to air temperature, compared to all other energy fluxes, the relative contribution of the Q_{lnet} decreases with decreasing T_a.

6.2.2 Spatial Variability during ROS

Berris and Harr (1987) and Marks et al. (1998) identified clear differences in melt rates between forested and open sites during ROS events. Garvelmann et al. (2014) however, found the energy available for snowmelt to be almost identical at open and forested locations. The results of this study agree more with the latter one. The model results suggest that the variability in melt energetics between land cover types are altered compared to non-ROS and particularly clear sky days. This results in a decreased spatial variability of potential meltwater production within a basin. Since the contribution of the shortwave radiation to the EB is limited during ROS conditions, the wind speed with its influence on the turbulent fluxes is the most important factor to cause differences in melt energetics between the land use classes. This is especially true for events with warm air temperatures. This implies that for events with low to moderate wind speeds, the spatial variability of the resulting melt will be muted.

An important consideration for the spatial distribution of potential melt rates during ROS events is the snowcovered area. If a storm occurs in midwinter or deposits fresh snow just before the actual rain event, the spatial differences in melt energetics might be relevant, given the spatial differences in wind speeds and cold content over a whole basin. However, for the events described in this study, which occurred late in the melt season, the remaining snowcover consisted mainly of wind slabs on leeward slopes and snow blown into the treeline - both locations are relatively sheltered from wind. There is therefore a bias due to snowcovered are depletion, which can potentially contribute to a ROS event and the site characteristics. Those locations are ofter open meadows forest gaps or sparse vegetated forests, where wind speeds are low. The spatial distribution of the rainfall determines to some extent the spatial variability of rain induced snowmelt rates. Rössler et al. (2014) found for a ROS event in the Swiss Alps, that the south facing slope received significant more precipitation than the north facing slope. This led to higher melt rates on the south side. The authors explained this local rainfall distribution with cavity circulation combined with a seeder-feeder-cloud system. A simple precipitation-elevation gradient is not a good proxi to asses the possible spatial variability of meltwater production in a catchment during ROS conditions.

The results of this study suggest, that during ROS conditions the variability between different aspects and forest coverages is altered compared to clear-sky days, where melt is mainly radiation induced. Especially when wind speeds are low, melt rates might be therefore very similar throughout the basin.

6.2.3 ROS Risk in the Eastern Canadian Rocky Mountains

The results show that snowmelt has only moderate sensitivity to rainfall amounts at low air temperatures. However, from the perspective of a flood risk assessment, precipitation is the most important factor. Mazurkiewicz et al. (2008) showed in their analysis of high frequency ROS events, that percolating rainfall was the major contributor of water available for runoff.

Valeo et al. (2007) analyzed air temperature and precipitation trends in the Elbow river watershed. The statistical analysis revealed significant temperature increases during February and March and no trend in annual precipitation amounts. However, they indicate an increase in precipitation in May. They state, that the snowpack in the upper watershed may be increasing, while it is decreasing in the lower elevations. Harder et al. (in press) found no increase in precipitation in the Kananaskis Valley. However, he identified an increase in annual minimum air temperatures, leading to a climate that is "less cold". McCabe et al. (2007) found in their analysis of ROS events in the Western United States a decrease in ROS frequency as air temperature increases. The authors tie this result to the effect of a decreasing length of time that snow is on the ground. This correlation was found to be most common for low-elevation sites. The authors suggest that the weaker trend in high elevations are due to the colder air temperatures. An increase in air temperature does not greatly decrease the number of snowfall days.

If the snowpack decreases in the lower elevations and melts out earlier, ROS events might be limited to a rather small spatial extent e.g. at the persistent deep snowdrifts. the period when a snowcover is present will shorten with the increase in low temperatures. The earlier melt out will decrease the likelihood of warm late spring rainfall to fall on a snowpack. This will decrease the ROS frequency. However, if heavy rain events occur earlier in the year rain induced melt events are possible in different circumstances.

Mid-winter and early spring ROS events could bring the rather cold Rocky Mountain snowpack into isothermal state and potentially generate meltwater over the whole extend of a basin.

6.2.4 Limitations of this Work

The sensitivity analysis is based on a real multiday ROS event. The averaging of the energy fluxes over the period does not show the temporal variability of the fluxes. For example for lower air temperatures, the change of snowcover energy becomes negative for short periods during the event. This information is lost when computing the mean flux. Also, the difference between night and daytime are averaged out. Furthermore, the period defined in the sensitivity analysis as a ROS event includes a period, where a small fraction of the precipitation falls as snow. Because the precipitation rate was found to be so high during the event, this small fraction of snow is enough to refresh the albedo. Therefore, the results are influenced by processes (e.g. albedo feedback) that would not be present during pure rain events. The assumption that a storm that doubles the wind speed in the open also doubles the wind speed in the forest is questionable. A possible solution could be to approximate the wind speed extinction coefficient (a in equation 7) by shortwave irradiance extinction Eagleson (2002). This would link the wind speed reduction under the canopy to the LAI. Following this approach, one could compute the absolute wind speed change for all land use classes.

7 Conclusion

Although uncertainties associated with observations and parameterizations exist, this study shows the ability of a physically based model to adequately reproduce the energy and mass balance of several rain-on-snow events in the Canadian Rockies. The definition of initial snowpack conditions prior to the events enables the model to run at point-scale on event-basis. Thousands of model runs were performed in order to asses the sensitivity of the energy fluxes and the resulting melt water production to topography, meteorological conditions and land cover changes. Overall, for different combination scenarios, radiation fluxes appeared to be the dominant source of energy available for melt. Especially during warm events with a dense cloud cover, net longwave radiation contributes substantial amounts of energy to snowmelt. The relative importance of the radiation terms for the ROS EB is particularly high, when wind speed and precipitation amounts are low. For events that come with high wind speeds the turbulent fluxes gain importance. High wind speeds combined with moderate precipitation amounts result in a high relative contribution of the turbulent fluxes to total energy available for melt of up to 42 % in the open and 29 % under forest canopy. Energy input from the rain can contribute significant amounts of energy to the snowpack in the form of adveced heat, especially if air temperatures are high. For initially cold snowpack conditions percolating and refreezing rainwater helps to overcome the cold content of the snowcover effectively through the release of latent heat. Snowmelt was found to be most sensitive to air temperature throughout all land use classes. The study shows the substantial impact of air temperature to net longwave radiation, advected heat and the turbulent fluxes of sensible and latent heat. A change in air temperature in the range of 10 °C results, for the conditions measured during the June 2013 event, in a melt difference of 66 mm in the forest and 77 mm in an open environment respectively. The impact of a change in wind speed of 300 % varies significantly between the land use classes examined. In the open the difference of high and low wind speeds results in up to 41 mm of melt, in the dense forest, however, it generates only 0.9 mm for unchanged air temperatures. The sensitivity of snowmelt to precipitation amount were found to be rather small. However, due to a wide range in possible rainfall intensities precipitation can generate up to 30.8 mm of melt for measured air temperatures. The sensitivity of melt rates to precipitation amount is highly dependent on air temperatures. The resulting change in melt-precipitation sensitivity to a change over the 10 °C air temperature range is 0.13 mm/mm. Over the range of possible precipitation amounts this interaction results in an additional 44 to 47 mm of melt. The feedback of a changing air temperature to the impact of the wind speed results in an additional melt of 0.6 mm in the forest and 15 mm in the open. Compared to a clear sky pre-event period, the control of aspect and forest cover on snowmelt was found to be muted during ROS conditions. For observed conditions a change in the aspect results in a maximal snowmelt difference of 3.6 mm in the open. The sensitivity of melt to a change in forest cover was found to be -6.0 mm of melt per $\frac{m^2}{m^2}$ change of LAI during the ROS event and -15 mm/$\frac{m^2}{m^2}$ during clear sky conditions. This implies that with spatial constant precipitation rates the spatial variation of potential melt energetics are altered during ROS events, especially if wind speeds are low. When snowpacks are further decreasing and colder than normal conditions become less likely, the ROS frequency will decline in the Canadian Rockies. However, if warm rainfall occur earlier in spring, ROS events can generate melt over the whole extent of a basin and potential contribute to flood events.

Bibliography

Al Nakshabandi, G. and Kohnke, H. (1965). Thermal conductivity and diffusivity of soils as related to moisture tension and other physical properties. *Agricultural Meteorology*, 2(4):271–279.

Anderton, S., White, S., and Alvera, B. (2002). Micro-scale spatial variability and the timing of snow melt runoff in a high mountain catchment. *Journal of Hydrology*, 268(1-4):158–176.

Beke, G. J. (1969). *Soils of three experimental waterscheds in Alberta and their hydrological significance.* PhD thesis, University of Alberta, Edmonton, Alberta.

Berg, N., Osthuber, R., and Bergamn, J. (1991). Rain-induced outflow from deep snowpacks in the central sierra nevada, california. *Hydrological Sciences Journal*, 36(6):611–629.

Berris, N. and Harr, D. (1987). Comparative snow accumulation and melt during rainfall in forested and clear-cut plots in the western cascades of oregon. *Water Resources Research*, 23(1):135–142.

Brutsaert, W. (1982). *Evaporation into the Atmosphere: Theory, History and Applications*, volume 1 of *Environmental Fluid Mechanics*. Springer Netherlands, Dordrecht.

Cionco, R. M. (1965). A mathematical model for air flow in a vegetative canopy. *Journal of Applied Meteorology*, (4):517.

Cionco, R. M. (1978). Analysis of canopy index values for variouse canopy densities. *Boundary-Layer Meteorology*, (15):81–93.

DeBeer, C. (2012). *Simulating Areal Snowcover Depletion and Snowmelt Runoff in Alpine Terrain.* PhD thesis, University of Saskatchewan, Saskatoon, SK.

DeWalle, D. R. and Rango, A. (2008). *Principles of snow hydrology.* Cambridge University Press, Cambridge, UK and New York.

Dingman, S. L. (2008, c2002). *Physical hydrology.* Waveland Press Inc, Long Grove, Ill., 2nd ed. edition.

Eagleson, P. S. (2002). *Ecohydrology: Darwinian expression of vegetation form and function*. Cambridge University Press, Cambridge, UK and New York.

Egli, L., Jonas, T., Grünewald, T., Schirmer, M., and Burlando, P. (2012). Dynamics of snow ablation in a small alpine catchment observed by repeated terrestrial laser scans. *Hydrological Processes*, 26(10):1574–1585.

Ellis, C. R., Pomeroy, J. W., Brown, T., and MacDonald, J. (2010). Simulation of snow accumulation and melt in needleleaf forest environments. *Hydrology and Earth System Sciences*, 14(6):925–940.

Essery, R. and Etchevers, P. (2004). Parameter sensitivity in simulations of snowmelt. *Journal of Geophysical Research*, 109(D20).

Fang, X., Pomeroy, J. W., Ellis, C. R., MacDonald, M. K., DeBeer, C. M., and Brown, T. (2013). Multi-variable evaluation of hydrological model predictions for a headwater basin in the canadian rocky mountains. *Hydrology and Earth System Sciences*, 17(4):1635–1659.

Foken, T. (2006). 50 years of the monin–obukhov similarity theory. *Boundary-Layer Meteorology*, 119(3):431–447.

Garnier, B. J. and Ohmura, A. (1970). The evaluation of surface variations in solar radiation income. *Solar Energy*, 13(1):21–34.

Garvelmann, J., Pohl, S., and Weiler, M. (2014). Variability of observed energy fluxes during rain-on-snow and clear sky snowmelt in a midlatitude mountain environment. *Journal of Hydrometeorology*, 15(3):1220–1237.

Golding, D. L. (1974). The correlation of snowpack with topography and snowmelt runoff on marmot creek basin, alberta. *Atmosphere*, 12(1):31–38.

Granger, R. J., Pomeroy, J. W., and Parviainen, J. (2002). Boundary-layer integration approach to advection of sensible heat to a patchy snow cover. *Hydrological Processes*, 16(18):3559–3569.

Gray, D. M. and Male, D. H. (2004). *Handbook of snow: Principles, processes,* ***management*** *& use*. Blackburn Press, Caldwell, N.J.

Harder, P. and Pomeroy, J. (2013). Estimating precipitation phase using a psychrometric energy balance method. *Hydrological Processes*, 27(13):1901–1914.

Harder, P., Pomeroy, J., and Westbrook, C. (in press). Hydrological resilience of a canadian rockies headwaters basin subject to changing climate, extreme weather and forest management. *Hydrological Processes*

Hardy, J. P., Davis, R. E., Jordan, R., Li, X., Woodcock, C., Ni, W., and McKenzie, J. C. (1997). Snow ablation modeling at the stand scale in a boreal jack pine forest. *Journal of Geophysical Research*, 102(D24):29397.

Harr, R. D. (1981). Some characteristics and consequences of snowmelt during rainfall in western oregon. *Journal of Hydrology*, 53(3-4):277–304.

Hedstrom, N. and Pomeroy, J. (1998). Measurements and modelling of snow interception in the boreal forest. *Hydrological Processes*, (12):1611–1625.

Helgason, W. and Pomeroy, J. (2012). Problems closing the energy balance over a homogeneous snow cover during midwinter. *Journal of Hydrometeorology*, 13(2):557–572.

Helgason, W. and Pomeroy, J. W. (2005). Uncertainties in estimating turbulent fluxes to melting snwo in a mountain clearing. *Eastern Snow Conference*, (62).

Jost, G., Weiler, M., Gluns, D. R., and Alila, Y. (2007). The influence of forest and topography on snow accumulation and melt at the watershed-scale. *Journal of Hydrology*, 347(1-2):101–115.

King, J., Pomeroy, J., Gray, D. M., Fierz, C., Föhn, P., Harding, R., Jordan, R., and Martin, E., Plüss, C (2008). Snow–atmosphere energy and mass balance. In Armstrong, R. and Brun, E., editors, *Snow and climate*, pages 70–124. Cambridge University Press, Cambridge.

Krogh, S. A., Pomeroy, J. W., and McPhee, J. (2015). Physically based mountain hydrological modeling using reanalysis data in patagonia. *Journal of Hydrometeorology*, 16(1):172–193.

List, R. J. (1968). *Smithsonian Meteorological Tables. 6th Edition,* Smithsonian Institution.

López-Moreno, J. I., Pomeroy, J. W., Revuelto, J., and Vicente-Serrano, S. M. (2013). Response of snow processes to climate change: spatial variability in a small basin in the spanish pyrenees. *Hydrological Processes*, 27(18):2637–2650.

Lu, H., Wei, W. S., Liu, M. Z., Han, X., and Hong, W. (2012). Changes in seasonal snow liquid water content during the snowmelt period in the western tianshan mountains, china. *The Cryosphere Discussions*, 6(5):4137–4169.

MacDonald, J. (2010). *Unloading of Intercepted Snow in conifer Forests*. PhD thesis, University of Saskatchewan, Saskatoon, SK.

Male, D. H. and Granger, R. J. (1981). Snow surface energy exchange. *Water Resources Research*, 17(3):609–627.

Marks, D. and Dozier, J. (1992). Climate and energy exchange at the snow surface in the alpine region of the sierra nevada: 2. snow cover energy balance. *Water Resources Research*, 28(11):3043–3054.

Marks, D., Kimball, J., Tingey, D., and Link, T. (1998). The sensitivity of snowmelt processes to climate conditions and forest cover during rain-on-snow: a case study of the 1996 pacific northwest flood. *Hydrological Processes*, 12(10-11):1569–1587.

Marks, D., Winstral, A., Flerchinger, G., Reba, M., Pomeroy, J., Link, T., and Elder, K. (2008). Comparing simulated and measured sensible and latent heat fluxes over snow under a pine canopy to improve an energy balance snowmelt model. *Journal of Hydrometeorology*, 9(6):1506–1522.

Mazurkiewicz, A. B., Callery, D. G., and McDonnell, J. J. (2008). Assessing the controls of the snow energy balance and water available for runoff in a rain-on-snow environment. *Journal of Hydrology*, 354(1-4):1–14.

McCabe, G. J., Hay, L. E., and Clark, M. P. (2007). Rain-on-snow events in the western united states. *Bulletin of the American Meteorological Society*, 88(3):319–328.

Melloh, R. A., Hardy, J. P., Bailey, R. N., and Hall, T. J. (2002). An efficient snow albedo model for the open and sub-canopy. *Hydrological Processes*, 16(18):3571–3584.

Mishra, S. (2009). Uncertainty and sensitvity analysis techniques for hydrologic modeling. *Journal of Hydroinformatics*, (11.3-4):282–296.

Musselman, K. N., Molotch, N. P., and Brooks, P. D. (2008). Effects of vegetation on snow accumulation and ablation in a mid-latitude sub-alpine forest. *Hydrological Processes*, 22(15):2767–2776.

Nogués-Bravo, D., Araújo, M. B., Errea, M. P., and Martínez-Rica, J. P. (2007). Exposure of global mountain systems to climate warming during the 21st century. *Global Environmental Change*, 17(3-4):420–428.

Parviainen, J. and Pomeroy, J. (2000). Multiple-scale modelling of forest snow sublimation: initial findings. *Hydrological Processes*, (14):2669–2681.

Pohl, S., Marsh, P., and Liston, G. E. (2006). Spatial-temporal variability in turbulent fluxes during spring snowmelt. *Arctic, Antarctic, and Alpine Research*, 38(1):136–146.

Pomeroy, J., Fang, X., and Marks, D. (2014). A cold rain-on-snow event in a canadian rockies alpine catchment: Characteristics and modelling.

Pomeroy, J., Stewart, R., and Whitfield, P. (Manuscript submitted for publication). The 2013 flood event in the bow and oldman river baisns; causes assessment, and damages. *Canadian Water Resources Journal*.

Pomeroy, J. W., Fang, X., and Ellis, C. (2012). Sensitivity of snowmelt hydrology in marmot creek, alberta, to forest cover disturbance. *Hydrological Processes*, 26(12):1891–1904.

Pomeroy, J. W. and Gray, D. M. (1995). *Snowcover accumulation, relocation, and management*, volume no. 5 of *National Hydrology Research Institute science report*. National Hydrology Research Institute, Saskatoon, Sask., Canada.

Pomeroy, J. W., Gray, D. M., Brown, T., Hedstrom, N. R., Quinton, W. L., Granger, R. J., and Carey, S. K. (2007). The cold regions hydrological model: a platform for basing process representation and model structure on physical evidence. *Hydrological Processes*, 21(19):2650–2667.

Pomeroy, J. W., Gray, D. M., Shook, K. R., Toth, B., Essery, R. L. H., Pietroniro, A., and Hedstrom, N. (1998a). An evaluation of snow accumulation and ablation processes for land surface modelling. *Hydrological Processes*, 12(15):2339–2367.

Pomeroy, J. W., Marks, D., Link, T., Ellis, C., Hardy, J., Rowlands, A., and Granger, R. (2009). The impact of coniferous forest temperature on incoming longwave radiation to melting snow. *Hydrological Processes*, 23(17):2513–2525.

Pomeroy, J. W., Parviainen, J., Hedstrom, N., and Gray, D. M. (1998b). Coupled modelling of forest snow interception and sublimation. *Hydrological Processes*, 12(15):2317–2337.

Pradhanang, S. M., Frei, A., Zion, M., Schneiderman, E. M., Steenhuis, T. S., and Pierson, D. (2013). Rain-on-snow runoff events in new york. *Hydrological Processes*, 27(21):3035–3049.

Rasouli, K., Pomeroy, J. W., Janowicz, J. R., Carey, S. K., and Williams, T. J. (2014). Hydrological sensitivity of a northern mountain basin to climate change. *Hydrological Processes*, 28(14):4191–4208.

Reba, M. L., Pomeroy, J., Marks, D., and Link, T. E. (2012). Estimating surface sublimation losses from snowpacks in a mountain catchment using eddy covariance and turbulent transfer calculations. *Hydrological Processes*, 26(24):3699–3711.

Rössler, O., Froidevaux, P., Börst, U., Rickli, R., Martius, O., and Weingartner, R. (2014). Retrospective analysis of a nonforecasted rain-on-snow flood in the alps – a matter of model limitations or unpredictable nature? *Hydrology and Earth System Sciences*, 18(6):2265–2285.

Rutter, A. J., Kershaw, K. A., Robins, P. C., and Morton, A. J. (1972). A predictive model of rainfall interception in forests, 1. derivation of the model from observations in a plantation of corsican pine. *Agricultural Meteorology*, 9:367–384.

Seneviratne, S. I., Corti, T., Davin, E. L., Hirschi, M., Jaeger, E. B., Lehner, I., Orlowsky, B., and Teuling, A. J. (2010). Investigating soil moisture–climate interactions in a changing climate: A review. *Earth-Science Reviews*, 99(3-4):125–161.

Sicart, J. E., Pomeroy, J. W., Essery, R. L. H., and Bewley, D. (2006). Incoming longwave radiation to melting snow: observations, sensitivity and estimation in northern environments. *Hydrological Processes*, 20(17):3697–3708.

Singh, P. and Kumar, N. (1997). Effect of orography on precipitation in the western himalayan region. *Journal of Hydrology*, 199(1-2):183–206.

Singh, P., Spitzbart, G., Hübl, H., and Weinmeister, H. (1997). Hydrological response of snowpack under rain-on-snow events: a field study. *Journal of Hydrology*, 202(1-4):1–20.

Solberg, E. J., Jordhøy, P., Strand, O., Aanes, R., Loison, A., Saether, B.-E., and Linnell, J. D. C. (2001). Effects of density-dependence and climate on the dynamics of a svalbard reindeer population. *Ecography*, 24(4):441–451.

Storck, P., Lettenmaier, D. P., and Bolton, S. M. (2002). Measurement of snow interception and canopy effects on snow accumulation and melt in a mountainous maritime climate, oregon, united states. *Water Resources Research*, 38(11):5–1–5–16.

Storr, D. (1967). Precipitation variations in a small forested watershed. *35th Annual Western Snow Conference*.

Strasser, U., Warscher, M., and Liston, G. E. (2011). Modeling snow–canopy processes on an idealized mountain. *Journal of Hydrometeorology*, 12(4):663–677.

Sui, J. and Koehler, G. (2001). Rain-on-snow induced flood events in southern germany. *Journal of Hydrology*, 252(1-4):205–220.

Valente, F., David, J. S., and Gash, J. (1997). Modelling interception loss for two sparse eucalypt and pine forests in central portugal using reformulated rutter and gash analytical models. *Journal of Hydrology*, 190(1-2):141–162.

Valeo, C., Xiang, Z., Bouchart, F.-C., Yeung, P., and Ryan, M. C. (2007). Climate change impacts in the elbow river watershed. *Canadian Water Resources Journal*, (37):285–302.

van Heeswijk, M., Kimball, J., and Marks, D. (1996). Simulation of water available for runoff in clearcut forest openings during rain-on-snow events in the western cascade range of oregon and washington. *Water-Resources Investigations Report*, 95(4219).

Varhola, A., Coops, N. C., Weiler, M., and Moore, R. D. (2010). Forest canopy effects on snow accumulation and ablation: An integrative review of empirical results. *Journal of Hydrology*, 392(3-4):219–233.

Verseghy, D. L. (1991). Class-a canadian land surface scheme for gcms. i. soil model. *International Journal of Climatology*, 11(2):111–133.

Winkler, R. D., Spittlehouse, D. L., and Golding, D. L. (2005). Measured differences in snow accumulation and melt among clearcut, juvenile, and mature forests in southern british columbia. *Hydrological Processes*, 19(1):51–62.

Wiscombe, W. J. and Warren, S. G. (1980). A model for the spectral albedo of snow. i: Pure snow. *J. Atmos. Sci.*, 37(12):2712–2733.

Ye, H., Yang, D., and Robinson, D. (2008). Winter rain on snow and its association with air temperature in northern eurasia. *Hydrological Processes*, 22(15):2728–2736.

Zhou, J., Pomeroy, J. W., Zhang, W., Cheng, G., Wang, G., and Chen, C. (2014). Simulating cold regions hydrological processes using a modular model in the west of china. *Journal of Hydrology*, 509:13–24.

Appendix A

Evaluation of the radiation modules

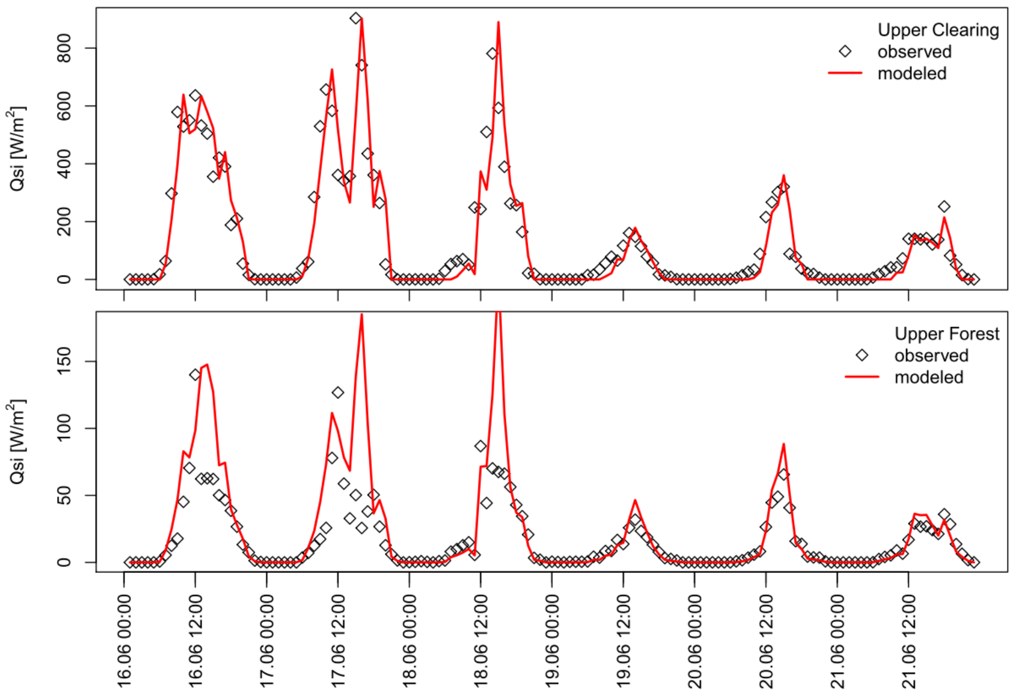

Figure 33: Timeseries of observed and modeled incoming shortwave radiation at UF and UC site for the June 2013 event.

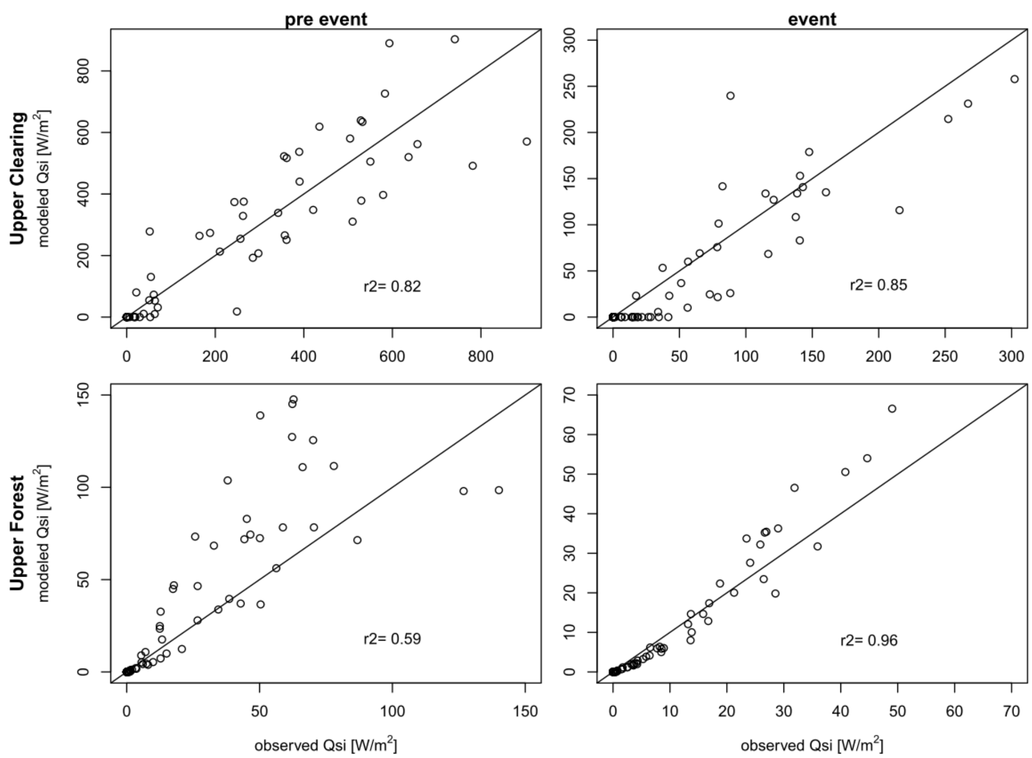

Figure 34: Observed and modeled incoming shortwave radiation at UF and UC site for the June 2013 event.

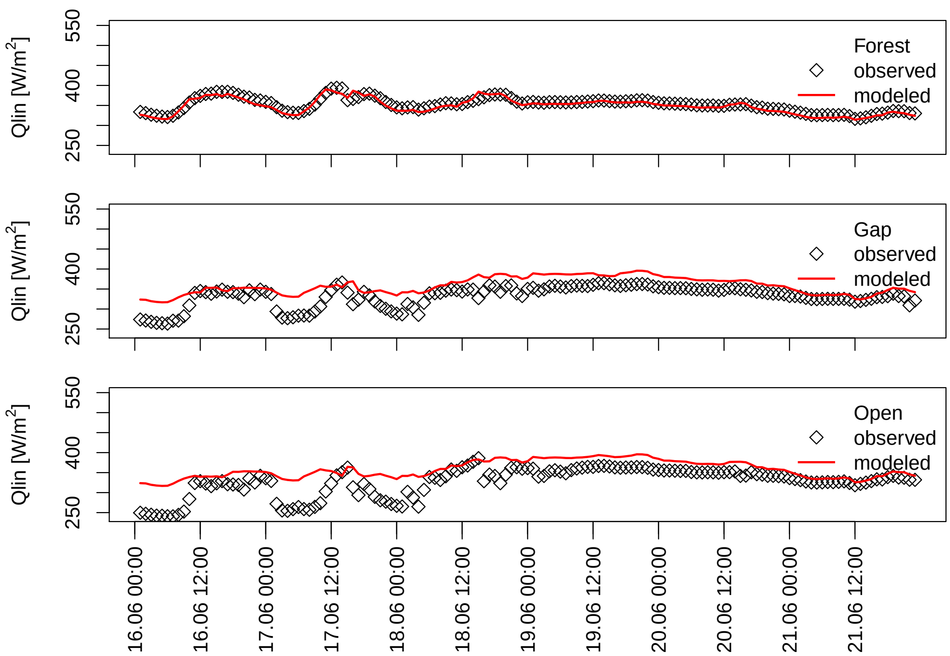

Figure 35: Observed and modeled incoming longwave radiation at UF UC and UTow site for the June 2013 event. Using a method proposed by Sicart et al., 2006.

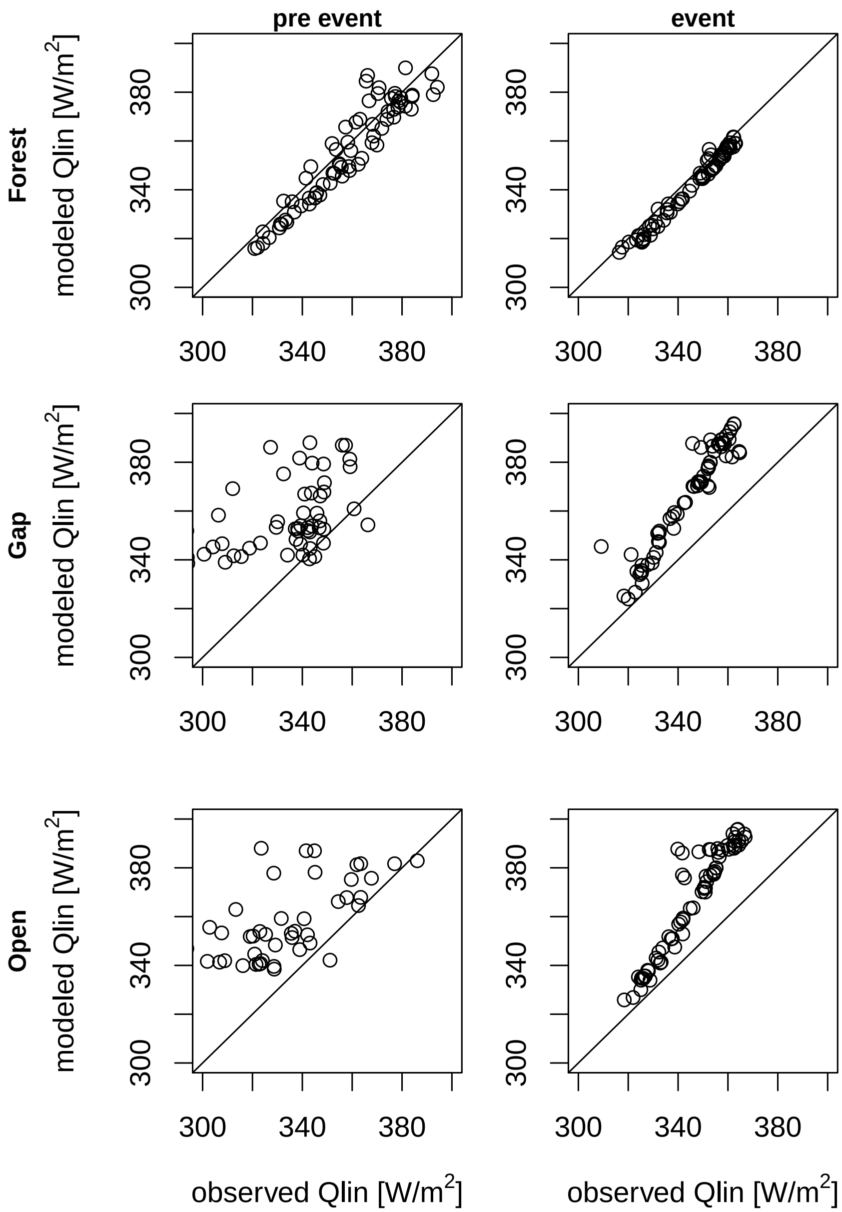

Figure 36: Performance of incoming longwave radiation computation at UF UC and UTow site for the June 2013 event. Using a method proposed by Sicart et al., 2006.

For the event period Sicarts Qli model is bypassed and the atmospheric emissivity is set to 0.98.

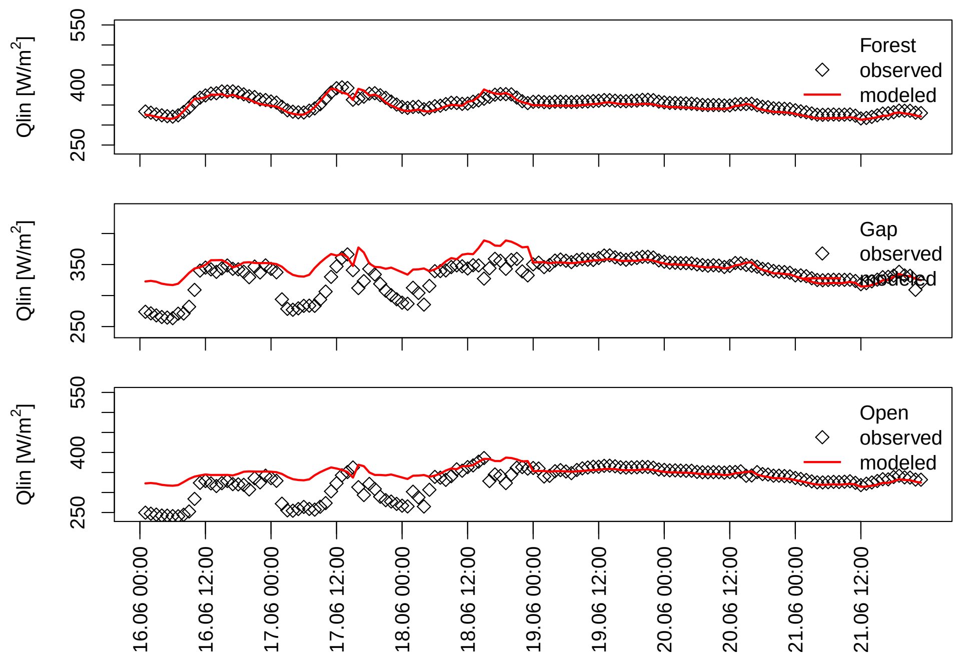

Figure 37: Observed and modeled incoming longwave radiation at UF UC and UTow site for the June 2013 event. Assuming atmospheric emissivity of 0.98 for the event period.

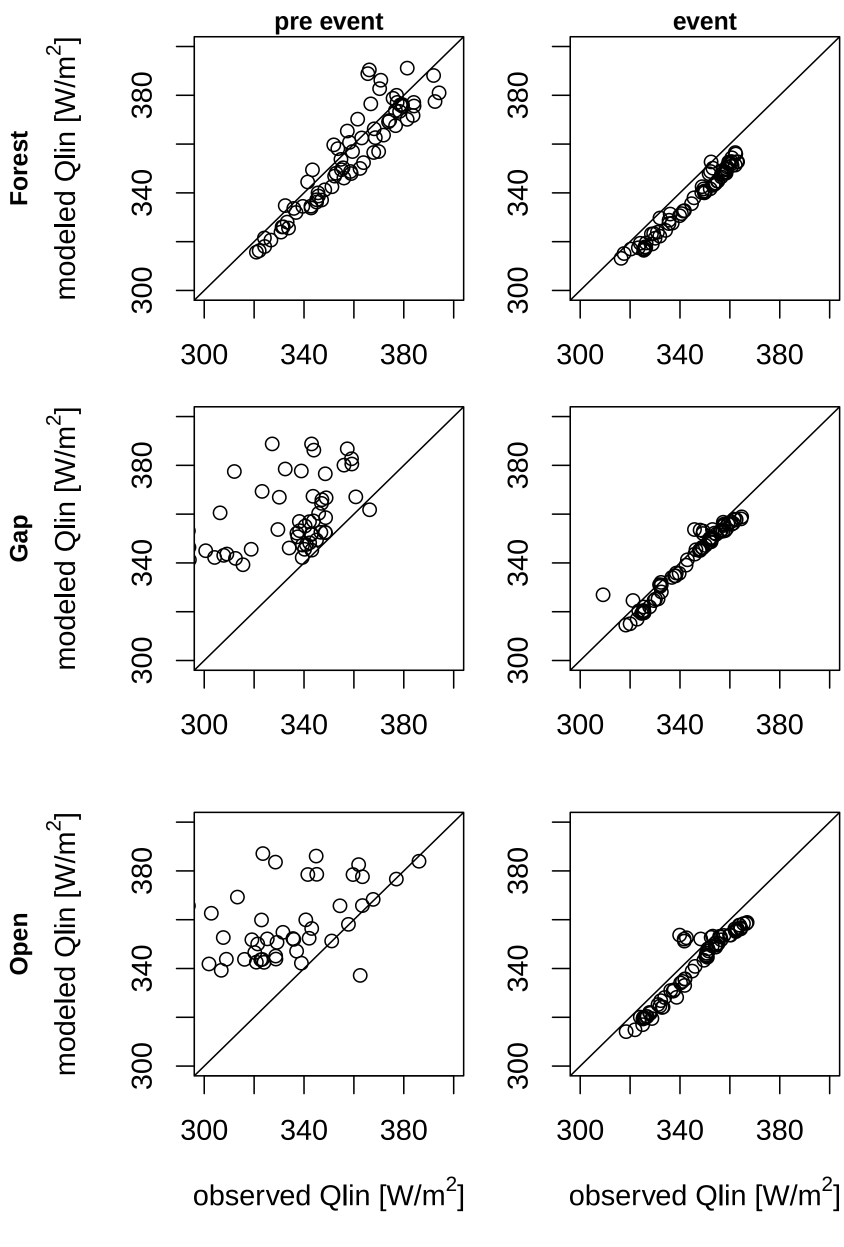

Figure 38: Performance of incoming longwave radiation computation at UF UC and UTow site for the June 2013 event. Assuming atmospheric emissivity of 0.98.

Wind speed evaluation

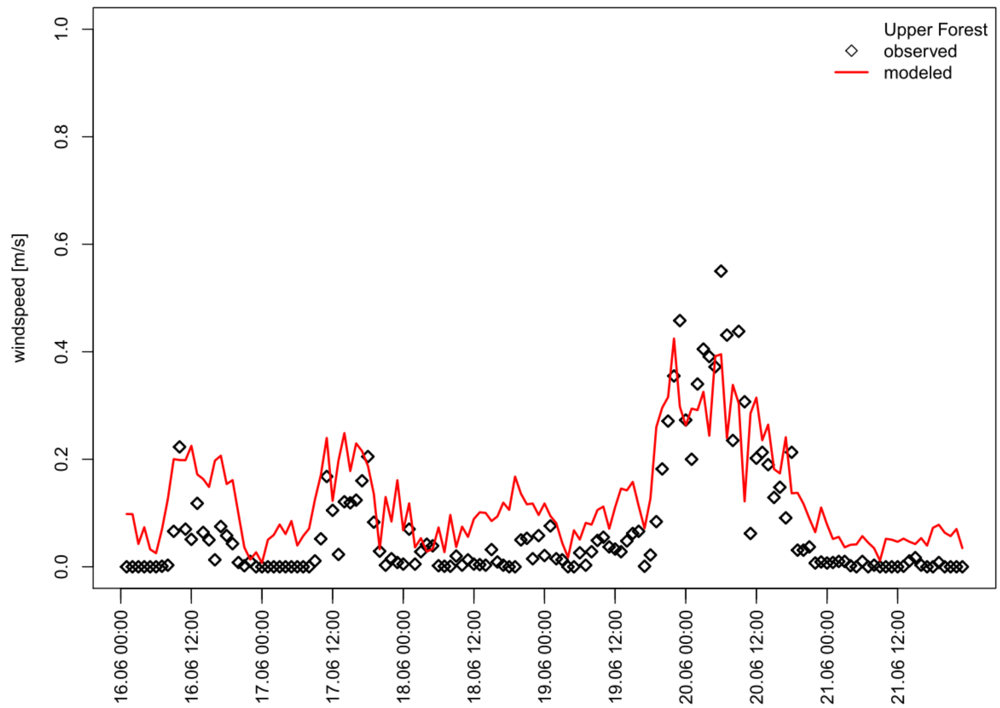

Figure 39: Timeseries of observed and modeled wind speed at UF site for the June 2013 event (attenuation coefficiant = 2.74)

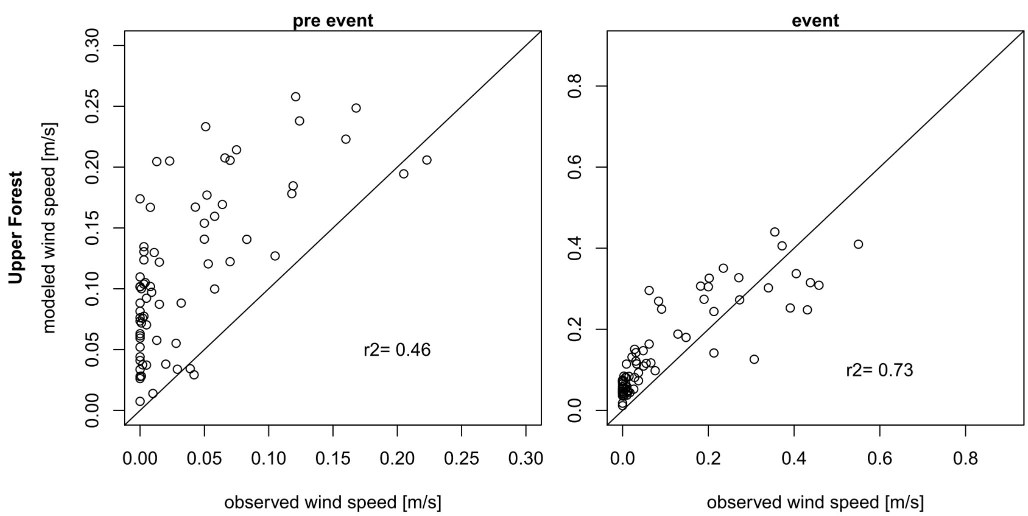

Figure 40: Observed and modeled wind speed at UF and UC site for the June 2013 event (attenuation coefficiant = 2.74)

Appendix B

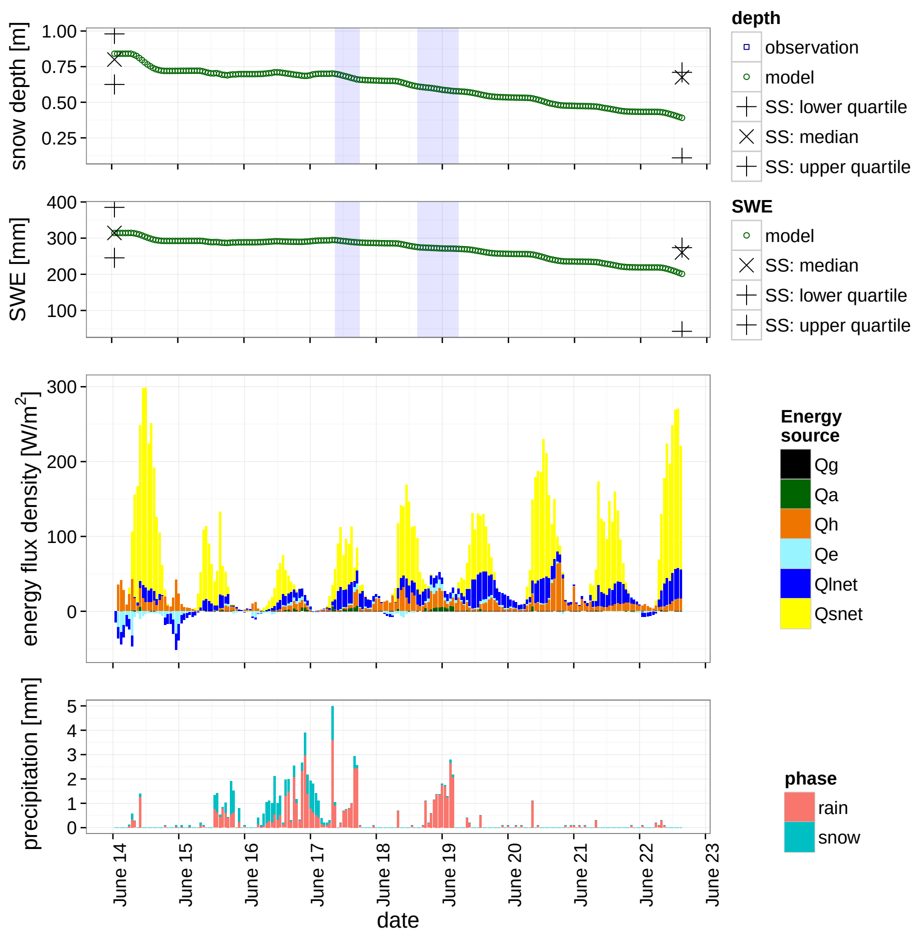

Figure 41: Fisera Ridge South Forest: Modeled and observed (SR50 and snow survey SS) snow depth, SWE and precipitation, as well as the time series of the modeled energy fluxes.

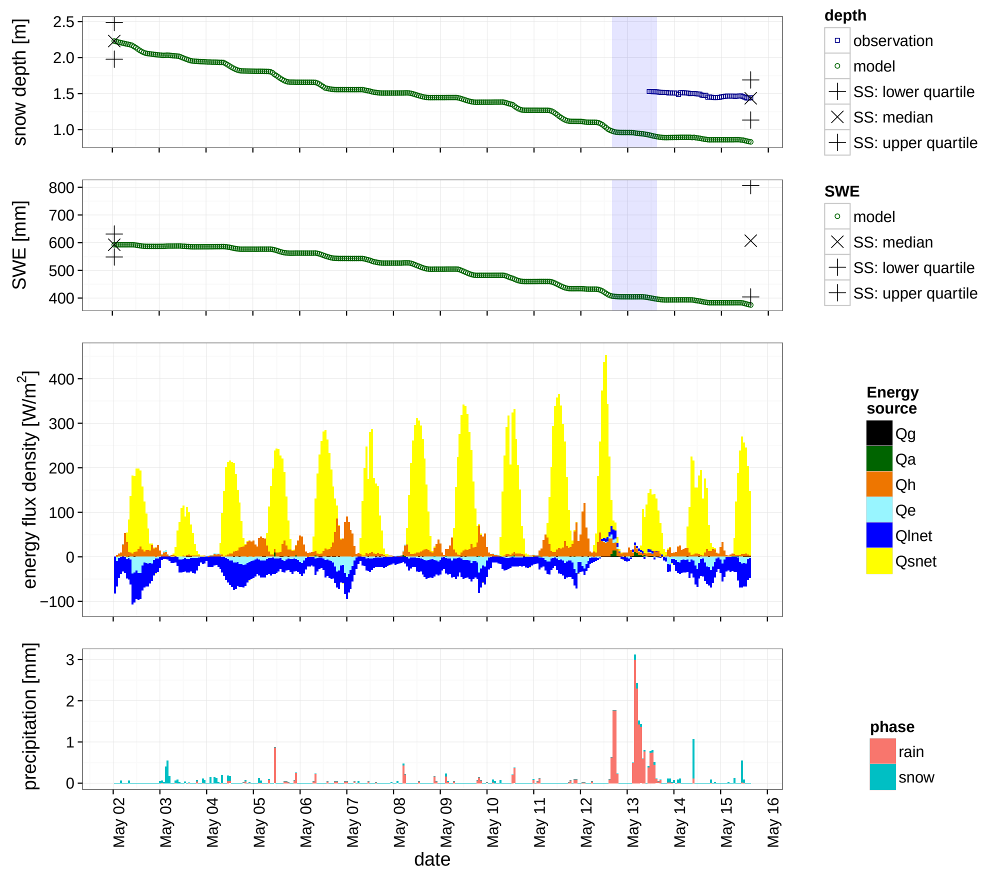

Figure 42: Fisera Ridge South: ROS-event in May 2013. Modeled and observed (SR50 and snow survey SS) snow depth, SWE and precipitation, as well as the time series of the modeled energy fluxes.

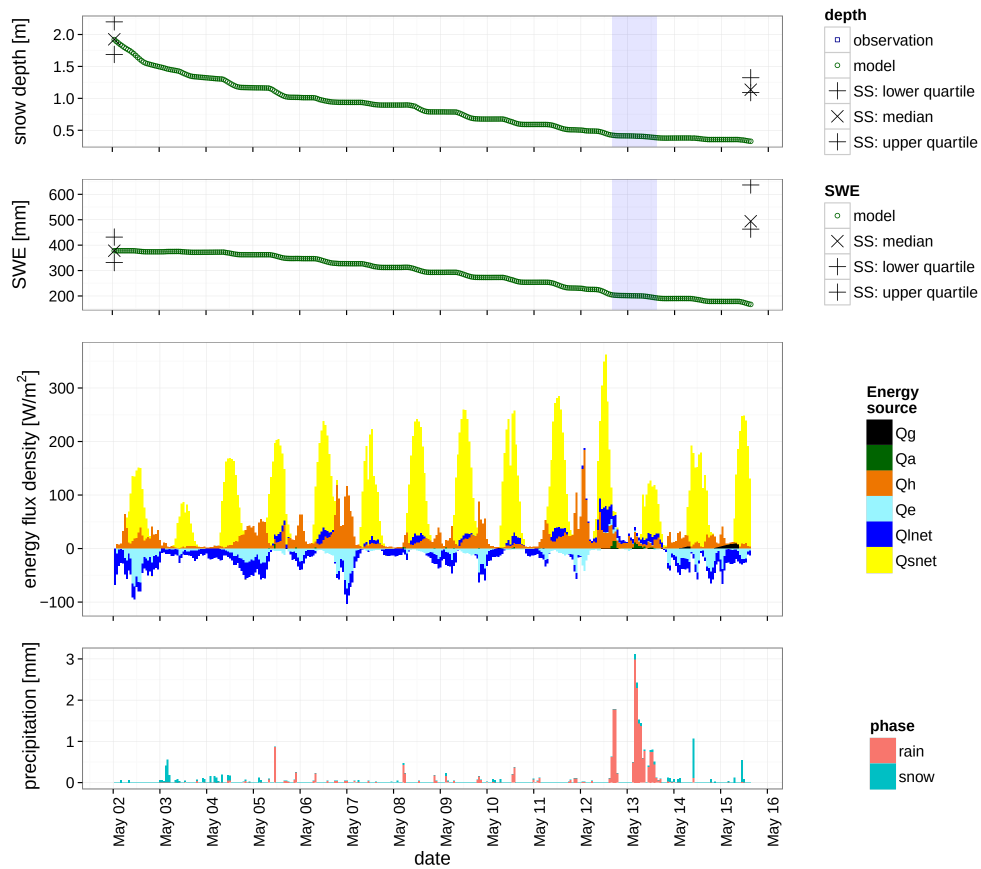

Figure 43: Fisera Ridge South Forest: ROS-event in May 2013. Modeled and observed (SR50 and snow survey SS) snow depth, SWE and precipitation, as well as the time series of the modeled energy fluxes.

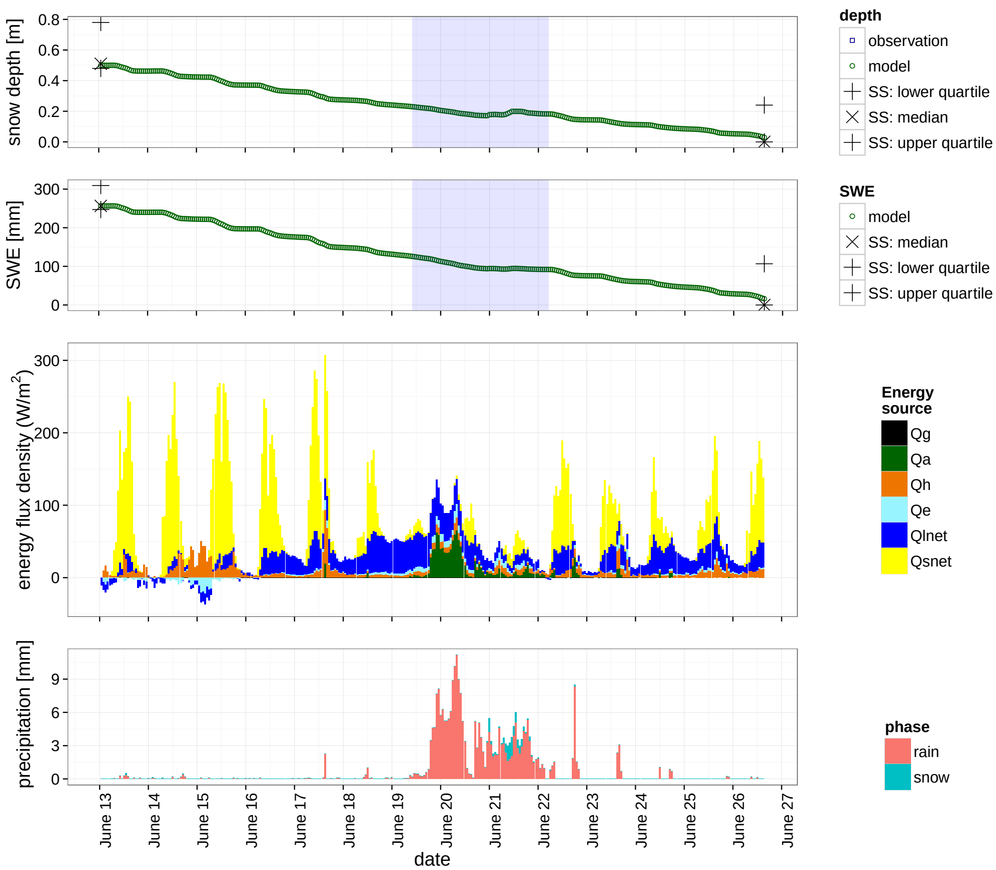

Figure 44: Fisera Ridge South Forest: ROS-event in June 2013. Modeled and observed (snow survey SS) snow depth, SWE and precipitation, as well as the time series of the modeled energy fluxes.

Appendix C

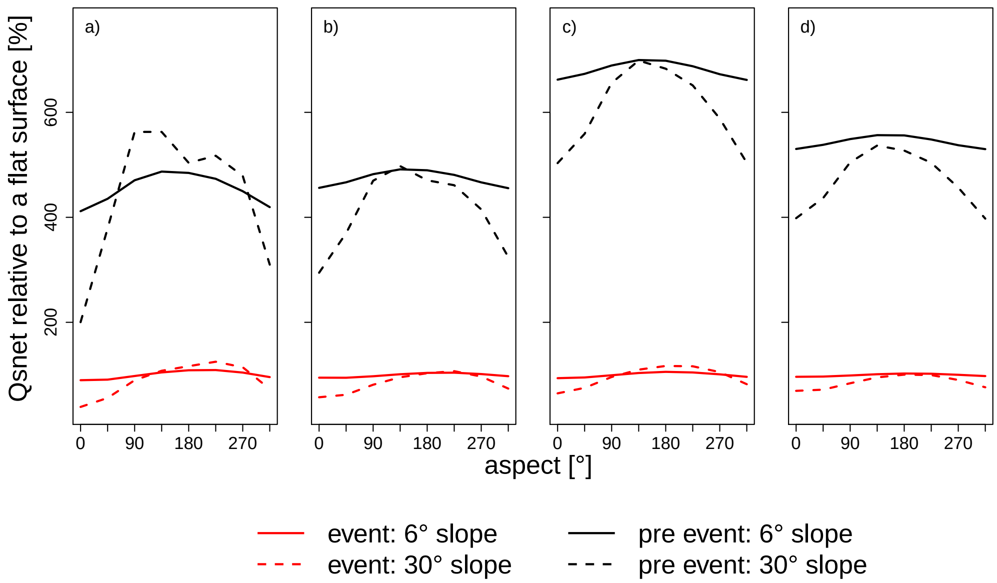

Figure 45: Response of net shortwave radiation to a change in aspect at two different slopes for a pre-event and event period for four land use classes (a) dense forest, b) sparse forest, c) forest gap and d) open).

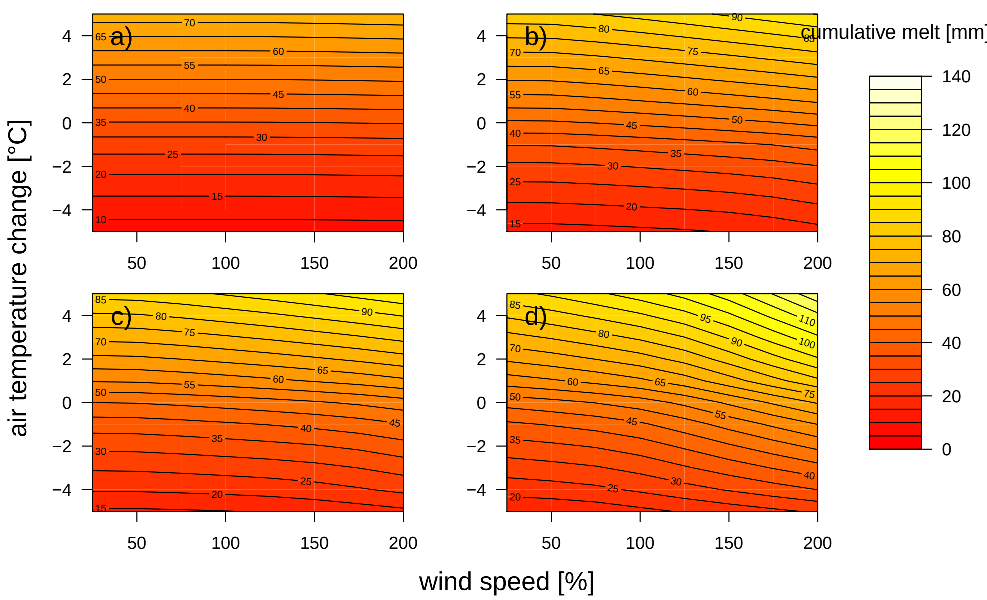

Figure 46: Response surface of cumulative snowmelt to air temperature and wind speed for a three day ROS-period for four land use classes (a) dense forest, b) sparse forest, c) forest gap and d) open).

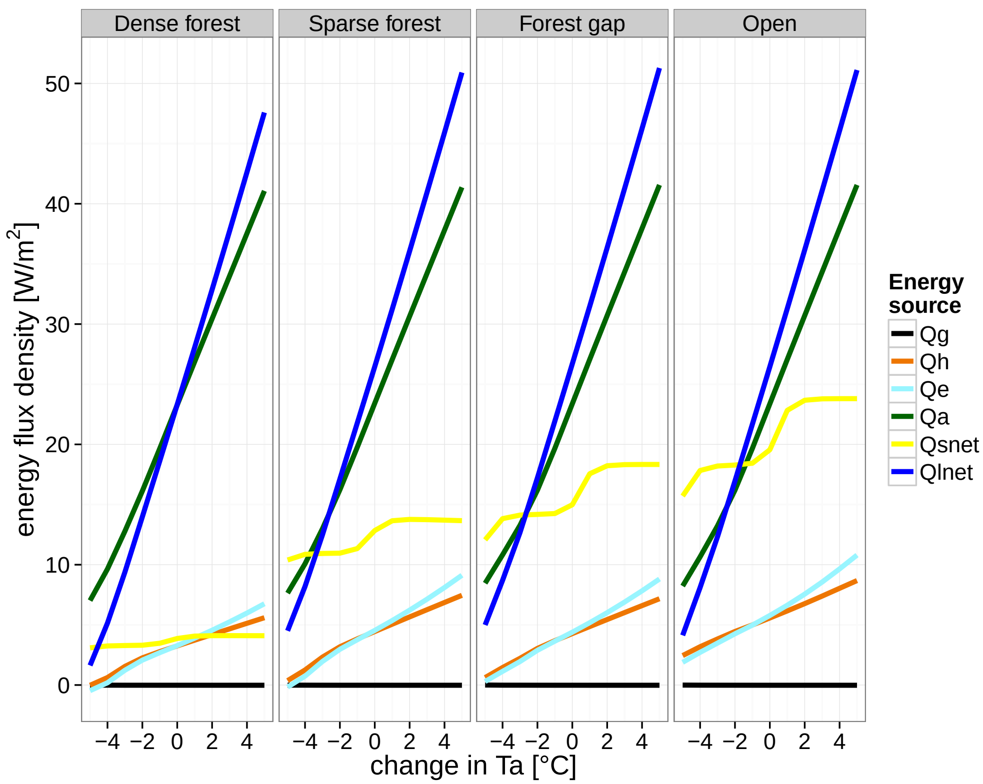

Figure 47: Response of the energy fluxes to a change in air temperature for four land use classes.

Table 8: 1^{st} order sensitivity of energy fluxes.

flux	parameter	unit	D.forest	S. forest	Gap	Open
	T_a	$W/(m^2 {}^\circ C)$	0.548	0.690	0.643	0.610
	u	$W/(m^2\%)$	0.002	0.026	0.028	0.085
Q_h	P	$W/(m^2 mm)$	0.000	0.000	0.000	-0.001
	northing	$W/((m^2 {}^\circ)$	0.000	0.000	0.000	0.000
	easting	$W/(m^2 {}^\circ)$	0.000	0.000	0.000	0.000
	T_a	$W/(m^2 {}^\circ C)$	0.705	0.905	0.836	0.871
	u	$W/(m^2\%)$	0.002	0.027	0.029	0.088
Q_e	P	$W/(m^2 mm)$	0.000	0.000	0.000	-0.001
	northing	$W/(m^2 {}^\circ)$	0.000	0.000	0.000	0.000
	easting	$W/(m^2 {}^\circ)$	0.000	0.000	0.000	0.000
	T_a	$W/(m^2 {}^\circ C)$	3.466	3.449	3.396	3.414
	u	$W/(m^2\%)$	0.000	0.000	0.000	0.000
Q_a	P	$W/(m^2 mm)$	0.236	0.236	0.234	0.234
	northing	$W/(m^2 {}^\circ)$	0.000	0.000	0.000	0.000
	easting	$W/(m^2 {}^\circ)$	0.000	0.000	0.000	0.000
	T_a	$W/(m^2 {}^\circ C)$	0.119	0.401	0.667	0.875
	u	$W/(m^2\%)$	0.000	0.000	0.000	0.000
Q_{snet}	P	$W/(m^2 mm)$	-0.002	-0.010	-0.018	-0.023
	northing	$W/(m^2 {}^\circ)$	-0.008	-0.017	-0.021	-0.017
	easting	$W/(m^2 {}^\circ)$	-0.003	-0.006	-0.004	-0.003
	T_a	$W/(m^2 {}^\circ C)$	4.653	4.688	4.684	4.738
	u	$W/(m^2\%)$	0.000	0.000	0.000	0.000
Q_{lnet}	P	$W/(m^2 mm)$	0.000	0.000	0.000	0.000
	northing	$W/(m^2 {}^\circ)$	-0.001	-0.001	-0.001	0.000
	easting	$W/(m^2 {}^\circ)$	-0.001	-0.001	0.000	0.000

Appendix D

CRHM Report

```
CURRENT TIME: 25.05.2015 13:14
CRHM Version: CRHM 03/26/15
PROJECT FILE NAME:

DIMENSIONS:
   nhru 8
   nlay 1
   nobs 5
OBSERVATIONS:
   D:\Dokumente\Uni\MThesis\CRHM\test\Projects\BATCH\obs\
      batch_u100.obs ( 02.04.2013 01:00 - 19.09.2013 23:00,
      Interval = 01:00 )
DATES:
   2013 6 13
   2013 6 16
MODULES:
   basin CRHM02/24/12
   global CRHM04/19/13
   obs CRHM11/12/14
   Slope_Qsi#1 CRHM07/14/11
   calcsun CRHM10/01/13
   albedo_Richard CRHM03/19/15
   walmsley_wind CRHM07/30/08
   longVt CRHM05/29/14
   netall CRHM04/25/12
   evap CRHM09/26/13
   CanopyClearingGap#3 CRHM11/16/14
   pbsmSnobal CRHM02/04/15
   SnobalCRHM#1 CRHM03/26/15
PARAMETERS:
Shared - basin_area <1E-6 to 1E9>
   8E-6
Shared - hru_area <1E-6 to 1E9>
   1E-6 1E-6 1E-6 1E-6 1E-6 1E-6 1E-6 1E-6
```

```
Shared - hru_ASL <0 to 360>
   0 0 0 0 0 0 0 0
Shared - hru_elev <0 to 1E5>
   1800 1800 1800 1800 1800 1800 1800 1800
Shared - hru_GSL <0 to 90>
   0 0 0 0 0 0 0 0
Shared - hru_lat <-90 to 90>
   51.32 51.32 51.32 51.32 51.32 51.32 51.32 51.32
Shared - Ht <0.001 to 100>
   20 3 0.1 0.1 20 3 0.1 0.1
Shared - inhibit_evap <0 to 1>
   0 0 0 0 0 0 0 0
Shared - Zwind <0.01 to 100>
   2.3 2.3 2 20 2.3 2.3 2 20
albedo_Richard - a1 <0 to 1E8>
   1.08E7 1.08E7 1.08E7 1.08E7 1.08E7 1.08E7 1.08E7 1.08E7
albedo_Richard - a2 <0 to 1E8>
   7.2E5 7.2E5 7.2E5 7.2E5 7.2E5 7.2E5 7.2E5 7.2E5
albedo_Richard - Albedo_Bare <0 to 1>
   0.17 0.17 0.17 0.17 0.17 0.17 0.17 0.17

albedo_Richard - Albedo_Snow <0 to 1>
   0.8 0.8 0.85 0.85 0.8 0.8 0.85 0.85
albedo_Richard - amax <0 to 1>
   0.84 0.84 0.84 0.84 0.84 0.84 0.84 0.84
albedo_Richard - amin <0 to 1>
   0.5 0.5 0.5 0.5 0.5 0.5 0.5 0.5
albedo_Richard - smin <0 to 20>
   4 4 2 2 4 4 2 2
basin - basin_name
   'Marmot'
basin - hru_names
   'DenseForestN' 'ShrubN' 'GapN' 'OpenN' 'DenseForestS' '
      ShrubS' 'GapS' 'OpenS'
 basin - INIT_STATE
   ''
 basin - Loop_to
   '' ''
```

```
 basin - RapidAdvance_to
   ,,
 basin - RUN_END <0 to 1E5>
   0
 basin - RUN_ID <-1E8 to 1E8>
   1
 basin - RUN_START <0 to 1E5>
   0
 basin - StateVars_to_Update
   , , , , , , , , , , , , , , , , , , , ,
basin - TraceVars
   , , , , , , , , , , , , , , , , , , , ,
 CanopyClearingGap - Alpha_c <0.05 to 0.2>
   0.17 0.17 0.17 0.17 0.17 0.17 0.17 0.17
 CanopyClearingGap - B_canopy <0 to 0.2>
   0.038 0.038 0.038 0.038 0.038 0.038 0.038 0.038
 CanopyClearingGap - CanopyClearing <0 to 2>
   0 0 2 1 0 0 2 1
CanopyClearingGap - Gap_diameter <10 to 1000>
   10 20 50 100 10 20 50 100
CanopyClearingGap - LAI <0.1 to 20>
   2.5 1.25 0.1 0.1 2.5 1.25 0.1 0.1
CanopyClearingGap - Sbar <0 to 100>
   6.6 3 1.1 1.1 6.6 3 1.1 1.1
CanopyClearingGap - Surrounding_Ht <0.001 to 100>
   20 3 20 0.1 20 3 20 0.1
CanopyClearingGap - unload_t <-10 to 20>
   -3 -3 -3 -3 -3 -3 -3 -3
CanopyClearingGap - unload_t_water <-10 to 20>
   6 6 6 6 6 6 6 6
CanopyClearingGap - Z0snow <0.0001 to 0.01>
   0.01 0.01 0.01 0.01 0.01 0.01 0.01 0.01
CanopyClearingGap - Zref <0.01 to 100>
   2.3 2.3 2.3 2.3 2.3 2.3 2.3 2.3
CanopyClearingGap - Zvent <0 to 1>
   0.75 0.75 0.75 0.75 0.75 0.75 0.75 0.75
evap - evap_type <0 to 2>
   0 0 0 0 0 0 0 0
```

```
evap - F_Qg <0 to 1>
   0.1 0.1 0.1 0.1 0.1 0.1 0.1 0.1
evap - rs <0 to 0.01>
   0 0 0 0 0 0 0 0
global - Time_Offset <-12 to 12>
   1.67 1.67 1.67 1.67 1.67 1.67 1.67 1.67
longVt - epsilon_s <0 to 1>
   0.98 0.98 0.98 0.98 0.98 0.98 0.98 0.98
longVt - Vt <0 to 1>
   0.25 0.25 0.25 0.25 0.25 0.25 0.25 0.25
obs - catchadjust <0 to 2>
   0 0 0 0 0 0 0 0
obs - ClimChng_flag <0 to 1>
   0 0 0 0 0 0 0 0
obs - ClimChng_precip <0 to 10>
   1 1 1 1 1 1 1 1
obs - ClimChng_t <-50 to 50>
   0 0 0 0 0 0 0 0
obs - ElevChng_flag <0 to 1>
   0 0 0 0 0 0 0 0
obs - HRU_OBS <1 to 100>
   2 2 1 1 2 2 1 1
   1 1 1 1 1 1 1 1
   2 5 1 4 2 5 1 4
   1 1 1 1 1 1 1 1
   3 3 3 3 3 3 3 3
obs - lapse_rate <0 to 2>
   0.75 0.75 0.75 0.75 0.75 0.75 0.75 0.75
obs - obs_elev <0 to 1E5>
   1800 1800 1800 1800 1800 1800 1800 1800
obs - ppt_daily_distrib <0 to 1>
   1 1 1 1 1 1 1 1
obs - precip_elev_adj <-0.1 to 0.1>
   0 0 0 0 0 0 0 0
obs - snow_rain_determination <0 to 2>
   2 2 2 2 2 2 2 2
obs - tmax_allrain <-10 to 10>
   4 4 4 4 4 4 4 4
```

```
obs - tmax_allsnow <-10 to 10>
   0 0 0 0 0 0 0 0
obs - Use_Observations_As_Supplied <0 to 1>
   0
pbsmSnobal - A_S <0 to 2>
   0.4 0.1 0.001 0.001 0.4 0.1 0.001 0.001
pbsmSnobal - distrib <-10 to 10>
   1 1 1 1 1 1 1 1
pbsmSnobal - fetch <300 to 1E4>
   300 300 300 300 300 300 300 300
pbsmSnobal - inhibit_bs <0 to 1>
   1 1 1 1 1 1 1 1
pbsmSnobal - inhibit_subl <0 to 1>
   0 0 0 0 0 0 0 0
pbsmSnobal - N_S <1 to 500>
   2 1 200 200 2 1 200 200
SnobalCRHM - hru_F_g <-50 to 50>
   0 0 0 0 0 0 0 0
SnobalCRHM - hru_rho_snow <50 to 1000>
   100 100 100 100 100 100 100 100
SnobalCRHM - hru_T_g <-50 to 50>
   0 0 0 0 0 0 0 0
SnobalCRHM - KT_sand <0.01 to 3>
   1.65 1.65 1.65 1.65 1.65 1.65 1.65 1.65
SnobalCRHM - max_h2o_vol <0.0001 to 0.2>
   0.0001 0.0001 0.0001 0.0001 0.0001 0.0001 0.0001 0.0001
SnobalCRHM - max_z_s_0 <0 to 0.35>
   0.1 0.1 0.1 0.1 0.1 0.1 0.1 0.1
SnobalCRHM - rain_soil_snow <0 to 1>
   1 1 1 1 1 1 1 1
SnobalCRHM - relative_hts <0 to 1>
   1 1 1 1 1 1 1 1
SnobalCRHM - T_g_or_G_flux <0 to 1>
   0 0 0 0 0 0 0 0
SnobalCRHM - z_0 <0.0001 to 0.1>
   0.003 0.003 0.002 0.0001 0.003 0.003 0.002 0.0001
SnobalCRHM - z_g <0.1 to 1>
   0.1 0.1 0.1 0.1 0.1 0.1 0.1 0.1
```

```
SnobalCRHM - z_T <0 to 10>
   2.3 2.3 2.3 2.3 2.3 2.3 2.3 2.3
SnobalCRHM - z_u <0 to 10>
   2.6 2.6 2.6 2.6 2.6 2.6 2.6 2.6
walmsley_wind - A <0 to 4.4>
   2.5 2.5 3.5 3 2.5 2.5 2.5 2.5
walmsley_wind - B <0 to 2>
   0.8 0.8 1.55 2 0.8 0.8 0.8 0.8
walmsley_wind - L <40 to 1E6>
   1000 1000 40 40 40 40 40 40
walmsley_wind - Walmsley_Ht <-1000 to 1000>
   100 100 20 5 0 0 0 0
INITIAL STATE:
   D:\Dokumente\Uni\MThesis\CRHM\test\Projects\BATCH\int\
      SWEInitialState_BATCH_13_06_22_06_2013_warm_cold-5.int
FINAL STATE:
```